UNIVERSITÀ DEGLI STUDI DI PADOVA

DIPARTIMENTO DI INGEGNERIA CIVILE, EDILE E AMBIENTALE

Master’s Degree in Water and Geological Risk Engineering

MASTER THESIS

Use of satellite imagery for crop water status monitoring: a case study on soybean with Planet and Sentinel-2 satellites

Supervisor:
Chiar.mo Prof. Maurizio Borin
Co-Supervisor:
Prof. Carlo Bettanini Fecia di Cossato

Student: Alessia Bado
Student ID: 2061984

ACADEMIC YEAR 2023-2024

ABSTRACT

This study evaluates the use of satellite data to monitor soybean water status under different irrigation regimes - Full irrigation (FI) and Regulated Deficit Irrigation (RDI) – across varying climate conditions of 2022 and 2023. Three key objectives guided this research: (1) assessing the potential of vegetation indices (NDVI, GNDVI, ENDVI, NDRE, and LAI) in providing real-time insights into crop health and irrigation needs; (2) comparing high-resolution PlanetScope (3 m, daily revisit time) imagery with Sentinel (10 m, 5 days) data for agricultural monitoring; and (3) examining the trade-offs between water savings and crop performance under FI and RDI strategies. Planet vegetation indices (VIs) respond promptly to changes in water availability, capturing the immediate effects of irrigation and rainfall on plant physiological processes and effectively tracking stress conditions, reflecting the in-situ physiological data (stomatal conductance gsw, transpiration T_a, leaf temperature T_{leaf}) measured with porometer/fluorometer LI-600. Comparative analysis between PlanetScope and Sentinel imagery found PlanetScope's high resolution advantageous, but Sentinel provided highly correlated results although underestimations in most indices, suggesting it can be a cost-effective alternative for large-scale agricultural monitoring, but less trustworthy for precision agriculture purposes. The comparison between FI and RDI revealed that RDI, particularly in soils with higher water-holding capacity, can maintain crop yields with reduced water input, offering a sustainable alternative to FI without significantly compromising crop performance. This research concludes that RDI presents a viable strategy for water-scarce regions, providing significant water savings without drastically affecting crop productivity. Furthermore, remote sensing technologies offer practical, accessible tools for global irrigation management, supporting the sustainable intensification of agriculture in the face of climate change and resource limitations.

TABLE OF CONTENTS

AKNOWLEDGEMENTS

I want to express my deepest gratitude to my supervisor, Professor Maurizio Borin, for his patience and good heart, without whom this journey would have been much less enjoyable.

I am also grateful to the PhD student Francesco Morbidini and to the research fellow Giovanni Trevisanuto, who continually helped me with data processing and provided useful guidance on the topics of my thesis. Special thanks are also due to the other professors, researchers, PhD students, and laboratory technicians of the Department of Agronomy, Food, Natural Resources, Animals and Environment (DAFNAE) and the Centre of Studies and Activities for Space (CISAS) in the Department of Industrial Engineering (DII) for their passionate and invaluable work put on this study.

LIST OF FIGURES

LIST OF TABLES

LIST OF ABBREVIATIONS

$BBCH$	Biologische Bundesanstalt, Bundessortenamt and CHemical industry (phenological scale)
$ENDVI$	Enhanced Normalized Difference Vegetation Index
ESA	European Space Agency
EVI	Enhanced Vegetation Index
FC	Field Capacity
FI	Full Irrigation strategy
$GNDVI$	Green Normalized Difference Vegetation Index
IDW	Inverse-Distance Weighting interpolation
LAI	Leaf Area Index
MIS	MultiSpectral Instrument (Sentinel)
$NDVI$	Normalized Difference Vegetation Index
NIR	Near Infrared
$PAWC$	Plant Available Water Capacity
PWP	Permanent Wilting Point
PWS	Plant Water Status
RDI	Regulated Deficit Irrigation strategy
RH	Relative Humidity
SE	Standard Error
VI	Vegetation Indices
VIS	Visible Spectrum

LIST OF SYMBOLS

α	level of significance
ET	evapotranspiration
g_{sw}	stomatal conductance
m	slope of regression line
P	precipitation
q	intercept of regression line
σ	standard deviation
T	temperature
t	t-value of Student’s t test
$t_{\alpha,N-2}$	critical t-value
T_a	apparent transpiration
T_{leaf}	leaf temperature
T_{max}	maximum temperature
T_{min}	minimum temperature
T_r	return period

1. INTRODUCTION

1.1. Overview

The world's sustainable management of water resources has become a critical matter due to recent environmental and agricultural challenges. In particular, the water and agricultural sectors are the most threatened by climate change [1], that modify water fluxes through a continuous rise in global and local temperature and variation in precipitation patterns and intensity [2]. Higher temperatures in turn lead to an increase in evapotranspiration (ET) rates, where ET is a major component of the water cycle, resulting from the combination of two important processes: the loss of water from the soil and water surfaces through evaporation, and transpiration from vegetation stomata [3]. As a consequence of increasing ET and rainfall distribution alterations, river streamflows also vary: this intricate interconnection between the different contributions to the hydrological cycle can compromise water availability due to more frequent drought events [4].

Globally, agricultural irrigation is one of the primary leading actors of water consumption, as it employs about 70% of the global freshwater withdrawal from surface and subsurface systems, reaching an annual water use of about 2500 km^3 globally. This production system provides 40% of the world's food from only 20% of cultivated area and sustains the food supply of both highly populated and arid countries [5, 6]. Nevertheless, recent studies showed that much more water is abstracted for irrigation than crop water requirements, being hence environmentally unsustainable, because it leads to soil salinity, bad management of groundwater, and so on [7, 8, 9]. The ever-increasing demographic growth requires the satisfaction of the need for food security, which strategies will be complex: higher temperatures will imply greater water demand, and in locations where precipitation decreases, irrigation will be severely required but also subjected to unpredictability due to water scarcity [10]. Therefore, intense pressure will be placed on maintaining an optimal crop yield with less water, increasing the overall water use efficiency and avoiding unnecessary losses. An integrated comprehension of the plant water status

(PWS) as a response to decreased irrigation water is then vital to ensure healthy and still productive cultivations, and to ideally schedule the timing and amount of irrigation based primarily on their effective needs. In the agricultural sector, ET is a key parameter for identifying plants' water requirements and potential stress, as its variation is the same as the water absorption rates of vegetation [11]. The traditional irrigation strategy, hereafter referred to as Full Irrigation (FI), is based on distributing enough water to allow crops to transpire to their full potential, satisfying the ET requirements of their growing period, but it obviously implies great water volumes and losses. Alternatively, Regulated Deficit Irrigation (RDI) can be a solution for limiting irrigation water consumption and demand, because it is based on the provision of water below the ET needs for optimal plant growth, thus allowing to virtually achieve 20-50% of water savings [12, 13]. In addition, RDI is proven to increase the level of drought resistance of cultivation [14]; nonetheless, its management is difficult and requires more frequent and precise monitoring than FI, as it is necessary to ensure optimal and not excessive water deficit to avoid a decline in crop yield and quality [15].

Traditionally, decision-making for irrigation refers to ground-based measured information such as historical regimes, monitored environmental parameters and weather data, and visual assessments of soil and crops. These techniques, although dependable, are expensive to acquire a reasonable amount of data. Small leaf samples are then considered representative of whole crops, often leading to over- or under-watering [16]. New approaches have been explored to overcome these limitations: in particular, satellite remote sensing gives the opportunity to capture images and information about PWS over large areas at frequent intervals [17]. The baseline of these methodologies is the exploitation of the electromagnetic wave reflectance from the canopy, which changes according to different biophysical properties, such as plant type and water content within the tissues [18]. Chlorophyll controls much of the spectral response of the plant, absorbing 70 – 90% of blue and red incident light for photosynthesis, while reflecting most of the green radiation. Other structural characteristics of the leaf scatter the infrared light (700–1400 nm) away from its surface, showing the peak of reflectance in this region of the spectrum (Figure 1.1). The behavior of leaf spectral response changes according to the health conditions and the stage of growth: plant stress or senescence can be noticed by the decrease in green and, in particular, near-infrared reflectance, and an increase in the red reflection. As crops attempt maturity, the so-called "red edge shift" occurs, as the point of transition from the red to the infrared reflectance shifts toward longer wavelengths [19, 20]. Therefore, the values of leaf reflectance, particularly in the near-infrared, green, and red portions of the spectrum, as well as the position of the red edge, can be exploited to identify the plant status in terms of health, maturity, and stress conditions.

In this context, several mathematical combinations of leaf reflectance in the different portions of the spectrum result in the calculation of the Vegetation Indices (VI), which can provide information about plant physiological parameters [4]. In particular, the large difference between the infrared (highly reflected) and red (mostly absorbed) reflectance value in an actively growing plant makes the ratio between the two very high; if vegetation is stressed or senescing, the ratio will decrease, being hence correlated to the photosynthetic activity and biomass cover [19]. This ratio is the baseline of the calculation of the most widely used VI in vegetation monitoring, the Normalized Difference Vegetation Index (NDVI): the higher the NDVI, the more active, healthier, and less stressed the vegetation. Nonetheless, red radiations are primarily absorbed by the upper layer of vegetation, hence lower layers do not contribute much to the NDVI measure, compromising its correlation to other important physiological parameters [21].

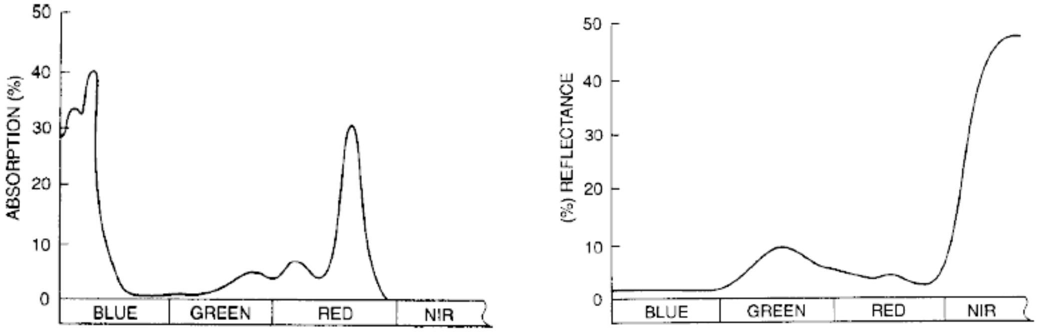

Figure 1.1. [a] Absorption spectrum of leaves, that absorb blue and red light, while reflecting green and near-infrared radiations. [b] Typical spectral reflectance from leaves: green and near-infrared radiations are reflected, with the peak of reflectance in the near-infrared region [19].

Although its capability to qualitatively describe the photosynthetic activity, Gitelson et al. (1996) [20] found that chlorophyll concentration is better described by the green reflectance than the red channel, as its variation depends almost entirely on the amount of chlorophyll itself. For this purpose, they developed the Green NDVI (GNDVI) that uses green in place of the red light, being characterized by a higher sensitivity to chlorophyll concentration and a lower dependence on ground cover variations with respect to NDVI [22]. Another important index, the Enhanced Normalized Difference Vegetation Index (ENDVI), uses the blue portion of the spectrum, together with the infrared and green, to better detect vegetation vigor due to the higher absorptivity of blue compared to the red channel, though it was originally realized for low altitude monitoring systems such as aircraft and drones [23, 24]. Finally, the Normalized Difference RedEdge index (NDRE) is calculated through the same ratio of NDVI but using the red edge wavelength instead of the red, because the former penetrates the leaf deeper than both red and blue wavebands. It works better than NDVI when the crop enters the middle growing stage, when plants start becoming mature to the point where they are chlorophyll-saturated and red light is no longer properly absorbed [25]. Moreover, the RedEdge band is better at measuring the lower layers of the vegetation cover, since it is not absorbed by the top layers as the red radiation [21]. In addition to those listed above, many other VIs have been developed, all of which are useful for interpreting crop vigor and as a potential tool for guiding management decisions [26]. Using these techniques, satellites can be a potential solution for spatial monitoring of agricultural water use, as they can be used by smallholder farmers with insufficient or absent in-situ water use monitoring infrastructure. Nevertheless, significant limitations are carried by these remote sensing techniques due to their spatial and temporal resolution, often ineffective for small-scale detection, in particular those free for the user end [27].

1.2. Satellites for irrigation monitoring

Since the 1970s, scientific researchers have started using remotely sensed images from Landsat-1 to map irrigated areas and estimate water use, even if the majority of the scientific papers about remote sensing monitoring of irrigation have been published from 2015 onward, due to the greater availability of satellite data [27]. Water use monitoring is typically performed following three main methodologies.

The first is based on the use of Thermal Infrared (TIR) imagery (such as the Moderate Resolution Imagining Spectroradiometer MODIS and Landsat) for the estimation of evapotranspiration rates based on the surface energy balance, from which water consumption can be estimated by subtracting the effective rainfall. As reference, [28] inferred surface temperature and different components of the energy balance equation over a semi-arid agricultural area in Eastern Sicily, Italy, through Landsat Thematic Mapper TM5. This information was used to calculate the daily latent heat of vaporization and the net radiation, finally obtaining evapotranspiration fluxes of the area. Typically, the satellite-based energy balance method is complex to apply, due to both the generally coarse spatial resolution of the TIR instruments (1 km for MODIS, 120 m for Landsat TM5), for which specific thermal information for the individual field may be lost [29], and the difficulty in determining precisely the turbulent fluxes components of the energy balance, that impose the assumption of many simplifications.

The second approach employs either passive or active microwave sensors (such as the Advanced Microwave Scanning Radiometer-EOS (AMS-E) on Aqua satellite and Sentinel-1, respectively) to gain soil moisture indirect estimation, which is an important parameter affecting plant growth, due to its influence on PWS, soil temperature, aeration, and so on [30]. These techniques are based on the significant difference between the emissivity of wet (saturated) soils and dry soils, related to the water content of the soil's first layer of water. This is detected effectively by the longer microwave wavelengths due to the low atmospheric noise and greater vegetation penetration [31, 32]. For example, [33] demonstrated the effectiveness of different soil moisture products in detecting irrigation intensity by comparing satellite-based soil moisture and in-situ measurements in China, showing a very high consistency; [34] exploited satellite soil moisture information from coarse resolution satellites to quantify the amount of water applied for irrigation in pilot sites worldwide, through an algorithm that allows deriving the total amount of water entering the soil, given by the sum of precipitation and irrigation. They found a very good agreement with true irrigation levels for both semi-humid and semi-arid climatic conditions, although the issues related to the spatial resolution of the employed satellite products (around 40 km) and the lack of dependable in-situ irrigation observations.

Finally, the last method infers irrigation water use through reflectance-based calculation of VI, from which the crop coefficient can be calculated. This methodology is focused on providing an estimate of crop irrigation requirements, rather than the actual quantification of water use [27]. The present project follows this third approach, for which many researchers have already performed several studies worldwide. For example, Sheffield and Morse-McNabb (2015) [35] utilized satellite information to identify how anthropogenic and environmental factors, such as rainfall and land cover history, affect soil conditions and productivity. Landsat historical acquisitions, with a spatial resolution of 30-60 m, provided the annual cumulated value of NDVI and Spring vegetation cover to show their variability in response to rainfall class and presence or absence of irrigation, as well as to land privatization, to demonstrate that land use history is important in determining soil conditions. The results show that the indices were capable of capturing the strong link between vegetation growth and annual rainfall, having higher annual cumulative values for higher rainfall, and between soil conditions and long-term management of the land, underlying the satellite's capability to identify factors that affect agricultural production and therefore to highlight crop areas where production is not at its full potential. Another satellite constellation, the Pléiades, with a very high optical resolution (0.5 meters), although its limited application in this sector due to its relatively high cost, has been the source of NDVI measurements for monitoring the chlorophyll content in the municipality of Weidenbach, Germany, to estimate local crop yield, proving the valuable contribution of the VI [36]. Earlier studies used another commercial constellation, PlanetScope, that offers daily images at 3 m resolution, for crop water management and monitoring, as well as irrigation requirements [37, 38]. In a paper by Maselli et al. (2020) [39], Sentinel-2 MultiSpectral Instrument (MSI) images, with both high spatial (10 m) and temporal (3-4 days revisiting time) were used to capture irrigation water and NDVI evolutions to discriminate between irrigated and rainfed fields in Central Italy, proving the high quality of this technology in detecting the response of NDVI to water stress conditions in regions with a very accentuate dry season. Sentinel-2 has proven to also be able to capture variability, at the plot scale, in rice cultivation in Portugal by comparing different VIs, observing that NDRE is particularly useful in recognizing non-uniformity in irrigation and crop growth [40].

Satellite remote sensing can also be used to infer some basic biophysical vegetation cover's properties, such as the Leaf Area Index (LAI), representing the ratio between the total area of the upper leaf surface to the ground [41]. In particular, LAI determines the canopy water interception, microclimate, and reflected radiation, thus being related to key plant processes like photosynthesis, evapotranspiration, and carbon flux [42, 43]. Commonly, LAI is estimated through in-situ measurements, but Boegh et al. (2001) [44], in an attempt to derive this parameter from airborne multispectral data, defined a relationship between LAI and a VI called Enhanced Vegetation Index EVI, that is calculated through a mathematical combination of infrared, red, and blue leaf reflectance. The function shows a satisfactory correlation coefficient between the two indices, stipulating a new remote sensing-based method to calculate this key parameter for crop monitoring.

Despite the observed benefits that satellites can provide in monitoring irrigation, several issues are linked to their use at the field scale, mostly related to their spatial and temporal resolutions, meteorological conditions, and accessibility of data. Skakum et al. (2021) [45] compared satellite imagery with different resolutions in the study of within-field corn and soybean yield variability, noting that the coarser the resolution, the lower their ability to accurately infer the variability at the field scale. Specifically, they defined the spatial resolution of 3 m as the threshold for capturing 100% of the yield variability, which reduces to 86%, 72%, and 59% for 10 m, 20 m, and 30 m resolutions, respectively. This matter is linked to the accessibility of data: most of the open access satellite imagery, such as the Copernicus Open Access Hub, which provides free downloads of all Sentinel data, and Landsat archives, are characterized by coarse resolutions, while private companies like Planet offers more precise and frequent on-demand acquisitions, but they are generally expensive [46]. Moreover, commercial satellites have typically a daily temporal resolution (Planet, Pléiades), while the revisit times of Sentinel-2 and Landsat 8 are 5 and 8 days, which is not ideal for farmers who need to make decisions about irrigation management [47]. Finally, another issue is linked to the strong dependence of satellite acquisitions on meteorological conditions, as Visible (VIS) and Near Infrared (NIR) sensors needed to calculate the VIs are not able to penetrate clouds. Consequently, the availability of data can be compromised by bad weather.

1.3. Objectives

In a context where the contention between water scarcity and demographic growth is increasingly challenging, exploring new methodologies and technologies to determine the qualitative response of vegetation and agricultural cultivations to water stress is of paramount importance. These new methods should be feasible and accessible at the global level, as countermeasures to face the issue related to water availability and food production can only be effective if applied worldwide.

The present work aims to investigate the potential use of satellite platforms in monitoring crops and irrigation in particular, seeking information about plants' water status. Specifically, the goal is to understand whether trends of various vegetation indices can provide an indicative picture of the health, growth, and needs of vegetation, and in which measure this information can be of effective help for irrigation management. Moreover, it is interesting to study which of the analyzed indicators respond best and is more sensitive to any kind of change, from variations in water status to senescence.

Although the majority of research on the subject already demonstrates the usefulness of satellites in medium- to large-scale agricultural applications, several problems arise when it comes to precision agriculture, or at any rate the everyday, effective use that an ordinary farmer might make of them. Temporal and spatial resolutions of free access satellites, usually free for the user end, may not be sufficient to promptly take effectual actions in cases of either water stress or surplus, but higher-resolution satellites with a more frequent revisit time are generally expensive, making them unaffordable for smallholders. To address this question, a comparison between spectral information gathered from Sentinel-2 and commercial PlanetScope satellites has been conducted, to investigate to what extent the higher spatial and temporal resolution of PlanetScope is more useful than that of Sentinel, or whether Sentinel can provide the same information with minimal difference in terms of qualitative analysis and thus can be used without compromising crop yield.

The information collected from the two satellites has been exploited to investigate the response to different water inputs of a soybean crop. In fact, in view of a search for an increased irrigation water use efficiency, the performance of Full Irrigation and Regulated Deficit Irrigation strategies has been explored to contribute to the already underway research on the possibility of decreasing water inputs while maintaining or having minimal reduction of crop yield. By looking at the performance of the same cultivation to differentiate irrigation strategies, one can have a perspective on whether the advantages of water savings are not at the expense of crop production or whether RDI poses too many risks to crop performance.

2. DATA AND METHODS

2.1. Study area

2.1.1. Field characteristics

The study area consists of a soybean field located in Castelfranco Veneto, in the Veneto region of northern Italy. Soy was planted in two different portions of the field in 2022 and 2023 (Figure 2.1) to ensure the soil has the same initial conditions: in 2022, it was planted on May 20th and harvested on October 4th; in 2023, instead, it was planted on May 31st and harvested on October 9th. Each field has a dimension of 160x40 meters, further divided into four subplots of 40x40 meters each. Two subplots for each field (subplots 1,2 and 5,6) fall into the Full Irrigation zone (FI), while the remaining two (subplots 3,4 and 7,8) are irrigated through the Regulated Deficit Irrigation (RDI) strategy.

A granulometric analysis was performed on the two fields by georeferencing several points where soil samples were collected. The coarse and fine grain fractions were determined, as these affects soil's water retention capacity, which increases with a finer pore size distribution. Consequently, soils with high percentages of silt, clay, and other fine particles exhibit greater resistance to droughts compared to coarse-grained terrains, consisting of particles with a diameter higher than 2 mm (gravel, sand, etc.) [48]. Thus, soil granulometry provides insight into the soil's ability to endure drought and water scarcity. The Inverse-Distance Weighting (IDW) spatial interpolation technique was applied to these estimates to infer values across the entire plot, with the procedure detailed in Appendix B.

In 2022, 12 sampling points (three per subplot) were used to measure the percentage of coarse-grained soil fraction, from which the fine fraction was derived. The average values for these points are presented in Table 2.1, along with the results of the granulometric analysis, which detailed the specific percentages of clay, silt, and sand. Overall, the coarse fraction is significantly lower than the fine fraction across the entire field, with subplot 1 having the highest sand content (45%).

Figure 2.1. Soybean field in Castelfranco Veneto, Italy. The portions considered in 2022 (green) and 2023 (red) were subdivided into four subplots of 40x40 m each: plots 1,2 and 5, 6 were subjected to Full Irrigation (FI); plots 3,4 and 7, 8 were subjected to Regulated Deficit Irrigation (RDI) in 2022 and 2023, respectively.

Table 2.1. Coarse- and fine-grained fractions (% on the total weight) of the 2022 subplots, with the specific percentages of clay, silt, and sand.

		SUBPLOT	COARSE FRACTION	FINE FRACTION	CLAY	SILT	SAND
IRRIGATION	FI	1	29.45%	70.55%	22%	33%	45%
		2	35.64%	64.36%	23%	33%	44%
	RDI	3	26.39%	73.61%	20%	36%	44%
		4	19.15%	80.85%	27%	35%	38%

Table 2.2. Coarse- and fine-grained fractions (% on the total weight) of the 2023 subplots, with the specific percentages of clay, silt, and sand.

		SUBPLOT	COARSE FRACTION	FINE FRACTION	CLAY	SILT	SAND
IRRIGATION	FI	5	51.82%	48.18%	18%	48%	34%
		6	48.54%	51.46%	19%	51%	31%
	RDI	7	32.66%	67.34%	21%	49%	30%
		8	24.68%	75.32%	24%	47%	29%

In 2023, 64 points were georeferenced, collecting soil samples from 32 points for each subplot of the field. The resulting averages of coarse-grained and fine-grained fractions of the two subplots are listed in Table 2.2, which evidences how the subplot irrigated with RDI has a higher fine-grained fraction compared to the coarse-grained one. Instead, the FI portion of the field shows a higher percentage of coarse soil particles than fine ones.

Two important characteristics of the soil were then derived for each subplot both in 2022 and 2023: the field capacity (FC) and the permanent wilting point (PWP). FC is defined as the amount of soil moisture or water content held in the soil after excess water has been drained out and the downward movement rate has ceased, that typically takes place after 2-3 days after water supply [49]. In the absence of irrigation or precipitation, the water content in the root zone is uptaken by the crop, until the remaining water is held to the soil particles with greater force, making it more difficult for the plant to extract it.

Table 2.3. Field Capacity (FC), Permanent Wilting Point (PWP), and Plant Available Water Capacity (PAWC) values of the 2022 subplots.

		SUBPLOT	**FC (%)**	**PWP (%)**	**PAWC (mm)**
IRRIGATION	FI	1	0.228	0.124	20.76
		2	0.212	0.117	19.06
	RDI	3	0.234	0.122	22.22
		4	0.285	0.161	24.78

Table 2.4. Field Capacity (FC), Permanent Wilting Point (PWP), and Plant Available Water Capacity (PAWC) values of the 2023 subplots.

		SUBPLOT	**FC (%)**	**PWP (%)**	**PAWC (mm)**
IRRIGATION	FI	5	0.163	0.077	34.26
		6	0.177	0.084	37.44
	RDI	7	0.239	0.117	48.56
		8	0.277	0.142	54.03

Eventually, the PWP is reached, where the crop can no longer extract the remaining water [50]. To avoid wasting water and ensuring optimal plant growth, the objective of irrigation is to keep the soil moisture at the FC value, avoiding that plants reach the PWP. These two values allow for the computation of the Plant Available Water Capacity (PAWC), which indicates the maximum amount of water the soil can retain for plant growth [51].

In 2022, FC and PWP values (Table 2.3) reflect the composition of the soil in the different subplots. In fact, RDI subplots have a higher percentage of fine-grained particles, allowing for slightly higher values of FC, PWP, and PAWC, but their values remain comparable. In contrast, in 2023 (Table 2.4), the RDI subplots can hold 43% more water than those under FI owing to the higher percentage of fine-grained soil particles. These findings suggest that the soil in the RDI portion of the field in both years can save more water compared to the subplots subjected to FI, especially in 2023.

2.1.2. BBCH-scale for soybean

The BBCH-scale is a standardized system for coding growth stages that are phenologically similar across various plant species. The complete growth cycle is divided into ten distinct, easily identifiable development phases known as principal growth stages, which are numbered from 0 to 9. Secondary stages are used for more precise identification of specific moments or steps in plant development and are coded using the numbers 0 to 9. By combining the numbers for the principal and secondary stages, a two-digit code is created, ranging from 00 to 99 [52]. In particular, seed planting date is represented as 00, while the harvesting date is coded as 99. These more detailed stages are specific for each crop. The specific BBCH-scale for soybean is represented in Figure 2.2, with the principal growth stages synthetically described in Table 2.5.

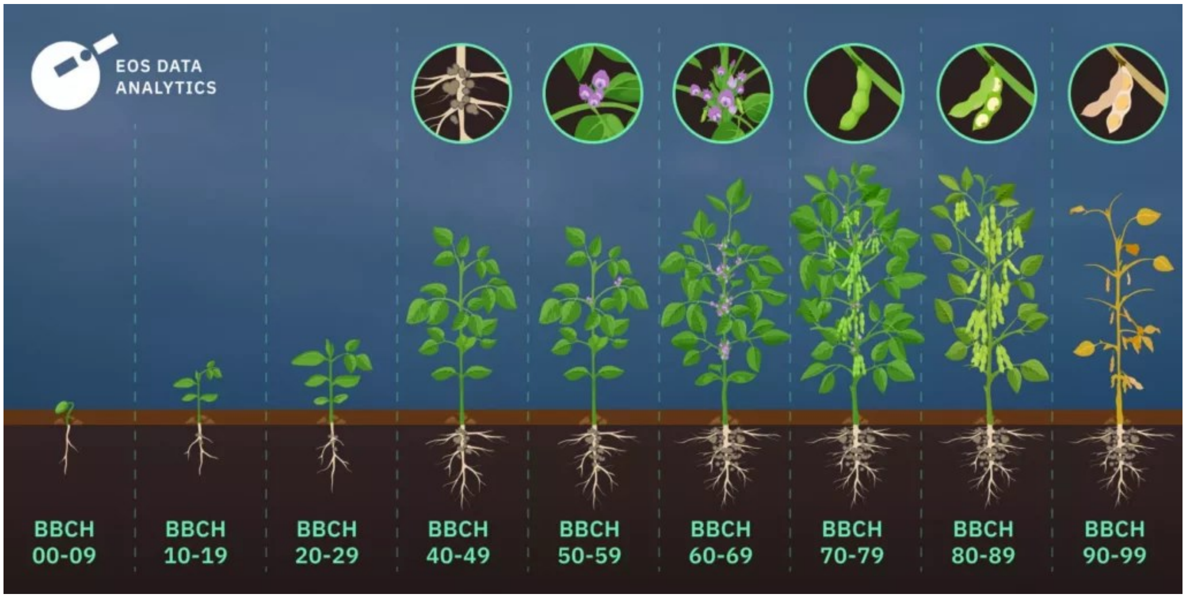

Figure 2.2. Soybean growth stages according to BBCH scale [54].

Table 2.5. Specific BBCH-scale for soybean, with indication of the principal growth stages and a synthetic description [53].

CODE	PRINCIPAL GROWTH STAGE	DESCRIPTION
0	Germination	Development of the plant under the soil surface, from the seed plantation (00) to emergence (09)
1	Leaf Development	Development of young seedling, from the cotyledons unfolding (10) to fully unfolding of the first leaves (19).
2	Formation of Side Shoot	Development of side shoots (20-29).
3	Stem Elongation	Stem elongation proceed parallel to leaf development, therefore a coding in this growth stage is omitted.
4	Development of Harvestable Vegetative Plant Parts	Harvestable vegetative plant parts have reached final size (40-49).
5	Inflorescence Emergence	Inflorescence development, from the visibility of the first flower buds (50) to the visibility of the first petals, but still closed flower (59).
6	Flowering	From the opening of the first flower (60) to the ending of flowering (69), with the first pods visible.
7	Development of Fruits and Seeds	Stage that starts when the first pod reaches its full length (70) and continues until all or most of the pods have reached final size, with seeds filling the cavity of the majority.
8	Ripening of Fruits and Seeds	From the first (80) to the majority (89) of the pods ripe, beans final color, dry and hard.
9	Senescence	Senescence of the plants, from 10% of leaves discolored or fallen (91) to harvested product (seeds) (99).

2.1.3. Irrigation strategies

According to Krote et al. [55], drought stress can exacerbate pod and flower abortion if introduced in early reproductive stages of growth, thus decreasing the number of seed and, therefore, yield. In the literature, significant yield reduction was observed when stress was applied during the initial reproductive stages of soybean, starting from inflorescence emergence (BBCH 50) to the onset of pod formation (BBCH 60) [56]. For this reason, RDI strategy was implemented across all the phenological growth stages except for the principal growth stage 5.

In 2022, the first and last irrigations were applied on June 14th and September 3rd, respectively, counting a total of 15 days of irrigation (Figure 2.3); in 2023, instead, it started on June 6th, and was regularly applied until August 22nd, for a total of applications equal to only 6 days, due to the higher rainfall amounts of the year compared to 2022 (Figure 2.4). The total depths of irrigation water applied throughout the soy growth cycle are listed in Table 2.6: in both years, the total amount of water supplied with the RDI was 23% lower than the water depth applied in the FI part of the field. In Table 2.7, an explicit characterization of the days and amounts of application of the two irrigation strategies are listed. In 2022, the BBCH 50-59 spanned from July 5th to July 20th, while in 2023 it occurred from July 10th to July 25th (see red rectangles in Table 2.7). During this period. 100% of the crop's water requirements were met in both the RDI and FI subplots.

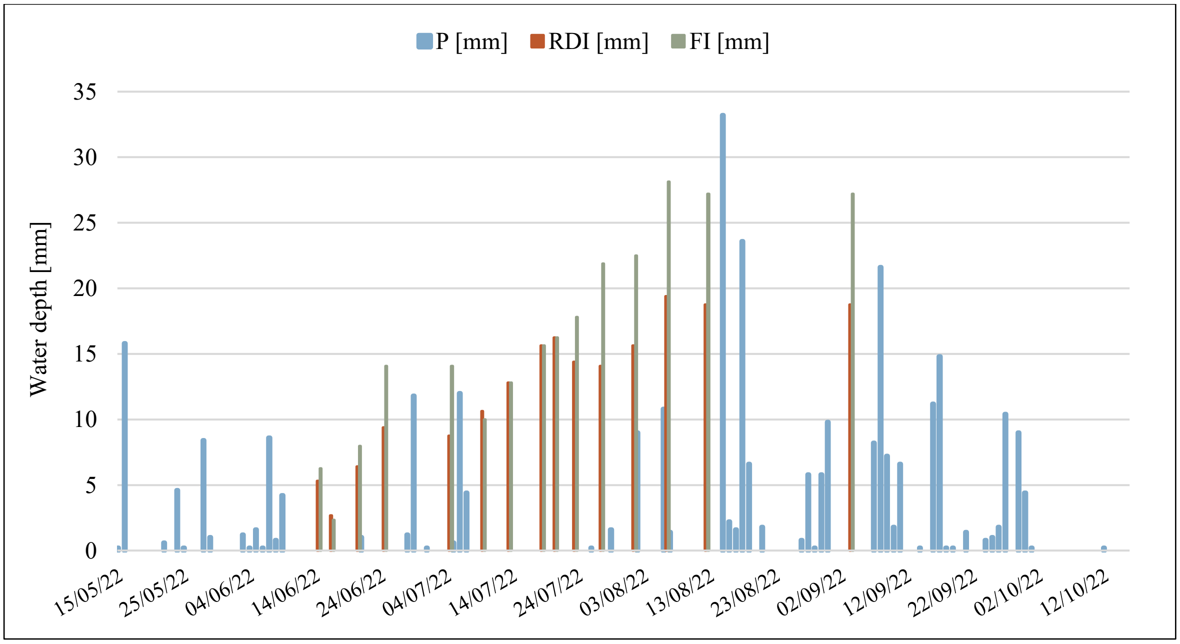

Figure 2.3. Precipitation and irrigation depths [mm] in the period of soybean cultivation in 2022.

Table 2.6. Total irrigation depths applied in 2022 and 2023, according to the corresponding irrigation strategy used. FI refers to Full irrigation, while RDI refers to Regulated Deficit Irrigation.

	IRRIGATION STRATEGY	**IRRIGATION DEPTH [mm]**
2022	FI	244.07
	RDI	188.78
2023	FI	160.90
	RDI	122.90

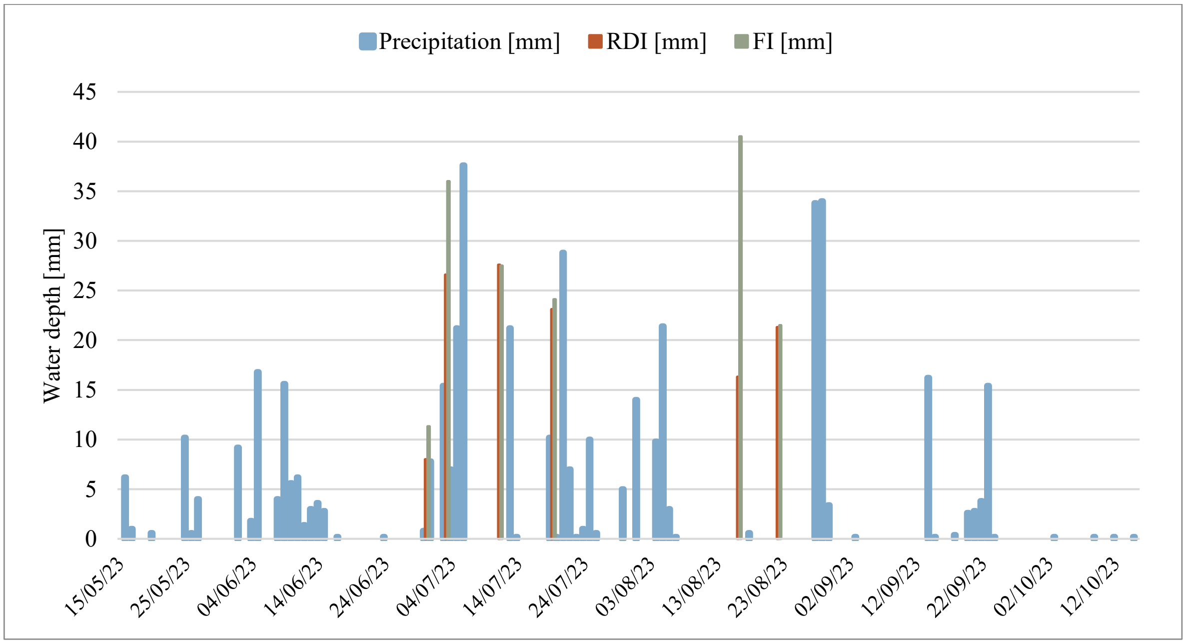

Figure 2.4. Precipitation and irrigation depths [mm] in the period of soybean cultivation cycle in 2023.

Table 2.7. Dates and depths of irrigation water supply [mm] with Full Irrigation (FI) and Regulated Deficit Irrigation (RDI) strategy for 2022 and 2023.The two red rectangles delimitate the periods when RDI was not applied.

Irrigation water supplied [mm]		
Date	**RDI**	**FI**
14/06/2022	5.31	6.25
16/06/2022	2.66	2.34
20/06/2022	6.41	7.97
24/06/2022	9.38	14.06
04/07/2022	8.75	14.06
09/07/2022	10.63	10.00
13/07/2022	12.81	12.81
18/07/2022	15.63	15.63
20/07/2022	16.25	16.25
23/07/2022	14.38	17.81
27/07/2022	14.06	21.88
01/08/2022	15.63	22.50
06/08/2022	19.38	28.13
12/08/2022	18.75	27.19
03/09/2022	18.75	27.19
30/06/2023	8.00	11.30
03/07/2023	26.60	36.00
11/07/2023	27.60	27.50
19/07/2023	23.10	24.10
16/08/2023	16.30	40.50
22/08/2023	21.30	21.50

2.1.4. Historical (1993-2021) climatic series of the site

Castelfranco Veneto is located in the Po Valley of the Veneto region, in Italy, which is characterized by a humid subtropical climate ("Csa" climate) according to the Köppen climate classification [57]. It is typically characterized by high air humidity and hot summers, as well as mild and foggy winters [58]. Monthly and seasonal precipitation is uniformly distributed during the year, reaching total annual rainfall depths of 700 – 1000 mm. Winter is the driest season, while Atlantic and Mediterranean perturbations dominate in spring and autumn, during which occasional occurrences of extreme precipitation events cluster. In summer, instead, rainstorms are quite frequent and irregularly distributed, often associated with hail and, more rarely, whirlwinds. This is due to the high humidity and solar radiation levels, so that lower layers of air masses become unstable, giving rise to storm cells. Regarding temperature, a breakpoint around the late 1980s separates an initial period of roughly stable temperatures and a second period of gradual growth. In particular, the growing trend is estimated to be more than 0.5°C per decade, which is higher than the global +0.33°C trend estimated by the National Oceanic and Atmospheric Administration (NOAA) [59].

The regional agency Agenzia Regionale per la Prevenzione e Protezione Ambientale del Veneto (ARPAV) is constituted of 85 meteorological monitoring stations distributed across the region. Station number 102, whose characteristics are listed in Table 2.8, is located exactly in the city of Castelfranco Veneto, from which a historical meteorological dataset for the study area was downloaded [60]. The period considered ranges from 19th May 1992 to 31st December 2021, counting 30 years of daily information about many important meteorological factors: precipitation, solar radiation, wind, temperature, and relative humidity at 2 meters height. The annual statistical analysis was performed not considering 1992 since data are incomplete; nonetheless, a focus on the important months for soybean growth (May, June, July, August, and September) was investigated examining also that year.

The average annual precipitation [mm] for the considered period resulted in 1117 mm, with the average values for the cited months in Table 2.9. To check the potential occurrences of extreme precipitation events in 2022 and 2023, the annual maxima precipitation depths [mm] (Figure 2.5) were extracted. The Gumbel distribution was hence

Table 2.8. Meteorological station 102 (Castelfranco Veneto) coordinates and altitude in the Gauss-Boaga projection system (a.s.l. refers to the altitude above sea level).

METEOROLOGICAL STATION 102 (CASTELFRANCO VENETO)	
ALTITUDE	50 m a.s.l
LATITUDE	45.694843
LONGITUDE	11.9486259

Table 2.9. Mean precipitation [mm] for May, June, July, August, and September for the considered period (1993-2021 for May, 1992-2021 for the other months).

	MAY	**JUNE**	**JULY**	**AUGUST**	**SEPTEMBER**
Mean P [mm]	120.47	101.93	88.01	94.58	109.77

applied, being a two-parameter model commonly used to simulate a broad variety of extreme data from environmental and engineering sciences [61]. The detailed approach, the relative graphs, and the tables can be viewed in Appendix A. The extreme precipitation depths resulted in 95.31, 113.61, and 170.91 mm for 5-, 10-, and 100-year return periods, respectively. The results for the months interested in soy growth are listed in Table 2.10, from which it can be noticed that precipitation depths are lower for July and August compared to June and September, as precipitation amounts in summer are lower than in mid-season. This is further confirmed by Figure 2.6 and Figure 2.7, in which the average values and a box plot of the total amount of precipitation occurring in the four months are displayed.

The mean temperature for the thirty-year dataset is 13 °C, with extremes of -3 °C and 37 °C on average. In particular, mean temperature has been subjected to an increasing trend, as shown in Figure 2.8, mainly due to a progressive increase of the minima, as the maximum temperatures do not show any trend (Figure 2.9). The same Gumbel distribution procedure was applied to the dataset of the annual maxima of temperatures, to check if any anomaly happened in 2022 and 2023. The results show that a 38.1 °C temperature is associated with a return period of 5 years, with differences across the months considered for soy growth (Table 2.11).

Table 2.10. Precipitation depths [mm] associated with return periods of 5, 10, and 100 years for the months interested in soy cultivation in the considered period (1992-2021).

MONTH	**PRECIPITATION DEPTH [mm]**		
	$T_r = 5\ years$	$T_r = 10\ years$	$T_r = 100\ years$
JUNE	54.57	72.70	129.48
JULY	49.13	63.22	107.34
AUGUST	45.16	55.34	87.19
SEPTEMBER	55.92	71.02	118.30

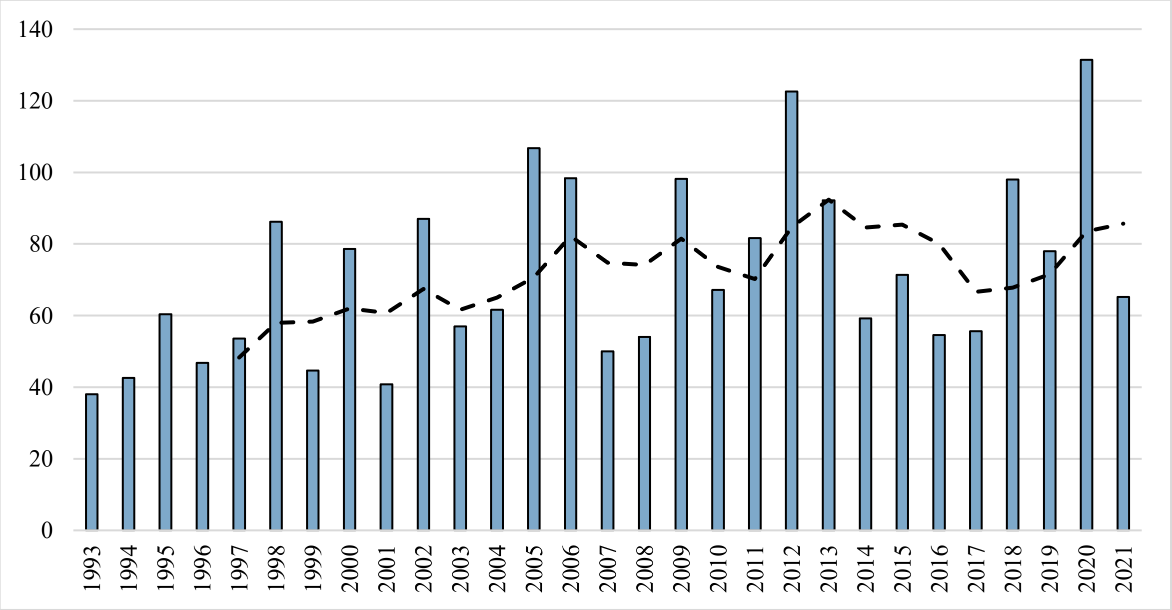

Figure 2.5. Annual maxima precipitation depths [mm] distribution for the 29-year dataset (from 1993 to 2021). The dashed line represents the moving average of five years.

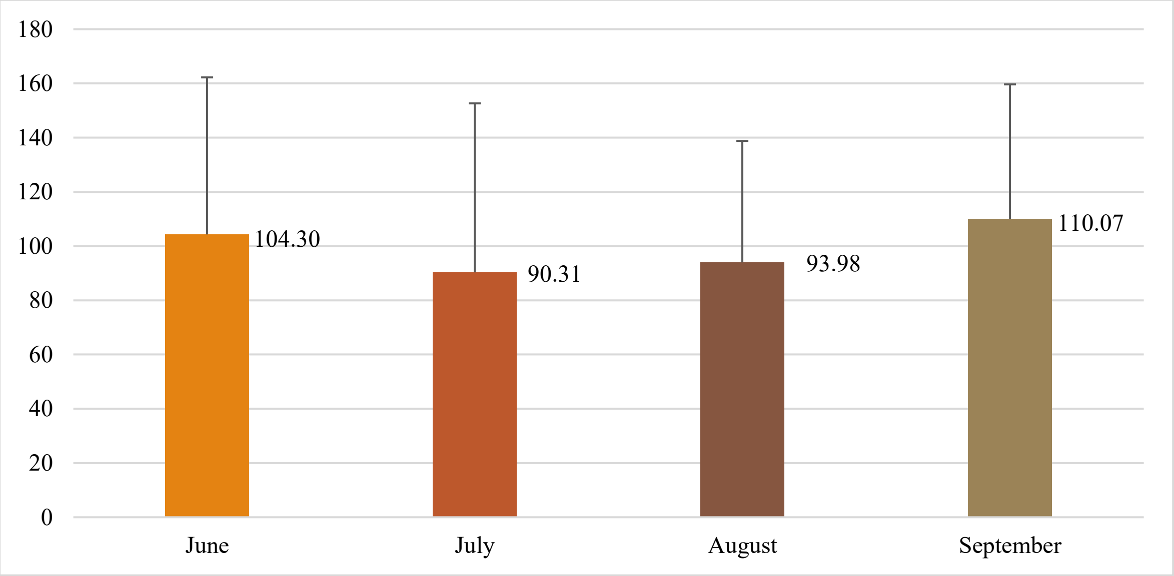

Figure 2.6. Average monthly precipitation depths [mm] for June, July, August, and September over the considered period (1992-2021).

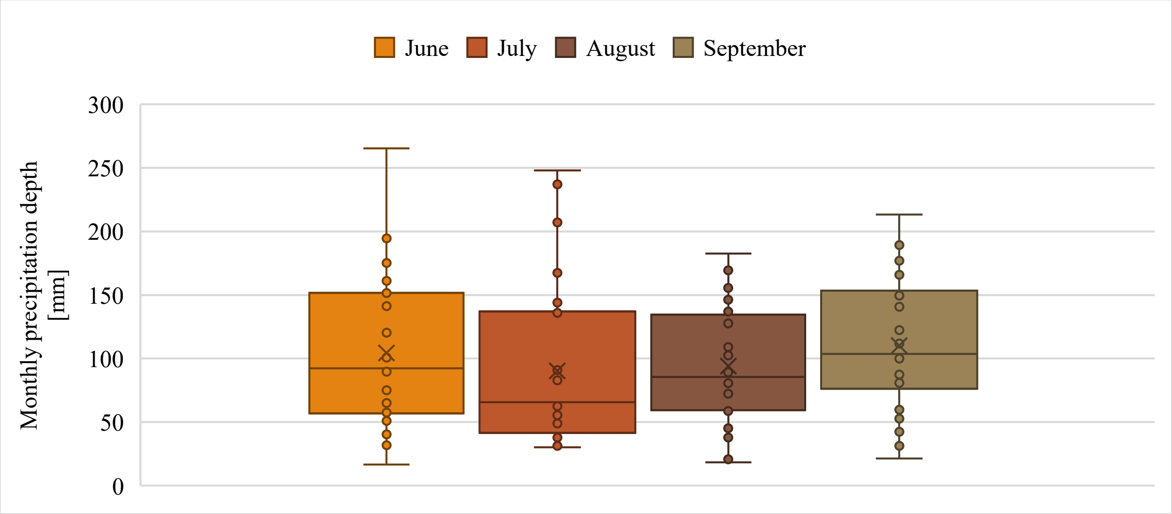

Figure 2.7. Box-plot of the monthly precipitation depths [mm] for June, July, August, and September over the considered period (1992-2021).

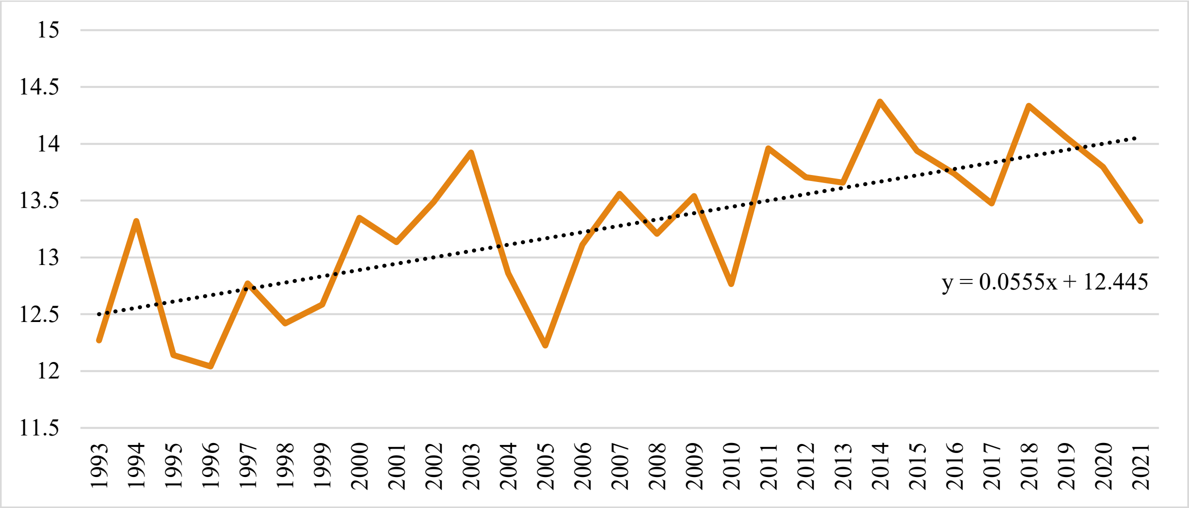

Figure 2.8. Mean temperature [°C] over the period 1993-2021. The dashed line represents the trendline, the slope of which indicates the trend whereby the average temperature increases by 0.056° C each successive year.

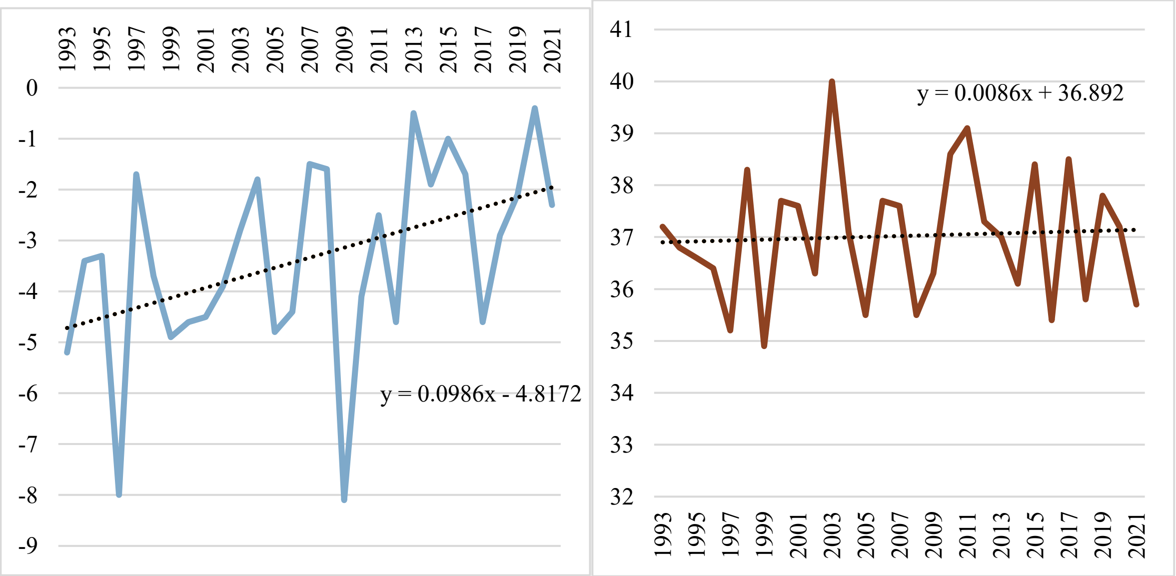

Figure 2.9. Minima (left) and maxima (right) temperatures [°C] over the period 1993-2021. The dashed lines represent the trendlines as simple linear regressions: it can be observed that minimum temperatures are increasing, while the maximum temperatures are not following any trend.

Table 2.11. Temperature [°C] associated with a return period of 5 years for the months interested in soy growth (May considers the years 1993-2021; June, July, August, and September consider the whole period 1992-2021).

MONTH	TEMPERATURE [°C]
MAY	34.7
JUNE	37.2
JULY	38.1
AUGUST	39.0
SEPTEMBER	33.9

Relative humidity (expressed in %) is generally pretty high, reaching values of 85%, 90%, 95%, and 100% for 97%, 93%, 83% and 63% of the days in the total dataset. The minima of the dataset are comprised between 4% and 19%, resulting in a mean within 70% - 78% for each year (Figure 2.10). In particular, the trend of relative humidity in June, July, August, and September is practically the same, with a mean maximum humidity of 99% and an average of the minima around 40-45% (Figure 2.11).

Solar radiation for the years 1993-2021 is characterized by average values of 1.1-2.2 kWh/m^2 in winter, 3.5-5.5 kWh/m^2 in spring, 5.5-6.1 kWh/m^2 during summer, and 1.4-4 MJ/m^2 during autumn (Figure 2.12). Considering that values between 3-4 kWh/m^2 represent high amounts of irradiance, and values higher than 4 kWh/m^2 are very high radiation [62], the study site is subjected to very high amounts of irradiance from April to September. In particular, the solar radiation of June, July, August, and September are shown in Figure 2.13.

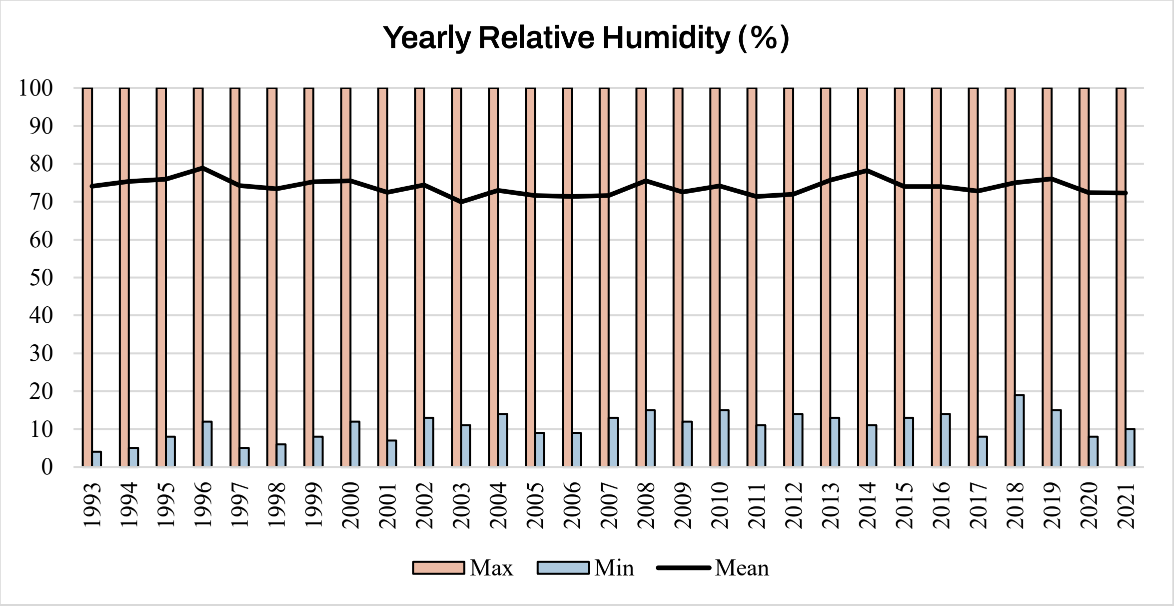

Figure 2.10. Mean, minimum, and maximum values of yearly relative humidity (%) over the period 1993-2021.

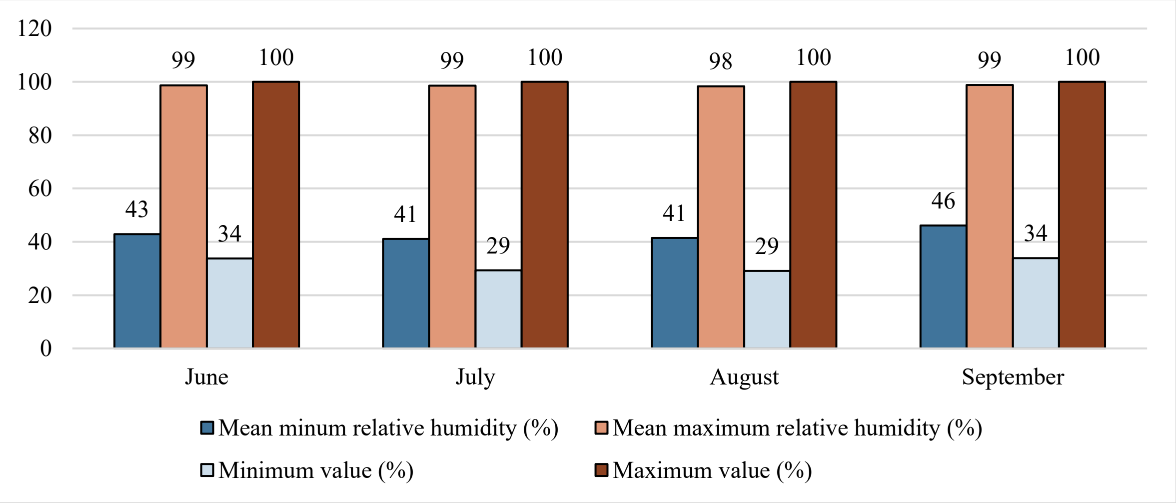

Figure 2.11. Relative humidity (%) in terms of maximum, minimum, mean maximum, and mean minimum values for the months interested in soy growth (June, July, August, September) over the considered period (1992-2021).

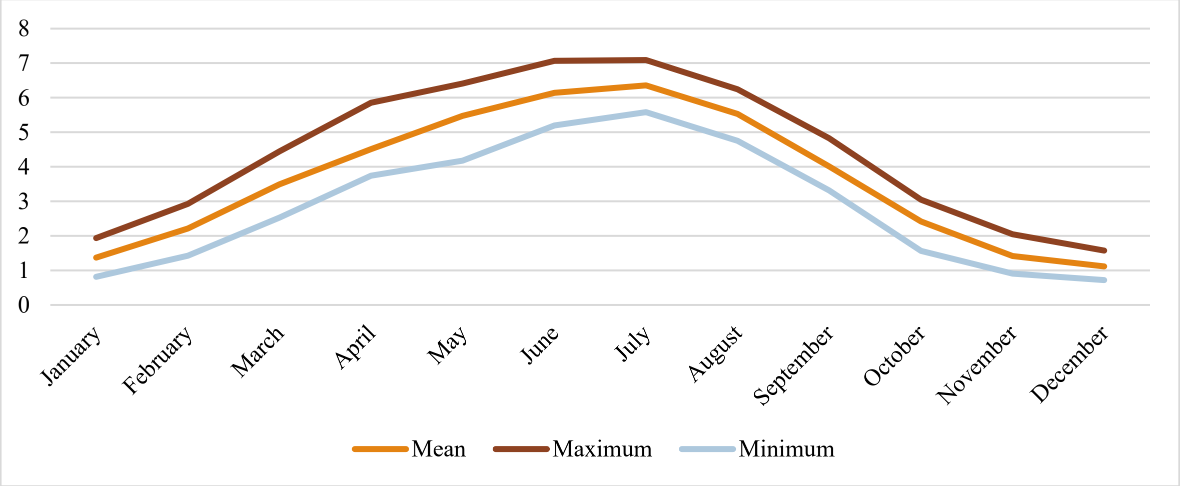

Figure 2.12. Behavior of average, maximum, and minimum solar radiation (kWh/m^{s}) over the considered period (1993-2021).

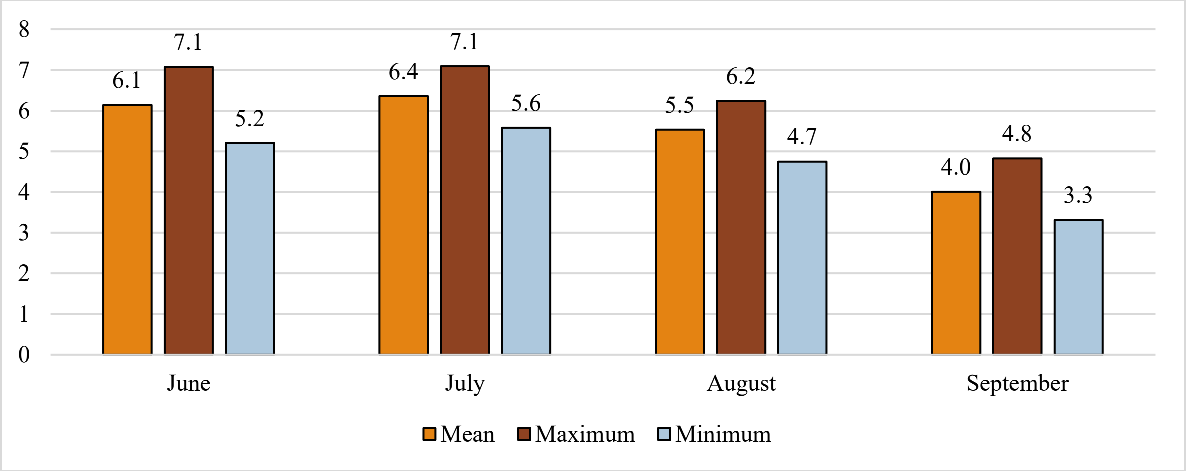

Figure 2.13. Maximum, minimum, and average solar radiation [MJ/m2] for the months interested in soy growth in the considered period (1992-2021).

2.1.5. Regional climatic characterization of 2022 and 2023

According to the national environmental organization Sistema Nazionale per la Protezione dell'Ambiente (SNPA), 2022 was the hottest year in Italy since 1961 [63]. In the Veneto region, in particular, the annual average of daily temperatures was equal to 12.7°C, 1.2°C higher than the reference mean of the period 1993-2021, with values of 18.0°C (+3.2°C) and 7.9°C (+1.2°C) for maximum and minimum daily temperatures, respectively.

Significant anomalies were registered in May (+2°C), June (+2.5°C), July (+2.5°C), and October (+3.2°C). At the same time, rainfall has been incredibly low throughout the territory: the total cumulative precipitation depth of 2022 was the lowest of the past 30 years, registering a regional mean of 771 mm vs. a baseline average of about 1100 mm, resulting in severe drought conditions that lasted almost all months. The highest deficits were registered in March (-81%), May (-43%), June (-44%), July (-40%), and October (-83%) [64].

Following the trend of 2022, 2023 was the second hottest year in Italy since 1961 [65]. In the Veneto region, the annual average, average maxima, and average minima were higher than the reference averages of the period 1993-2021, with anomalies of about +1.1°C, positioning 2023 as the second hottest year of the thirty-year dataset, after 2022. In particular, although the temperatures were generally close to the mean in spring, the hot temperatures of the summer season resulted in 2023 becoming the fifth and seventh hottest year in the ranking of summer maximum and minimum temperatures, respectively. Autumn, particularly September and October, registered the second-highest average maximum temperature of the historical series, during which almost all months were characterized by higher average temperatures compared to the reference mean. Moreover, precipitation were mostly lower than seasonal averages: the wettest months in percentage terms were August (+10%), May (+50%), July (+60%), and October (+65%), while the months that registered the lowest amount of precipitation with respect to the mean were September (-55%) and February (-94%) [66].

2.2. In–situ data

2.2.1. Meteorological station

Meteorological station 102 located in Castelfranco Veneto (Table 2.8) provided data about precipitation, temperature, relative humidity, and solar radiation over the study area for the years 2022 and 2023, during which the study was conducted. The research for extreme events was achieved by applying the results of the Gumbel distribution for the historical dataset to the 2022 and 2023 climatic information, thus being able to define the outliers through the associated return period.

2.2.1.1. 2022

Precipitation in the study area followed the national trend reported in [63], showing in general pretty low cumulative rainfall for the entire year. In particular, the number of rainy days was 10, 6, 14, and 17 in June, July, August, and September, respectively, contributing to a total amount of precipitation of 323.6 mm from May to October. The total amount of precipitation was pretty low in July, with only 19 mm of rain, being the driest month, while August was characterized by the highest value of 112.6 mm, mostly due to the one extreme event of the considered period, which occurred roughly from August 15th to 18th. Except for that episode, which was characterized by a total precipitation depth of 60.6 mm, with a peak of 33.2 mm on August 15th, most of the days were dry, particularly in July (25 days) and June (20 days). The precipitation amounts are plotted in Figure 2.14, where May and October are also included.

Temperatures were significantly high during the whole period of record, with maximum temperatures in the range of 30-39°C from May to September (Figure 2.15); only October registered a maximum temperature lower than this threshold (27°C).

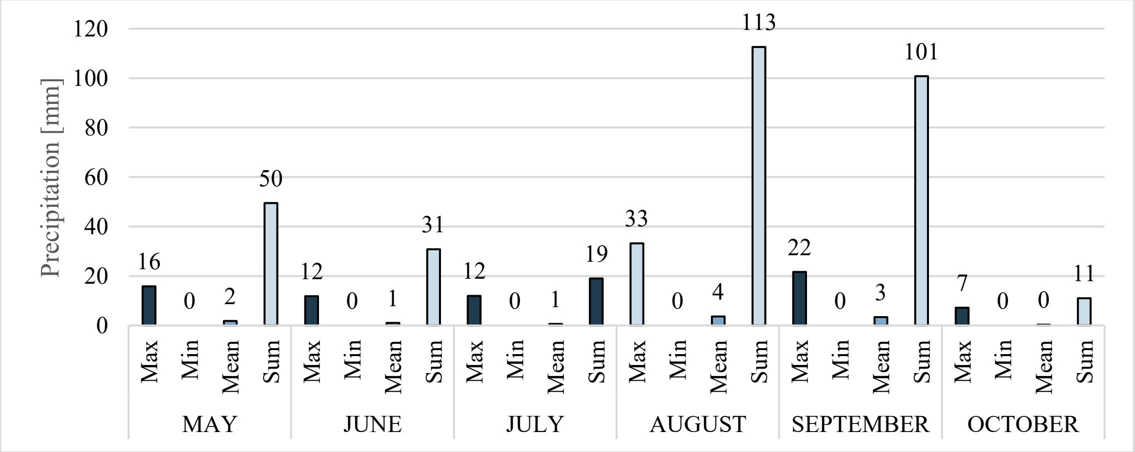

Figure 2.14. Maximum, minimum, mean, and total precipitation depths [mm] for the months interested in soy cultivation in 2022.

Table 2.12. Average solar radiation [kWh/m2] values for the months interested in soy cultivation in 2022.

MONTH	May	June	July	August	September	October
SOLAR RADIATION [kWh/m²]	5.90	6.44	7.09	5.86	4.30	3.03

In particular, maximum temperatures in the range of 27-31 °C started already from May 11th. Then, June and July showed several heat waves: from June 19th to 21st and from June 25th to 27th, with maximum temperatures in the range 34.1-34.9 °C, and from July 19th to 25th, going from 35.9 to 38.5 °C. These values perdured until the beginning of August, in particular from August 1st to August 6th. After this period, temperatures returned to the mean values for the rest of August and almost all of September, until a hail event happened in the area on September 17th. After this episode, temperatures dropped from 30°C on September 15th to 17.8°C on that day, keeping low values in the range 18.3-23.3°C for the rest of the month. Regarding the behavior of relative humidity in the study area, the months from May to October showed mean percentage values in the range of 62-76%, which is slickly lower than the average in the area, contributing to the dry and drought conditions of the year. Concerning solar radiation, each month showed an average value that falls into the very high amounts of irradiance, with the only exception of October, with an anyway high value of 3.03 kWh/m² (Table 2.12).

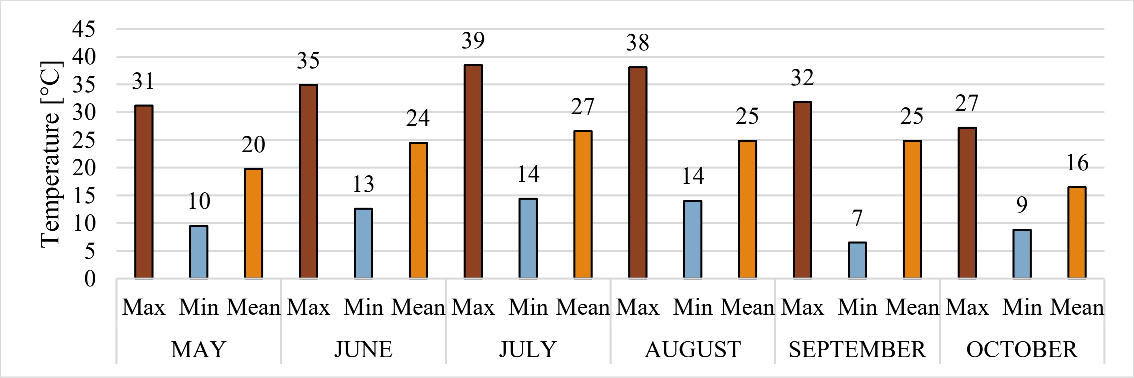

Figure 2.15. Maximum, minimum, and mean temperature [°C] for the months interested in soy cultivation in 2022.

2.2.1.2. 2023

The total precipitation depth in the period from May to October resulted in 430 mm, more than 100 mm more than in 2022, even though the total number of rainy days is lower (14, 16, 9, and 9 days of rain for June, July, August, and September, respectively). The specific amounts of rain depth for each month are illustrated in Figure 2.16. This is because intense precipitation events occurred with higher frequency in 2023 than in 2022. In particular, from July 3rd to July 6th a total of 81.2 mm of rain fell in the area, with a peak of 37.6 mm on July 6th. In the same month, rainfall lasted one week, with a peak of 28.8 mm on July 21st and a cumulated rainfall of 58 mm. August was almost entirely dry, counting 19 consecutive days without rainfall, until another intense event happened on the 28th and the 29th, with precipitation amounts equal to 33.8 and 34 mm, respectively.

Temperatures, on the other hand, were less extreme than in 2022 (Figure 2.17). Temperature values were in the average range for almost all months, with small exceptions in July, but the maximum temperature never went above 35.5°C, compared to the 39°C registered in 2022. Nonetheless, August and September showed in particular two episodes of high temperatures with respect to the average: from August 21st to 26th the maximum temperature stayed constantly in the range of 35.6-37.3°C, and September 8th to 11th registered values from 30.9°C to 31.8°C. Temperatures have maintained high until the second week of October, keeping the range of 25 – 31°C.

Relative humidity showed higher values compared to 2022, with mean values ranging from 70% to 80% in the considered period, resulting in more alignment with the usual mean values for the study area. Finally, average solar radiation resulted lower than the precedent year, although with values falling into the “very high” category as well, with the only exception of October, which showed a moderate amount (Table 2.13)

Table 2.13. Average solar radiation [kWh/m2] values for the months interested in soy cultivation in 2023.

MONTH	May	June	July	August	September	October
SOLAR RADIATION [kWh/m^2]	5.12	6.56	6.42	5.68	4.60	2.68

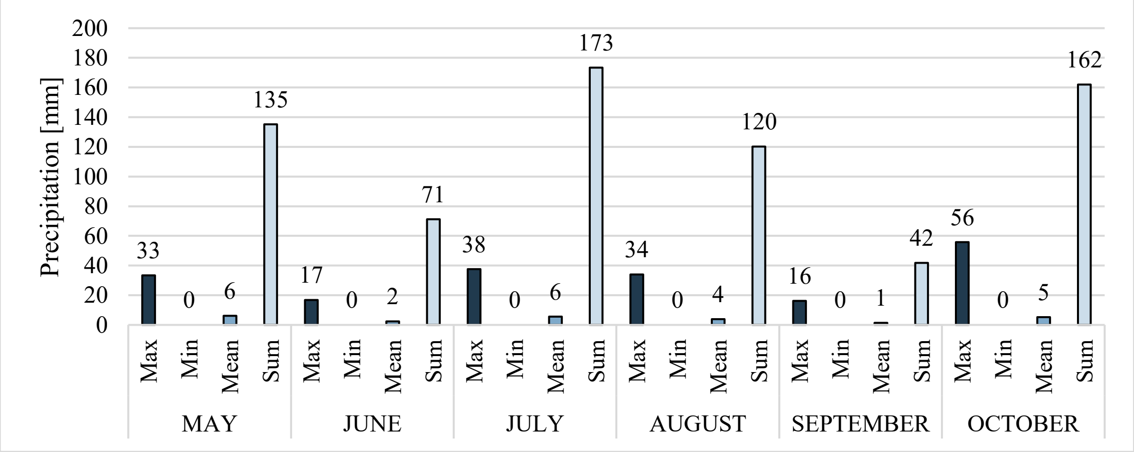

Figure 2.16. Maximum, minimum, mean, and total precipitation depths [mm] for the months interested in soy cultivation in 2023.

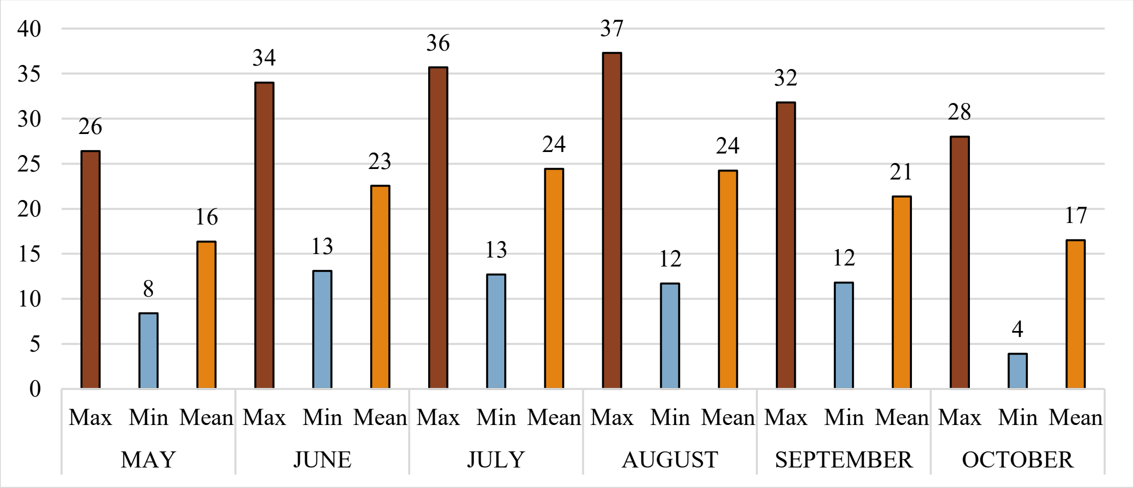

Figure 2.17. Maximum, minimum, and mean temperature [°C] for the months of soy cultivation in 2023.

2.2.1.3. Cumulative frequency of precipitation and temperature of 2022 and 2023

The cumulative frequencies associated with annual maxima precipitation and temperature of 2022 and 2023 compared to the historical series were analyzed.

1. As can be noticed from Figure 2.18, June registered a very low amount of annual maxima precipitation with respect to the historical maximum, both in 2022 and 2023: in particular, 2022 was the second driest year of the series. Maximum temperatures are quite high for 2022 (with a cumulative frequency of 0.61) and on average (0.42) for 2023 (Figure 2.19).
2. Small annual maxima precipitation depths perdured in July (Figure 2.20, Figure 2.21) for 2022 (with a cumulative frequency of 0.15) with, at the same time, the second highest value of cumulative frequency associated with maximum temperature (0.94). In 2023, the monthly maximum rainfall increased up to a cumulative frequency of 0.73, with maximum temperatures that are slightly over the average (0.58).
3. The trend of low annual maxima precipitation for 2022 showed a temporary inversion in August (Figure 2.22, Figure 2.23), returning to values close to the historical average, with a cumulative frequency of 0.52, followed by a similar value for 2023 (0.55). Regarding maximum temperatures, both years showed pretty high cumulative frequencies, with 2022 and 2023 the fourth (0.88) and eighth (0.76) highest values of the series, respectively.
4. Finally, September (Figure 2.24, Figure 2.25) registered low annual maxima precipitation amounts (0.24 for 2022, 0.09 for 2023) and quite high maximum temperatures (0.61 for 2022, 0.64 for 2023).

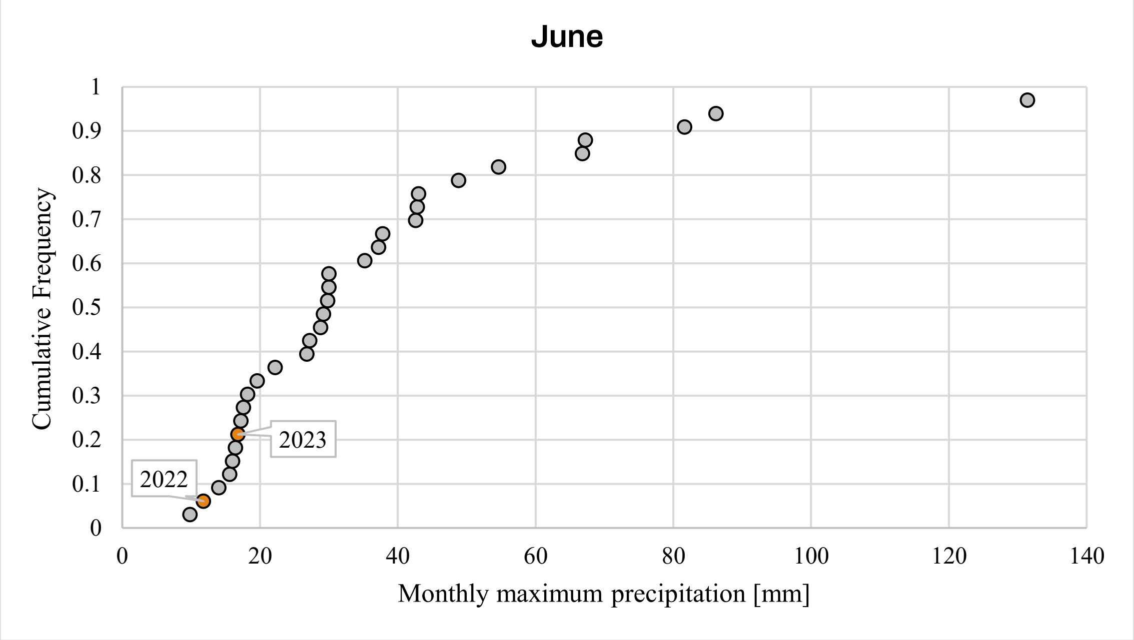

Figure 2.18. Cumulative frequencies of the monthly maximum precipitation depths of June of the historical series (1992-2023). In red, 2022 and 2023 are highlighted.

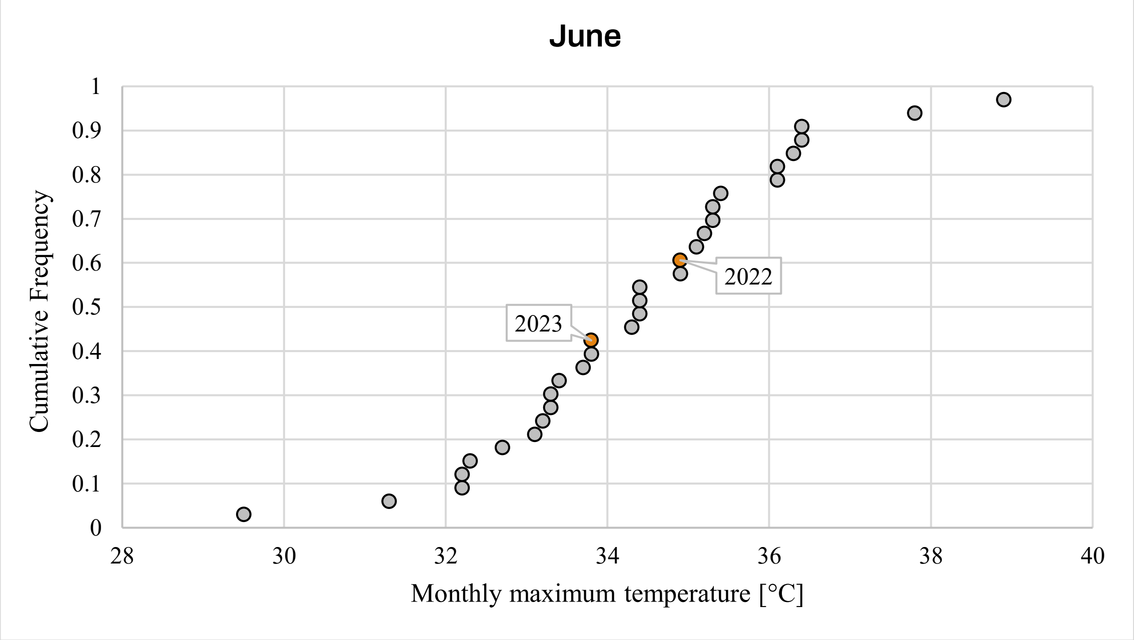

Figure 2.19. Cumulative frequencies of the monthly maximum temperature values of June of the historical series (1992-2023). In red, 2022 and 2023 are highlighted.

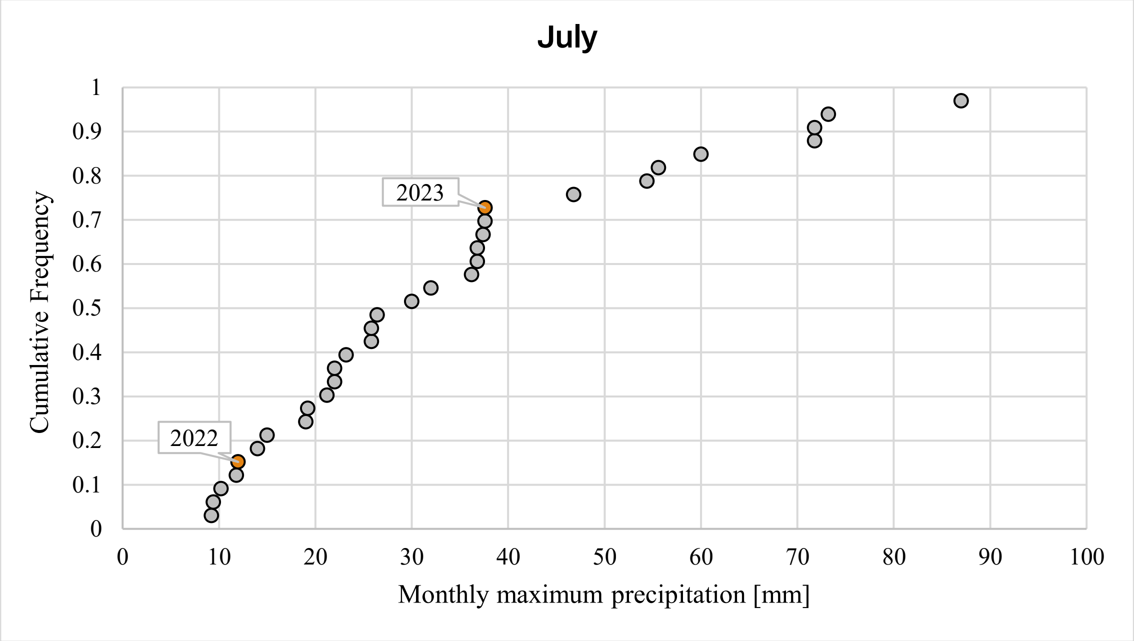

Figure 2.20. Cumulative frequencies of the monthly maximum precipitation depths of July of the historical series (1992-2023). In red, 2022 and 2023 are highlighted.

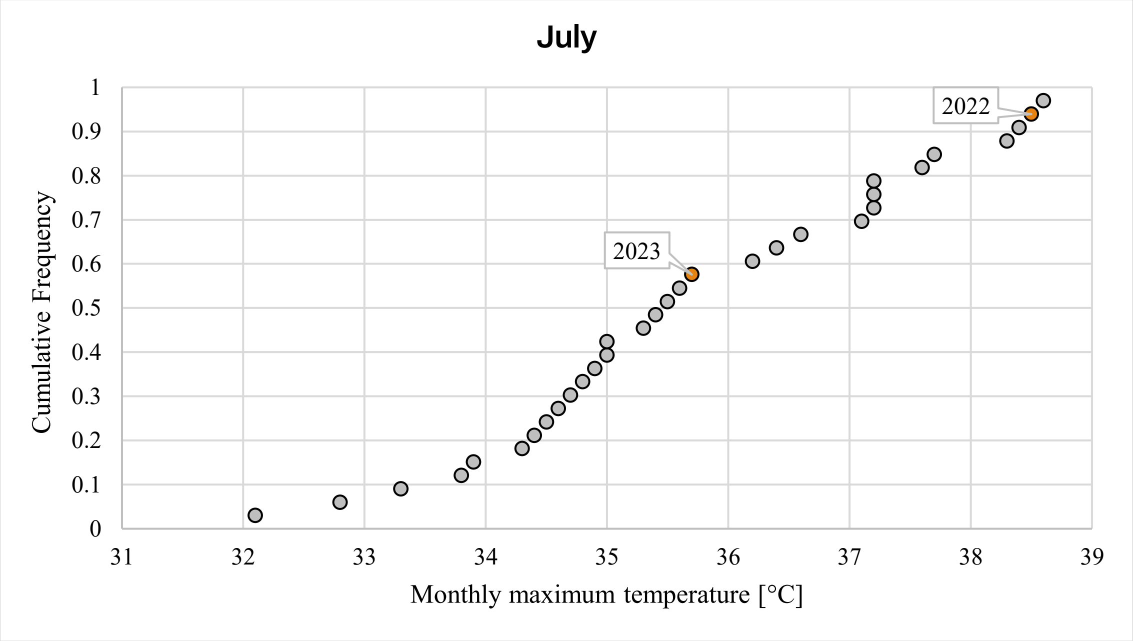

Figure 2.21. Cumulative frequencies of the monthly maximum temperature values of July of the historical series (1992-2023). In red, 2022 and 2023 are highlighted.

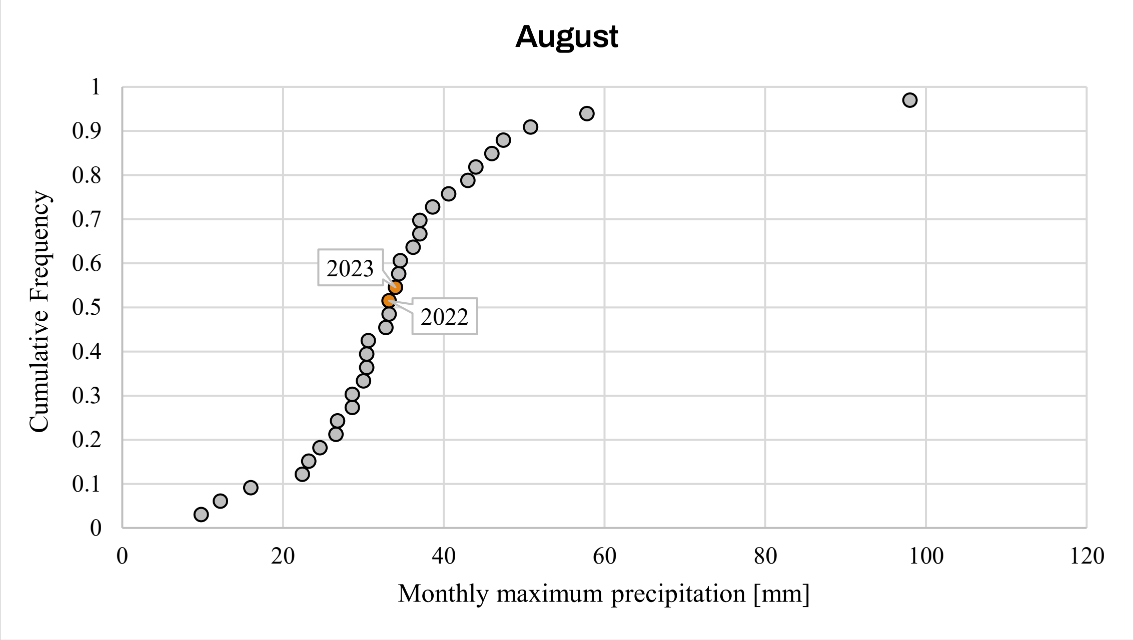

Figure 2.22. Cumulative frequencies of the monthly maximum precipitation depths of August of the historical series (1992-2023). In red, 2022 and 2023 are highlighted.

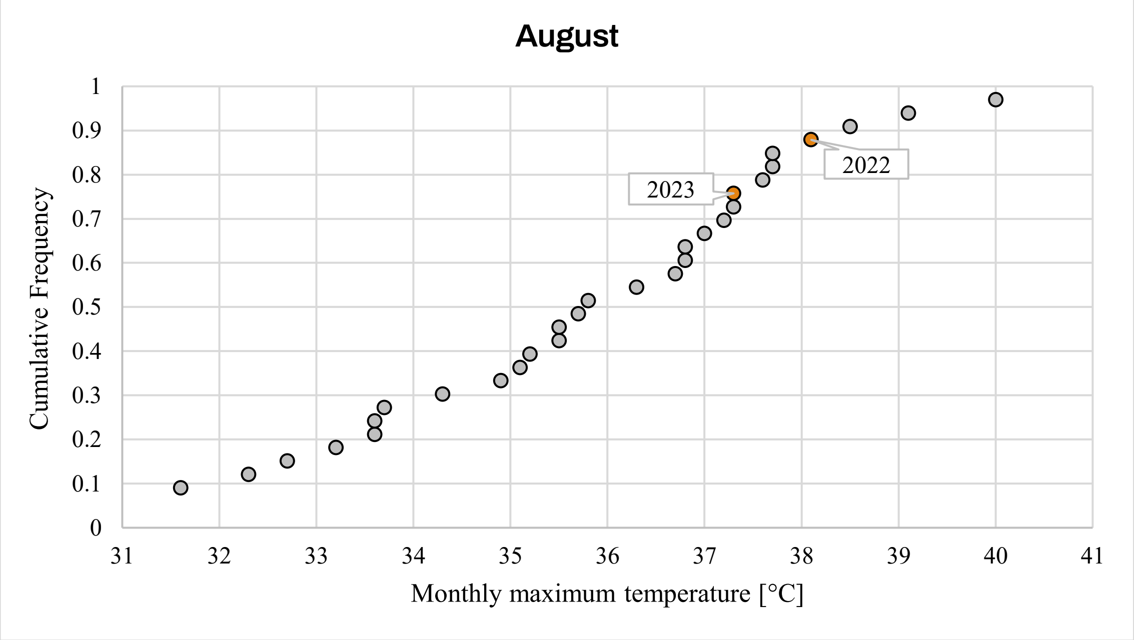

Figure 2.23. Cumulative frequencies of the monthly maximum temperature values of August of the historical series (1992-2023). In red, 2022 and 2023 are highlighted.

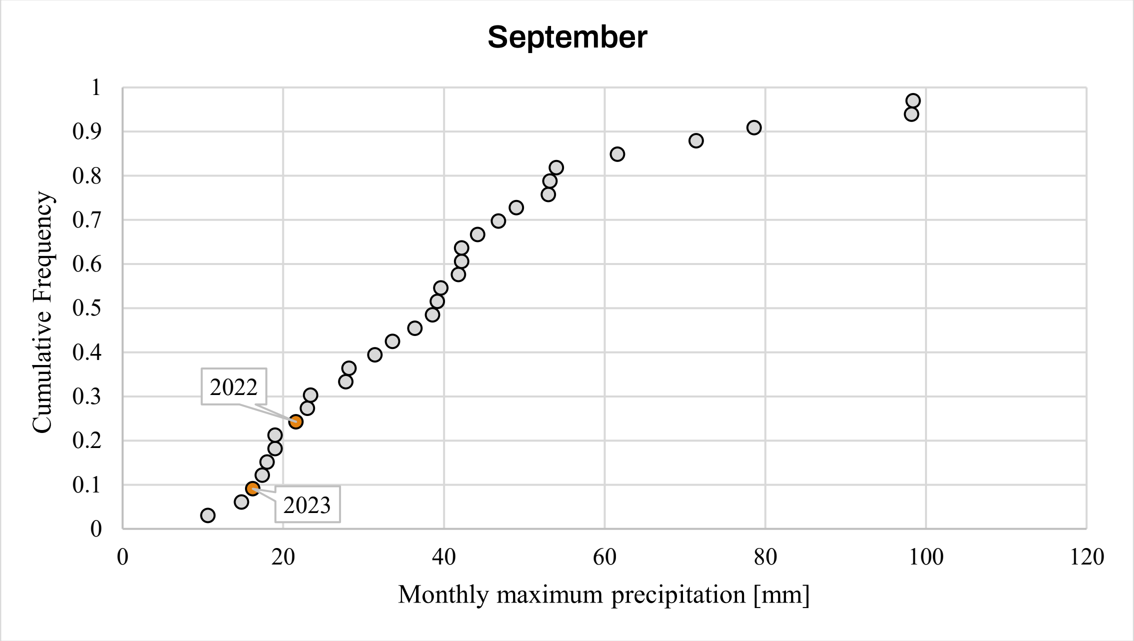

Figure 2.24. Cumulative frequencies of the monthly maximum precipitation depths of September of the historical series (1992-2023). In red, 2022 and 2023 are highlighted.

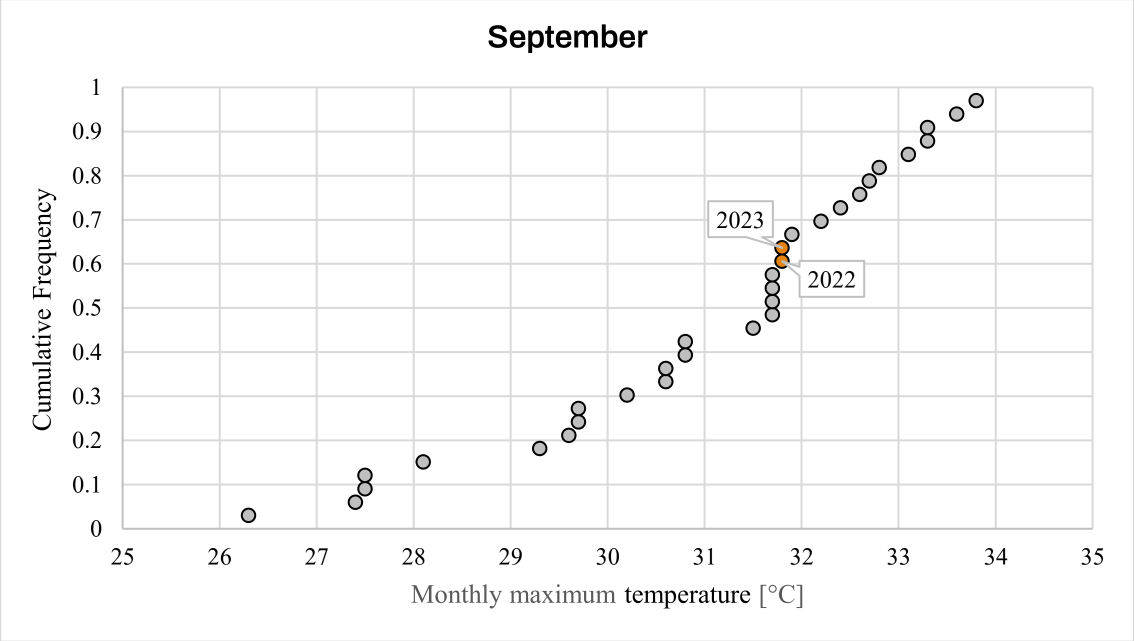

Figure 2.25. Cumulative frequencies of the monthly maximum temperature values of September of the historical series (1992-2023). In red, 2022 and 2023 are highlighted.

2.2.2. LI-600

Field measurements were performed utilizing the Porometer/Fluorometer LI-600, a product of the LI-COR Biosciences company, a leading innovator in developing instruments for environmental and biotechnological research, established in 1971 [67]. Among the various leaves and environment measurements that the instrument is capable of providing, the three parameters that were used in this study are:

1. Stomatal conductance (g_{sw}), which is a measure of how easily gases pass through the stomata. It can be employed as an indicator of water status of plants since it is connected to the degree of stomatal opening [68]. Synthetically, if stomata are more open, conductance is greater, and thus photosynthesis and transpiration rates are potentially higher.
2. Apparent transpiration T_a, calculated based on a mass balance of water vapor in an open system at a steady state. In general, high values of transpiration are characteristic of healthy and growing plants, while low amounts of transpiration are indicative of senescing or unhealthy plants.
3. Leaf temperature T_{leaf} , that is measured through a non-contact infrared thermometer (IRT) [69]. It is a good indicator of plant water stress, as stomata close, reducing transpiration and therefore the evaporative cooling, resulting in warmer leaves [70].

The values of these important leaf parameters were used to validate the satellite indices' values, to check whether they can provide an effective description of the health conditions of the soybean plants.

With regards to Figure 2.26, the main components of the instrument used in this study are:

a. Aperture (number 1) of 0.75 cm in diameter, which surrounds the leaf and takes the measurement.
b. Aperture clamp (number 2), that closes onto the leaf.
c. Fluorometer (number 3), which measures the amount of chlorophyll fluorescence.

d. Quantum sensor (number 4), which measures the light level of the environment.
e. Display (number 6), where measurements and instrument settings can be viewed.
f. Porometer (number 13), which is a steady-state gas exchange system that determines the stomatal conductance.

When the instrument turns on, a configuration must be selected among Auto and Manual Mode: the former automatically logs a measurement when certain stability criteria are met, whereas the latter does not. In Auto Mode, the display shows the prompt "Clamp on leaf": at that point, the user opens the aperture with the aperture clamp and close it onto the leaf (see Figure 2.27). The instrument will automatically search for stability and log the measurement; when the stability criteria are met, a beep sound informs the user to unclamp the leaf [71].

The LI-600 measurements were taken throughout soybean cultivation, from planting to harvest, at the time of maximum stress for plants due to the maximum solar radiation value, so between noon and 1 p.m., with many exceptions, especially in 2022, where some measurements were taken from 9 a.m. to 11 a.m. 120 leaf measurements were taken each day (30 for each subplot), ensuring optimum light conditions by operating only with a clear sky, without clouds. The dates of the acquisitions are listed in Table 2.14.

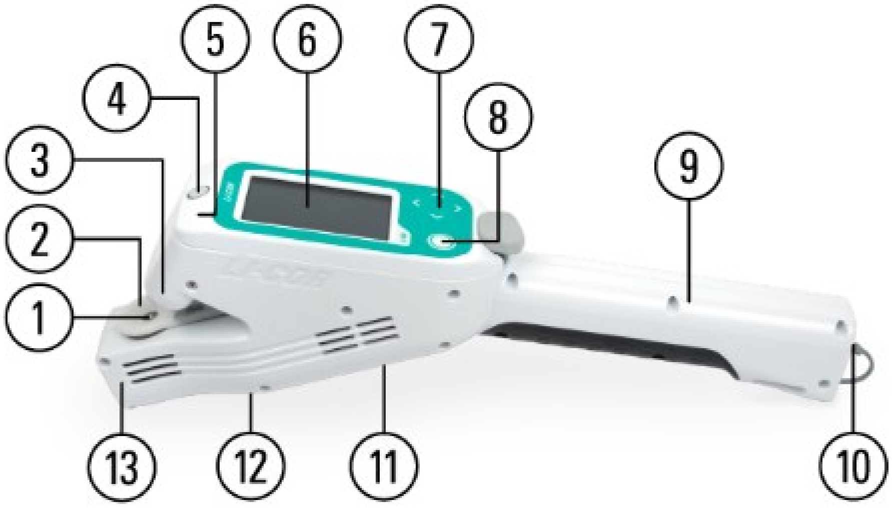

Figure 2.26. LI-600 components [69].

Table 2.14. Dates of the LI-600 acquisitions for 2022 and 2023.The highlighted dates refer to acquisitions taken between 9 and 11 a.m., hence not at the time of maximum stress for plants.

JUNE	20/06/2022	19/06/2023
	24/06/2022	27/06/2023
JULY	04/07/2022	05/07/2023
	09/07/2022	07/07/2023
	12/07/2022	12/07/2023
	18/07/2022	20/07/2023
	27/07/2022	28/07/2023
AUGUST	01/08/2022	02/08/2023
	06/08/2022	09/08/2023
	12/08/2022	17/08/2023
	24/08/2022	23/08/2023
SEPTEMBER	03/09/2022	01/09/2023
	13/09/2022	06/09/2023
	22/09/2022	12/09/2023

Figure 2.27. Clamp and measurement of the leaf with LI-600 [71].

2.3. Remote sensing data

2.3.1. Satellite characteristics

The two datasets for the soybean crop have been provided by two satellites with different spatial and temporal resolutions, namely Planet and Sentinel-2.

The PlanetScope satellite constellation is funded by the Planet private company, and it consists of about 130 individual Dove satellites, acquiring daily images with three meters per pixel resolution. Each Dove is a CubeSat 3U small satellite, with dimensions 10 cm by 10 cm by 30 cm, following a sun-synchronous orbit. In this work, the information gathered by the newest SuperDove instruments was employed: launched in early 2020, they carry the PSB.SD multispectral telescope, that captures scenes of the landscape of the approximate size of 32.5 km by 19.6 km in eight spectral bands as in Table 2.15. Each acquisition is referred to as PlanetScope Ortho Scene Product Level 3B, which represents radiometrically-, geometrically-, and sensor-corrected data, and is projected to a UTM/WGS84 cartographic map projection [72, 73, 74]. The satellite covered the soybean field between 9 and 10 A.M. every day, defining a dataset of 68 and 53 acquisitions in 2022 and 2023, respectively.

The Copernicus Sentinel-2 mission by the European Space Agency (ESA) is formed by a constellation of two satellites only, Sentinel-2A and Sentinel-2B, launched on June 23rd, 2015, and March 7th, 2017, respectively [75]. The two technologies follow the same sun-synchronous orbit, but with a phase difference of 180°, so that the revisit time of the overall mission scales down to 5 days at the Equator [76]. Both Sentinel2A/B have the MultiSpectral Instrument (MSI) onboard, which breaks the light into thirteen bands, with different spectral resolutions (Table 2.16). In particular, where available, the bands have been downloaded as Level-2A (L2A) Collection1 product, which provides orthorectified, radiometrically and geometrically corrected surface reflectance of the Bottom-Of-Atmosphere (BOA) [77]. When this level of correction was not available (only one image in the entire series), the Level-1C (L1C) Top-Of-Atmosphere (TOA) product was downloaded. The dataset defined by Sentinel2 consists of 17 and 18 acquisitions for 2022 and 2023, respectively. The correspondence between Sentinel-2 and PlanetScope bands is shown in Table 2.17.

Table 2.15. Spectral bands of PlanetScope PSB.SD instrument [72].

BAND	NAME	WAVELENGTH	RESOLUTION
1	Coastal Blue	431 – 452 nm	3 m
2	Blue	465 – 515 nm	3 m
3	Green I	513 – 549 nm	3 m
4	Green	547 – 583 nm	3 m
5	Yellow	600 – 620 nm	3 m
6	Red	650 – 680 nm	3 m
7	RedEdge	697 – 713 nm	3 m
8	NIR	845 – 885 nm	3 m

Table 2.16. Spectral bands of the Sentinel-2B MultiSpectral Instrument (MSI) [78]. In this case, the central wavelength is indicated. SWIR is the acronym for ShortWave InfraRed.

BAND	NAME	WAVELENGTH	RESOLUTION
1	Coastal/Aerosol Blue	443 nm	60 m
2	Blue	490 nm	10 m
3	Green	560 nm	10 m
4	Red	665 nm	10 m
5	RedEdge	705 nm	20 m
6	RedEdge	740 nm	20 m
7	RedEdge	783 nm	20 m
8	NIR	842 nm	10 m
8A	Vegetation RedEdge	865 nm	20 m
9	Water Vapor	945 nm	60 m
10	SWIR Cirrus	1375 nm	60 m
11	SWIR	1610 nm	20 m
12	SWIR	2190 nm	20 m

Table 2.17. Correspondence between Planet and Sentinel-2 spectral bands [79].

PLANET	NAME	CORRESPONDENCE TO SENTINEL
1	Coastal Blue	Band 1 – Coastal Blue
2	Blue	Band 2 – Blue
3	Green I	No
4	Green	Band 3 – Green
5	Yellow	No
6	Red	Band 4 – Red
7	RedEdge	Band 5 – RedEdge
8	NIR	Band 8A – Vegetation RedEdge

2.3.2. Vegetation Indices and crop parameters

Four different VIs were calculated with both spectral bands of Planet and Sentinel2:

1) *Normalized Difference Vegetation Index (NDVI)*

NDVI uses the visible and NIR bands to detect the presence of green vegetation. It is calculated as:

$$NDVI = \frac{NIR - Red}{NIR + Red} \tag{2.1}$$

It ranges from -1 to 1, and in particular, it has negative values for water bodies, close to zero for rocks, sands, or concrete surfaces, and positive for vegetation [80]. Specifically, the higher the NDVI, the healthier and denser the vegetation: values between 0.1 and 0.5 indicate sparse vegetation, while NDVI major than 0.6 relates to dense green vegetation [81]. In Table 2.18, a more specific review of the index values and their respective correct interpretation is explained.

Table 2.18. NDVI values and their interpretation [82].

VALUES	INTERPRETATION
< 0.1	Bare soil or clouds
0.1 – 0.2	Almost completely absent vegetation cover
0.2 – 0.3	Extremely low vegetation cover
0.3 – 0.4	Low vegetation cover and vigor, or extremely low vegetation cover and high vigor
0.4 – 0.5	Medium to low vegetation cover with low vigor, or extremely low vegetation cover with high vigor
0.5 – 0.6	Medium vegetation cover, or medium to low vegetation cover with high vigor
0.6 – 0.7	Medium to high vegetation cover with low vigor, or medium vegetation cover with high vigor
0.7 – 0.8	High vegetation cover and vigor
0.8 – 0.9	Extremely high vegetation cover and vigor
0.9 - 1	Total vegetation cover with extremely high vigor

2) *Green Normalized Difference Vegetation Index (GNDVI)*

It is characterized by a higher sensitivity to chlorophyll absorption compared to NDVI, and hence it is used as a measure of the photosynthetic activity of vegetation cover [83]. Moreover, it is capable of detecting water and humidity. GNDVI works as NDVI, but with green in place of the red band:

$$GNDVI = \frac{NIR - Green}{NIR + Green} \tag{2.2}$$

The stretch of values of GNDVI is the same as NDVI (refer to Table 2.18).

3) Enhanced Normalized Difference Vegetation Index (ENDVI)

Based on the green band as GNDVI, ENDVI is more recommended to detect vegetation vigor [84]. It works as such:

$$ENDVI = \frac{NIR + Green - 2 * Blue}{NIR + Green + 2 * Blue} \tag{2.3}$$

Being a modification of NDVI, the different values reflect the same vegetation characteristics as the original index (see Table 2.18).

4) Normalized Difference RedEdge index (NDRE)

It measures the chlorophyll content in plants, derived from a combination of NIR and RedEdge band:

$$NDRE = \frac{NIR - RedEdge}{NIR + RedEdge} \tag{2.4}$$

In general, the best performance of NDRE occurs in the mid-to-late growing season, with the other indices that are less effective to be used. Values comprised between -1 and 0.2 indicate bare soil or developing crop; 0.2 to 0.6 NDRE amounts can be translated as either unhealthful plant or a not mature crop; and finally, values between 0.6 to 1 indicate healthy and mature crops [85].

5) Leaf Area Index (LAI)

The Leaf Area Index has been calculated following the correlation with another index, named EVI, proposed by Boegh et al. (2002) [44]. According to the researchers, EVI can be calculated as:

$$EVI = \frac{2.5(NIR - Red)}{(NIR - C_1 \cdot Red - C_2 \cdot Blue + L)} \tag{2.5}$$

With coefficients $C_1 = 6, C_2 = 7.5, L = 1$. LAI can be effectively derived from EVI (with a correlation coefficient $R^2 = 0.77$) as:

$$LAI = 3.618 \cdot EVI - 0.118 \tag{2.6}$$

A typical LAI pattern begins with a slow increase early in the season, followed by a rapid rise until a maximum value is reached; then, LAI declines as leaves senesce and plants reach physiological maturity [86].

The bands 5 and 8A have a twenty meters spatial resolution in Sentinel (see Table 2.16). For the calculation of the indices with a spatial resolution of ten meters, a reprojection of the two bands was performed with the “Warp (Reproject)” command in QGIS. The resampling method chosen for this purpose is the bilinear interpolation, which computes the weighted average of the four nearest neighboring cells based on their distance from the output cell [87]. Once each index was computed, the maximum, minimum, average, and standard deviation values were obtained through the “Zonal Statistic” command, applied to the mask layer representing the two zones (RDI and FI) in each year.

The Sentinel results were then compared to the Planet indices by plotting the correlation curve, with Planet outcomes on the x-axis and Sentinel values on the y-axis, considering only the dates on which both values are available. The correlation coefficient is used to assess whether Sentinel’s spatial and temporal resolutions can adequately capture the trends of various indices throughout the soybean growth cycle, in comparison to the higher-resolution Planet data. Ideally, the values of the same index measured on the same date from two different satellites should be equal; therefore, the theoretical correlation line would be the bisector line, with slope equal to 1 and intercept equal to 0. In reality, most of the regression lines are not close to the ideal correlation, as slope and intercept values are estimations subjected to systemic errors. The difference between the slope and intercept of the regression lines and the corresponding coefficients of the bisector is evaluated for statistical significance using the Student’s t-test. This test determines whether to accept or reject the “null hypothesis” H_0, which states that the values are statistically equal. If H_0 is rejected, the "alternative hypothesis" H_1, which claims the values are not statistically equal, is accepted [88]. In this context, H_0 affirms that the slope/intercept of the regression line of each index is statistically equal to the slope/intercept of the bisector, whereas H_1 states that the two quantities are significantly different. The t value for the slope, for example, is calculated as follows:

$$t = \frac{m_{regr} - m_{corr}}{SE_{m_{regr}}} \tag{2.7}$$

With $SE_{m_{regr}}$ the standard error associated with the slope of the regression line m_{regr}, calculated with the Data Analysis tool in Excel. The calculated t-value is compared to the critical t-value corresponding to a chosen significance level α (taken equal to 0.05) and degrees of freedom, which are equal to the number of observations minus 2. If the absolute value of t is higher than the critical $t_{0.05;N-2}$, the null hypothesis must be rejected, indicating that the difference between the two slopes/intercepts is statistically significant. However, if $|t| < t_{0.05;N-2}$, the null hypothesis is accepted, meaning that the slope/intercept of the regression line can be considered statistically equal to those of the bisector.

3. RESULTS

3.1. Planet indices

3.1.1. 2022

The calculations of NDVI (Figure 3.1), GNDVI (Figure 3.2), ENDVI (Figure 3.3), NDRE (Figure 3.4), and LAI (Figure 3.5) using Planet bands resulted in four curves that follow a similar trend for 2022. Although the overall upward trend of the curves is consistent across all indices, their values differ significantly.

3.1.1.1. Early growth stages (BBCH 00-19)

During the early growth stages, from germination to leaf development, relatively low rainfall and warm temperatures occurred, especially during late May and early June. Precipitation was sparse, contributing to low soil moisture, which could explain the variability and lower values in the indices, perduring until June 12th (BBCH 19).

Specifically, while NDVI values increase from 0.30 to 0.40 for both FI and RDI subplots, GNDVI and ENDVI show higher amounts, ranging from 0.37 to 0.51 and 0.36 to 0.63, respectively. The generally low rainfall in June (10 rainy days, mostly dry) combined with high temperatures likely led to limited early vegetative growth, which might explain why indices like NDVI showed a slower increase compared to GNDVI and ENDVI, as they capture different aspects of vegetation health, indicating the beginning of the photosynthetic activity. ENDVI, in particular, reveals a significant variability in the values, that are more scattered and follow less precisely the upward trend defined by the other indices. On the other hand, NDRE displays lower amounts, in the range 0.22-0.30, with minimal differences between FI and RDI subplots. LAI is also highly variable in this initial stage, with values oscillating from 1.40 to 3.19 in FI and from 1.33 to 3.00 in RDI subplots, which could reflect the uneven early development of leaf area. Its values stabilize in proximity of the onset of the next BBCH stage.

3.1.1.2. Vegetative Growth stage (BBCH 20-59)

From June 12th to mid-July, the vegetation indices show a clear upward trend, continuing until the flowering stage (BBCH 60) around July 20th. This significant increase in plant cover and vigor coincides with the start of irrigation on June 14th. Despite the challenging climatic conditions, including a heatwave from mid- to late June, the absence of rainfall until the last days of the month, and prolonged drought conditions throughout most of July, the VIs continued to rise steadily. This consistent growth, however, was almost only sustained by the irrigation water supply, as natural precipitation was almost non-existent during this critical period.

During this time, NDVI rises faster compared to the other indices. Specifically, NDVI increased from 0.31 and 0.30 on June 12th to 0.77 and 0.75 by July 17th for FI and RDI subplots, respectively. This steep increase can be attributed to the fact that NDVI is sensitive to the presence of green biomass, and irrigation quickly boosted the leaf area and canopy cover. In contrast, GNDVI is equal to 0.45/0.44 and 0.73/0.72, ENDVI to 0.50/0.50 and 0.72/0.70, and NDRE to 0.22/0.21 and 0.60/0.58 for FI and RDI, respectively. These slower rises were influenced by the harsh climatic conditions, which affected plant responses related to chlorophyll content, photosynthetic activity, canopy structure, and overall stress. The heatwaves, with temperatures peaking at 35°C, slowed the plants' recovery in terms of chlorophyll, as captured by GNDVI and NDRE. Similarly, LAI follows the same upward trend, going from values of 1.67 (FI) and 1.57 (RDI) to 7.43 (FI) and 6.96 (RDI) by the start of the flowering stage. The slower rise in LAI and ENDVI, which track canopy development and structure respectively, suggests that while irrigation supported growth, the extreme heat and lack of rainfall slowed the full development of the canopy.

3.1.1.3. Flowering and Development of fruit and seeds stages (BBCH 60-79)

In late July and August, the VIs show slower growth rates as the flowering stage begins, coinciding with the peak of the growing season and a slight moderation of extreme heat events. Rainfall increased in August (112.6 mm), with a significant rain event from August 15th to 18th (60.6 mm), which likely provided a boost to plant growth, especially since irrigation was still ongoing.

At the end of the flowering stage (BBCH 69), all indices increased by 0.04-0.05. LAI in this period shows high variability as in the initial period, with values oscillating between 7.21 and 8.27 for FI subplots and between 7.07 and 8.01 for RDI areas.

During the Development of fruit and seeds stage (BBCH 70-79), the indices fluctuate within the following ranges:

- NDVI varies between 0.80 and 0.89 in FI, and from 0.77 to 0.89 in RDI subplots.
- GNDVI ranges from 0.75 to 0.84 in FI, and from 0.72 to 0.83 in RDI subplots.
- ENDVI values show higher variability, fluctuating between 0.70 and 0.87 in FI, and 0.60 and 0.86 in RDI subplots.
- NDRE remains lower, moving between 0.64 and 0.74 in FI, and 0.59 and 0.72 in RDI.

Each index reaches its peak value on August 23rd, indicating strong vegetative health. However, this does not hold for LAI, which values range between 7.9 and 9.1. The peaks occur on different dates for FI and RDI subplots: the FI highest value equals 9.11 on August 30th, while RDI subplots peaks at same value on August 12th (BBCH 73).

3.1.1.4. Ripening of fruit and seeds and Senescence stages (BBCH 80-99)

During the ripening (BBCH 80-89) and senescence stages (BBCH 90-99), all indices begin to decline, reflecting the natural process of plant aging and reduced vegetative activity. This coincided with a general decrease in temperatures, with a significant drop after the hail event happened on September 17th. Contemporarily, precipitation amounts increased consistently, counting 16 days of rain, therefore drastically reducing the climatic stress condition that perdured throughout all the other growing stages. The final measurements, taken on October 3rd (the day before harvest, BBCH 98), show indices ranging between 0.62-0.69 in FI subplots and 0.59-0.66 in RDI subplots, except for NDRE, which ends at much smaller values (0.38 and 0.37, respectively). Similar to the early growth phase, the NDVI's downward slope is particularly steeper than that of GNDVI and ENDVI, resulting in smaller final values. LAI is halved during this period, dropping from 8.37 on September 10th in both FI and RDI subplots to values of 4.46 (FI) and 4.12 (RDI) on October 3rd.

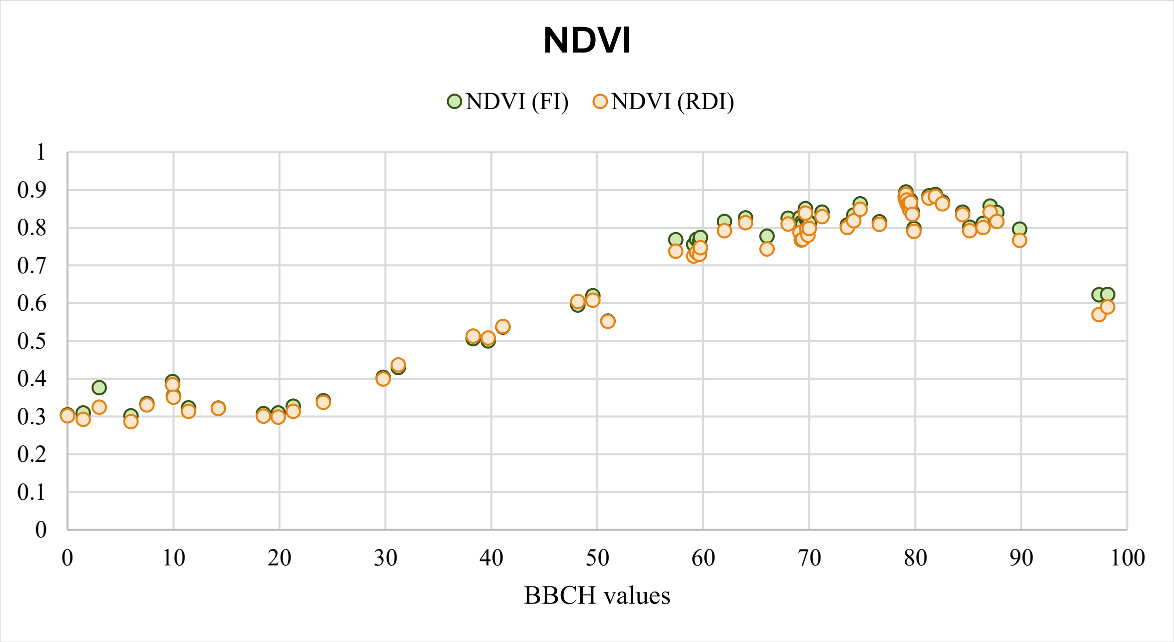

Figure 3.1. NDVI values obtained from Planet bands for 2022.

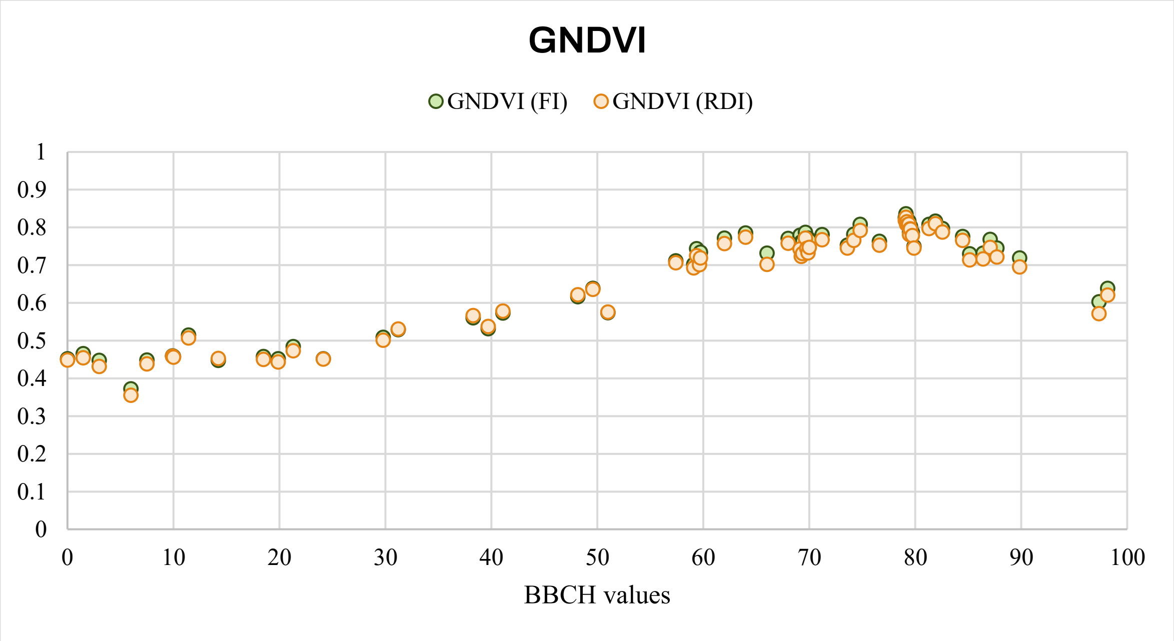

Figure 3.2. GNDVI values obtained from Planet bands for 2022.

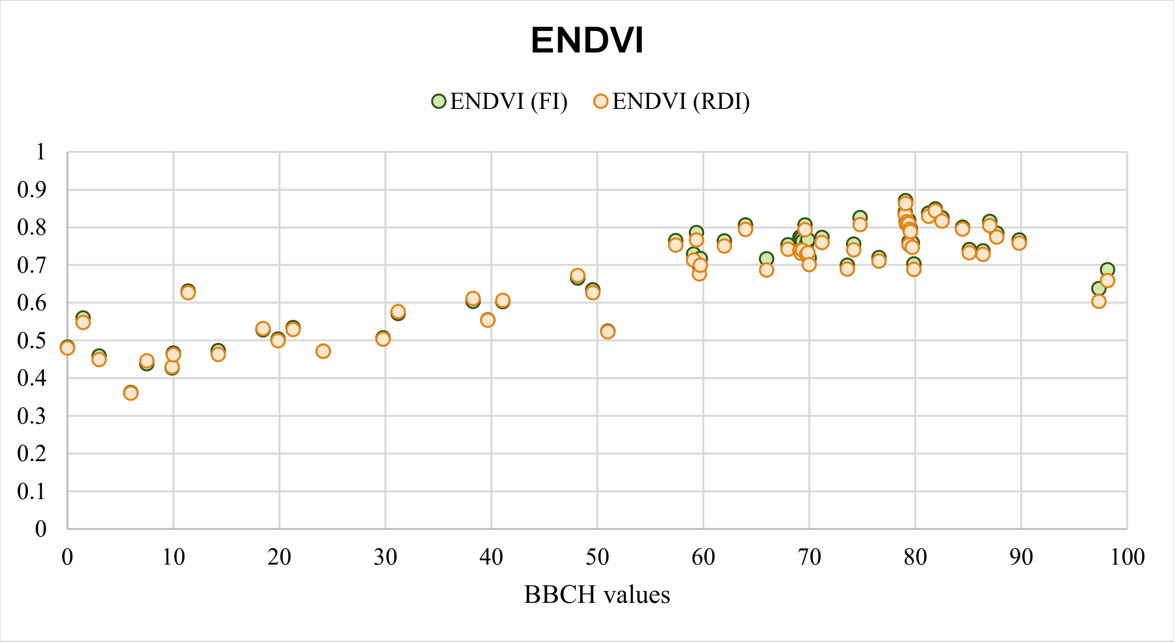

Figure 3.3. ENDVI values obtained from Planet bands for 2022.

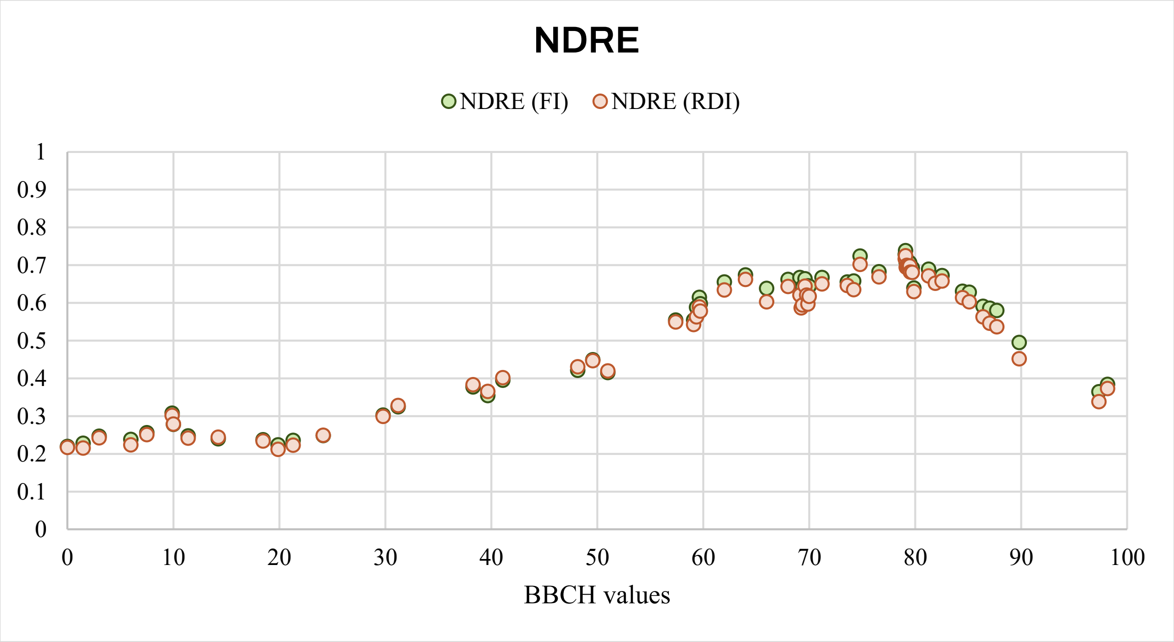

Figure 3.4. NDRE values obtained from Planet bands for 2022.

All indices measured higher values in the FI subplots compared to those recorded in the areas subjected to RDI, with few exceptions. However, the mean differences between the two are generally small for each index, as illustrated in Figure 3.6. Specifically, NDRE exhibits the largest mean difference between FI and RDI values, measuring 0.150, along with the highest standard deviation (σ) of 0.0144. The NDVI followed closely, with a mean difference of 0.0142 and a similar σ (0.0142). GNDVI and ENDVI recorded smaller mean differences, with minimal variability as indicated by standard deviations of 0.010. LAI exhibits similar results, showing minimal differences and variability between the values measured in the FI and RDI subplots, with a mean difference of 0.177 and σ of 0.22. Nonetheless, these mean differences turned out to be statistically significant. It is interesting to note that the divergence between FI and RDI varies over specific soybean growing stages and on the basis of RDI application (**Error! Reference source not found.**). The least d ifferences are recorded over the early growing stages (BBCH 00-49), from the germination to the end of the development of harvestable material stages. These differences decrease starting from the irrigation onset (BBCH 20). During the inflorescence emergence stage (BBCH 50-59), when RDI was halted, the differences between the indices slightly increased.

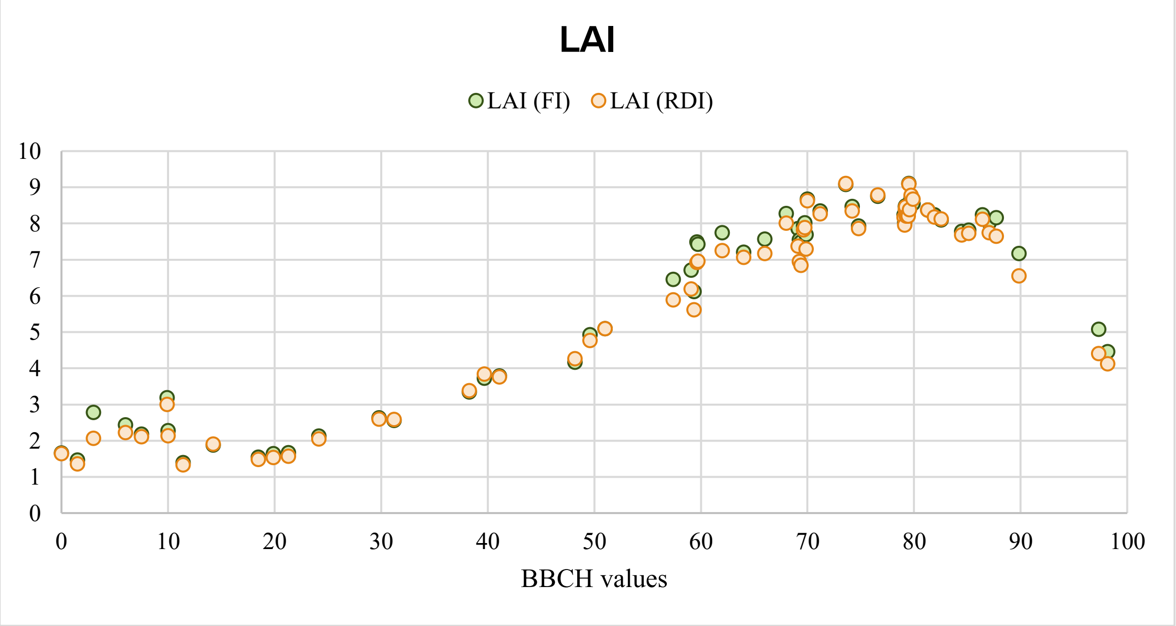

Figure 3.5. LAI values obtained from Planet bands for 2022.

This may be linked to earlier variations, as the water volume applied during this stage is the same for both subplots. In contrast, the flowering stage (BBCH 60-69), when RDI resumed, displays the highest difference, along with the final senescence stage (BBCH 90-99), during which the behavior of plants under FI and RDI seems to differ more significantly. The difference decreases during the stages of development (BBCH 70-79) and ripening of fruit and seeds (BBCH 80-89) for all indices except for NDRE, which trend in this latter stage deviates from the other indicators, almost doubling. This could be related to the higher sensitivity of NDRE to the late stages of crops, due to the use of the RedEdge wavelength, making it preferable in measuring crop parameters when plants start becoming mature to the point where they are chlorophyll-saturated and red light is no longer properly absorbed.

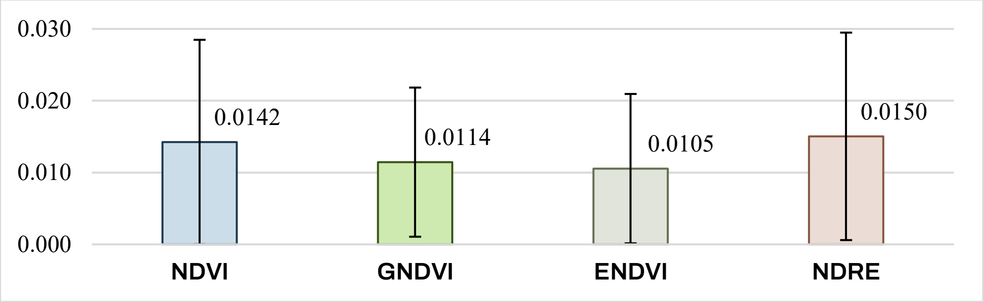

Figure 3.6. Mean difference (indicated by the label) in the Planet indices between FI and RDI subplots in 2022 with its standard deviation.

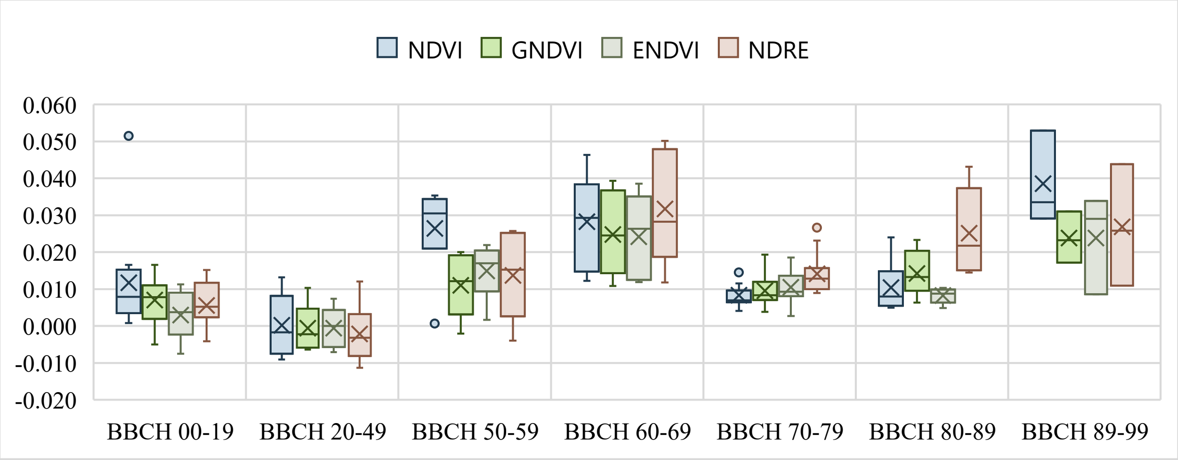

Figure 3.7. Mean difference in the Planet indices values in FI and RDI subplots at different BBCH soybean growing stages in 2022.

3.1.2. 2023

The trend of the indices in 2023 (displayed in Figure 3.8, Figure 3.9, Figure 3.10, Figure 3.11, and Figure 3.12) closely mirrors that of 2022, both in terms of values and the periods of upward and downward movements. However, the indices in the RDI subplots are consistently higher than those in the FI subplots for most of the soybean growing season.

3.1.2.1. Early growth stages (BBCH 00-19)

From May 31st (day of plantation) to June 19th (BBCH 19), temperatures were moderate compared to 2022, always staying between 23.5°C and 30°C. The milder temperatures allowed for a more favorable environment for early-stage growth, avoiding the early season heat stress observed in 2022. Moreover, precipitation was frequent and abundant but not excessive, with total depth of 70.2 mm distributed over 12 days.

During this period, all indices experience a slight increase, with differences between their values that are close to those measured in the same period in 2022. In particular, NDVI and NDRE values oscillates within the same intervals (0.27-0.40 for NDVI, 0.22-0.30 for NDRE across all subplot), but GNDVI, ENDVI, and LAI already start with higher amounts but end lower compared to 2022. GNDVI rises from 0.43 to 0.47 and 0.49 for FI and RDI subplots, respectively, while ENDVI registers ranges of 0.44-0.50 for FI, 0.44-0.51 for RDI. LAI begins at 1.47 and 1.55 for FI and RDI on the first acquisition and increases to 2.49 and 2.69, respectively, by BBCH 19. These indices capture the response of plants to better water availability, which supported early vegetative growth, chlorophyll production, and the formation of a denser canopy.

3.1.2.2. Vegetative Growth stage (BBCH 20-59)

Between June 20th and July 24th, all VIs exhibit a much steeper upward trend compared to 2022. This steep rise can be linked directly to the intense rainfall event from July 3rd to July 6th, which delivered over 81 mm of precipitation in just a few days, significantly boosting soil moisture levels. Additionally, temperatures during this period were moderate, with highs exceeding 35°C only on two occasions in mid-July, contributing to more favorable climatic conditions compared to 2022.

NDVI, in particular, increased dramatically, rising from 0.46 in FI and 0.48 in RDI to 0.87 and 0.88, respectively, by BBCH 59. NDRE followed a similar steep increase, jumping from around 0.30-0.31 on June 25th to 0.70-0.71 by July 20th. These indices reflect a robust increase in canopy cover and chlorophyll content, largely sustained by the timely availability of water. Although GNDVI and ENDVI also showed an upward trajectory, their increases were less pronounced compared to NDVI and NDRE, starting at around 0.49 on BBCH 20 and reaching 0.82 by BBCH 59. LAI also shows higher values compared to 2022, peaking at 9.31 and 9.20 for FI and RDI, respectively. By BBCH 59, LAI values in FI subplots surpass those in RDI plots and remain higher until BBCH 79 (late fruit and seed development).

3.1.2.1. Flowering and Development of fruit and seeds stages (BBCH 60-79)

As the plants entered the flowering stage (BBCH 60-69), growth slowed noticeably, with values increasing by only 0.04-0.05, similar to what was observed in 2022. Frequent rainfall made irrigation unnecessary, as the rainwater sustained plant growth, allowing the indices to rise, albeit at a slower rate. LAI, however, shows a sharp decline around July 26th (BBCH 60), dropping from 9.0-9.1 to 8.2 and 8.0 for FI and RDI, respectively. This reduction in canopy density is likely due to the plant's natural shift in energy allocation toward reproductive processes during flowering. The LAI later recovered, peaking again at BBCH 69, reaching 9.56 and 9.43 for FI and RDI. Temperatures during the flowering stage were relatively mild compared to the extreme conditions of 2022, with maximum temperatures ranging between 28-30°C. This, coupled with sufficient moisture from the earlier rainfall, likely helped the canopy recover quickly. In contrast, the NDRE peaked on the same day, reaching 0.89 and 0.88 for FI and RDI, respectively. This can be attributed to NDRE's sensitivity to chlorophyll content, especially in the deeper canopy layers, as the RedEdge band penetrates deeper than the NIR. Despite the LAI decline, the remaining leaves likely retained high chlorophyll concentrations, as the plant continued photosynthesizing to meet the energy demands of flower and fruit development.

Unlike in 2022, where the vegetation indices continued to increase steadily until the end of the fruit and seed development stage, in 2023 the indices peaked earlier and began to decline around BBCH 70. This earlier decline may be attributed to the prolonged dry spell in

August, where no rainfall was recorded for 19 consecutive days from August 5th to August 24th. Despite the irrigation, the lack of rainfall combined with high temperatures (reaching up to 37.3°C from August 21st to 26th) likely induced early stress on the plants. Additionally, the peaks of the indices are no longer aligned as they were in 2022. Specifically:

- NDVI peaks at 0.91 in both FI and RDI subplots but on different dates: August 12 for FI and August 15 for RDI.
- GNDVI and ENDVI both peak on August 15 across all fields, measuring 0.85 and 0.87 in FI and 0.86 and 0.87 in RDI subplots, respectively.
- LAI, meanwhile, continued to increase until August 20th, when it reached a peak of 10.1 for both subplots. This reflects the canopy's final expansion phase before the onset of senescence.

The intense rainfall event on August 28-29th (totaling 67.8 mm) might have helped sustain the canopy cover and slow down the senescence process, though it was insufficient to prevent the gradual decline observed in the indices after BBCH 70.

3.1.2.2. Ripening of fruit and seeds and Senescence stages (BBCH 80-99)

Following these peaks, all vegetation indices began to decline steadily between BBCH 71 and BBCH 73. This earlier decline, compared to 2022, was likely driven by the extended dry period in August and the high temperatures that stressed the plants during the critical stages of fruit and seed development.

By harvest day (October 9th, BBCH 99), the final values for the indices range from 0.41-0.49 in FI and 0.45-0.51 in RDI. This does not stand for NDRE, which records much lower values (0.29 in FI and 0.31 in RDI), reflecting reduced chlorophyll content and plant vitality as the crop approach full senescence. Similar to the early growth stage, NDVI's decline is steeper than that of GNDVI and ENDVI, leading to lower final values. LAI is halved during this period, falling from 6.21 (FI) and 6.87 (RDI) on September 11th to 3.00 (FI) and 3.39 (RDI) by October 9th. The continued decline in all indices until the end of the growing season indicates that, despite the improved conditions earlier in the season, the lack of rain and sustained high temperatures during August and September ultimately accelerated the plants' progression into senescence.

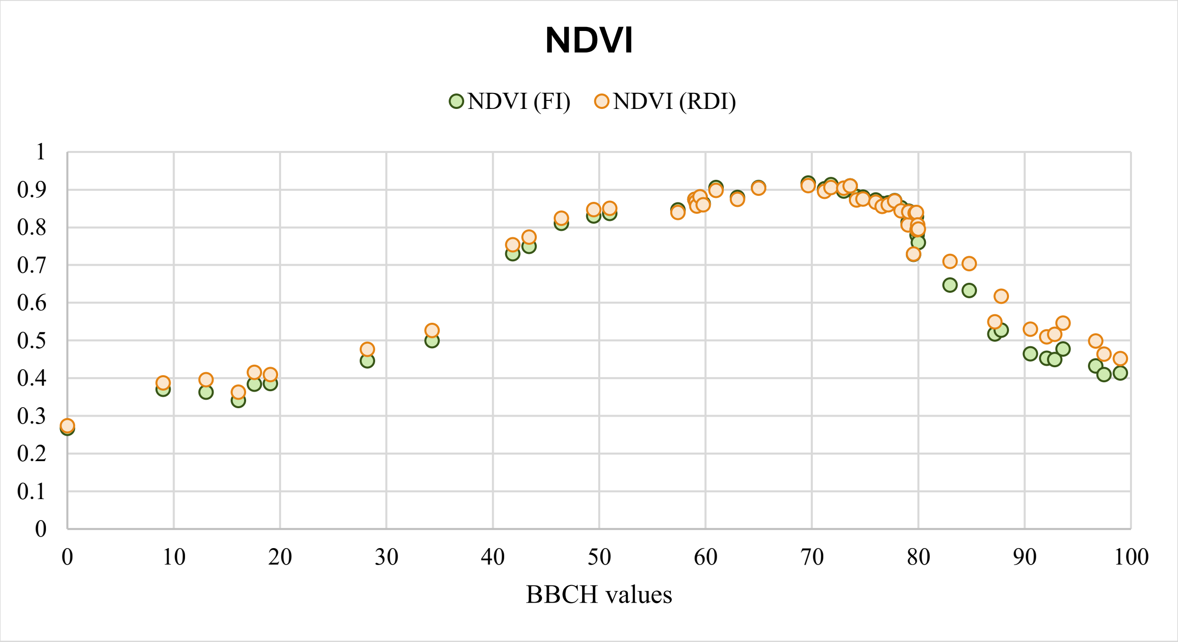

Figure 3.8. NDVI values obtained from Planet bands for 2023.

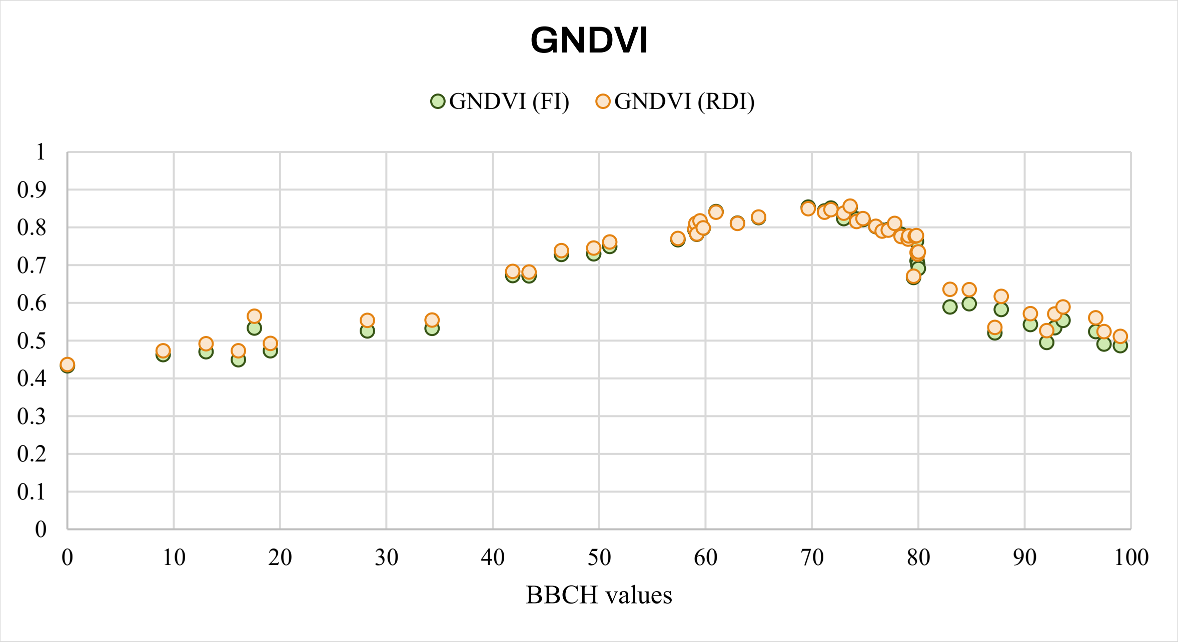

Figure 3.9. GNDVI values obtained from Planet bands for 2023.

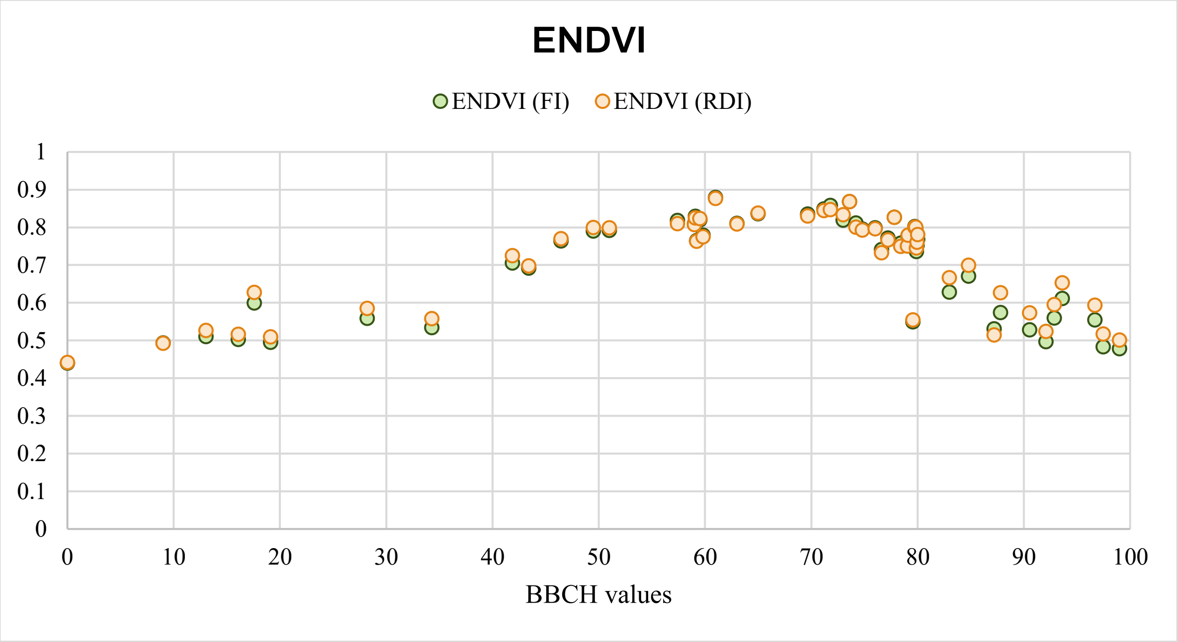

Figure 3.10. ENDVI values obtained from Planet bands for 2023.

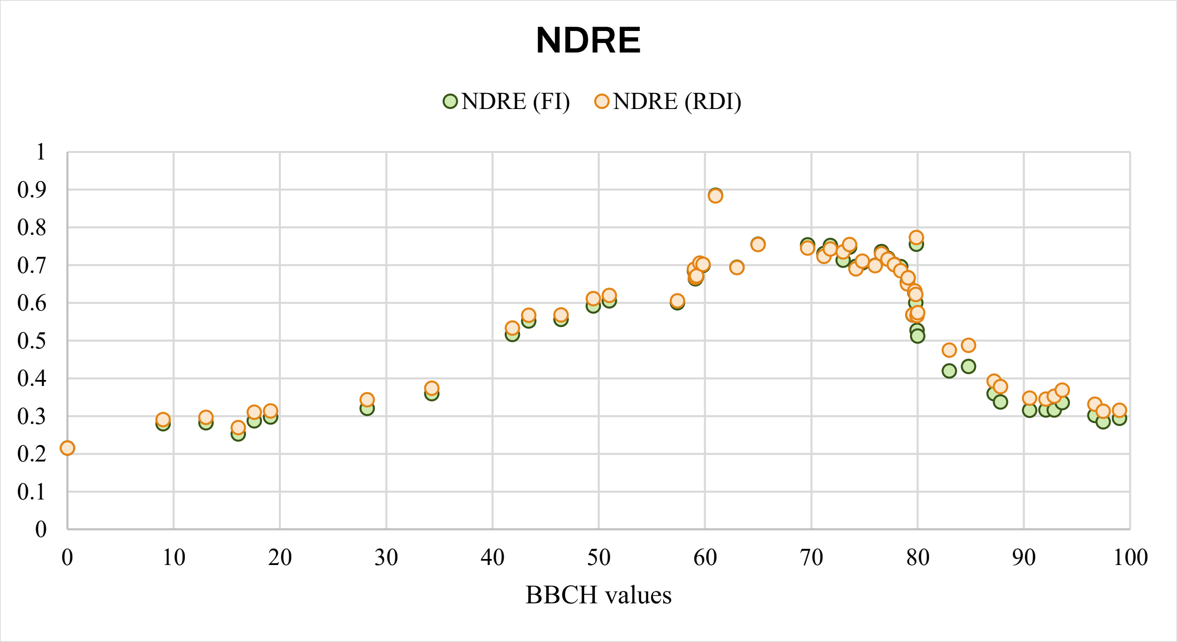

Figure 3.11. NDRE values obtained from Planet bands for 2023.

As aforementioned, the RDI subplots registered higher values of the indices than FI subplots, despite the lower volume of water supplied. The mean differences between the FI and RDI values (represented in Figure 3.13), in fact, exhibit negative values for all indices, indicating that RDI are on average higher than FI. In particular, the mean difference for NDVI between FI and RDI is approximately -0.0176, suggesting that vegetation health or vigor is marginally better under RDI compared to FI, but its values are subjected to great variability. GNDVI shows a mean difference of -0.0133, but with the lowest variability in terms of standard deviation compared to other indices, suggesting more consistent results. NDRE recorded similar results in terms of mean difference, but the standard deviation is slightly higher. Finally, ENDVI demonstrates the smallest mean difference, -0.0092, suggesting only a minor advantage for RDI over FI. Although LAI is the only index where FI values were higher than RDI for a certain period, its overall mean difference is still negative, indicating that RDI values were, on average, slightly higher than FI. However, this mean difference is quite small (-0.21) with a low standard deviation (0.36), suggesting that LAI did not capture

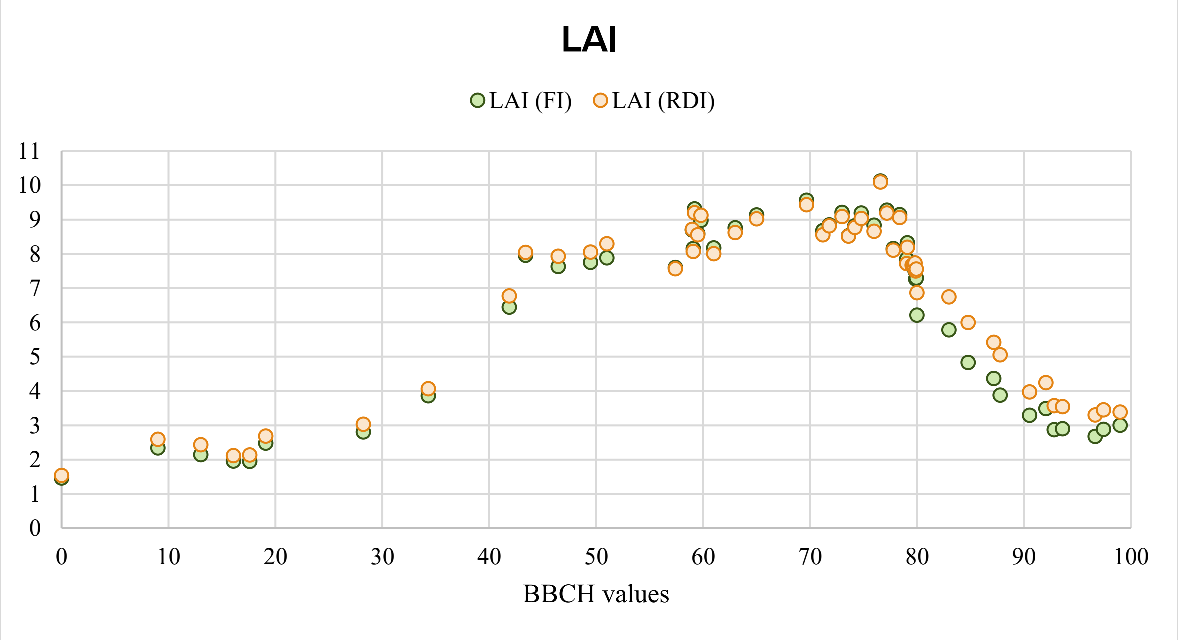

Figure 3.12. LAI values obtained from Planet for 2023.

significant differences between the two irrigation strategies in terms of vegetation growth and vigor. The most notable differences occur during the fruit and seeds development (BBCH 80-89) and senescence (BBCH 90-99) stages, where RDI appears to outperform FI in maintaining higher index values (Figure 3.14). However, throughout most stages, the differences remain small, suggesting that both irrigation strategies yield comparable outcomes for vegetation health,

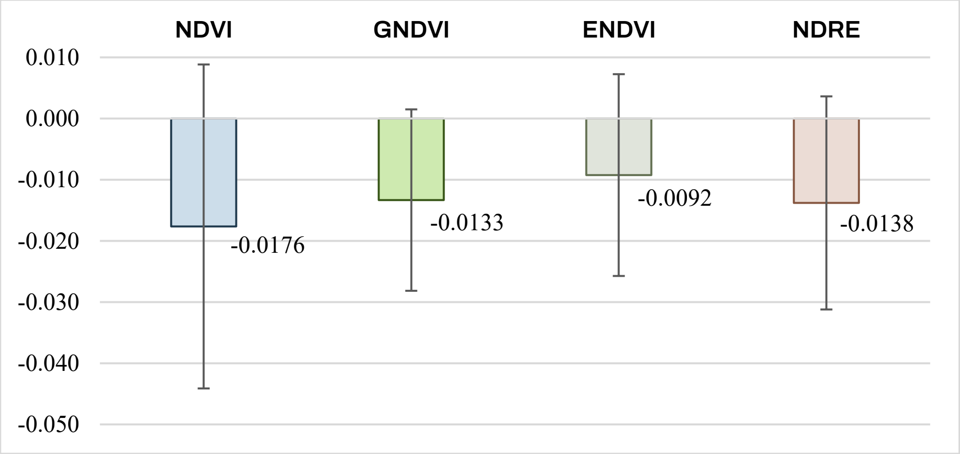

Figure 3.13. Mean difference (indicated by the label) in the Planet indices between FI and RDI subplots in 2023 with its standard deviation.

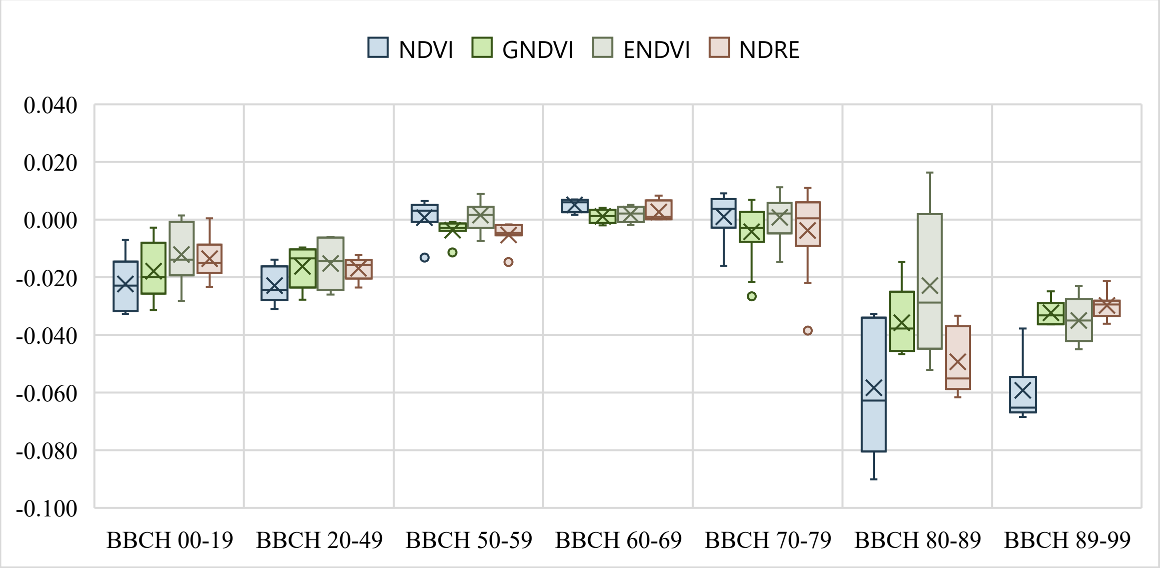

Figure 3.14. Mean difference in the Planet indices values in FI and RDI subplots at different BBCH soybean growing stages in 2023.

3.2. Comparison between Planet and Sentinel indices

The indices calculated with Sentinel bands appropriately align with the trend of each respective Planet's index in the years under consideration, but they are underestimated by the quantities explicated in Table 3.1. A statistical analysis revealed that the differences between Planet and Sentinel data are statistically significant for each index in both years. ENDVI is the index with the highest average difference between Planet and Sentinel values, whereas NDRE shows the closest match.

In particular, NDVI (Figure 3.15, Figure 3.16) is underestimated with respect to Planet by 0.213 – 0.227, but the correlation between the two outcomes (Figure 3.17) is very high in both 2023 (with a correlation coefficient of 0.984) and in 2022 (R^2 equal to 0.977), indicating that Sentinel NDVI values follow almost perfectly the trend of the index obtained with Planet in the same days of acquisition. GNDVI (Figure 3.18, Figure 3.19) also shows high correlation in both years (Figure 3.20), with R^2 equal to 0.938 and 0.981 in 2022 and 2023, respectively, underestimating the Planet outcomes a little bit less than NDVI. The ENDVI index indicates the worst alignment between the two satellite's results, with a difference of 0.30 – 0.32. Although the 2023 trend is quite similar to the Planet's ENDVI (Figure 3.22), in 2022 the curves are way less alike (Figure 3.21). As a result, the correlation coefficient for 2022 is 0.6882, much lower than R^2 for 2023, equal to 0.944 (Figure 3.23). Finally, NDRE values obtained with Sentinel are underestimating Planet outcomes by 0.147 – 0.154, and in fact the curves in Figure 3.24 and Figure 3.25 are closer one to another. The trend is also well described, with very high correlation coefficient in both years (Figure 3.26).

The computation of LAI based on EVI also gives good results, but Sentinel overestimates its values in this case, with a mean difference of 1.211±0.945 for FI and 0.953±1.150 for RDI in 2022, and of 1.080 for FI and 1.165 for RDI in 2023 (with σ of 0.922 and 1.029, respectively). This can be observed in Figure 3.27 and Figure 3.28 for 2022 and 2023, respectively: in particular, the red and pink dots are lower than Planet's in the beginning and in the end of the soy growth cycle, whereas they appear higher in the central period of soy growth. The Sentinel curves follow well the ones representing Planet, showing high correlation coefficients of 0.890 in 2022 and 0.967 in 2023 (Figure 3.29).

Table 3.1. Mean and standard deviation of the differences between the values of the indices calculated with Planet and Sentinel bands for 2022.

INDEX		**DIFFERENCE BETWEEN PLANET AND SENTINEL OUTCOMES**			
		2022		**2023**	
		FI	**RDI**	**FI**	**RDI**
NDVI	Mean	0.213	0.221	0.227	0.219
	σ	0.033	0.034	0.028	0.022
GNDVI	Mean	0.211	0.217	0.201	0.202
	σ	0.0267	0.028	0.023	0.017
ENDVI	Mean	0.321	0.324	0.298	0.296
	σ	0.0568	0.056	0.040	0.033
NDRE	Mean	0.147	0.149	0.152	0.154
	σ	0.029	0.031	0.030	0.026

As can be noticed from the regression plots, all the indices calculated with Sentinel underestimate the same values obtained with Planet, with the only exception of LAI. Each regression's slope and intercept are evaluated against the bisector line (which represents a perfect correlation where the two satellite indices are equal for the same date), using a Student t-test (Table 3.2). Across both years, the regression slopes and intercepts generally show significant deviations from the bisector line, indicating that the vegetation indices calculated from Planet and Sentinel satellites are not perfectly correlated. This deviation suggests either a systematic bias or variability between the two datasets.

- In 2022, the NDVI and NDRE values from Planet and Sentinel are not perfectly correlated as their calculated t-values for slopes and intercepts exceed the critical value, indicating a significant difference between their regression lines and the ideal correlation. In contrast, GNDVI and ENDVI show a difference in the slopes of their correlation line compared to the bisector, but the differences in the intercepts are not statistically significant. This suggests that GNDVI and ENDVI values from Planet and Sentinel are biased in slope but not in intercept. The opposite is true for LAI, for which the intercept is significantly different from 0, but the slope shows minimal bias

- In 2023, the t-test results for NDVI show that the slope of the regression line is significantly different from the slope of the ideal correlation, but this is not true for the intercept, which t-value is lower than the critical one. For all the other indices, the regression lines are significantly different from the ideal correlation both in terms of slope and intercept, meaning that the values from Planet and Sentinel are not perfectly correlated due to biases.

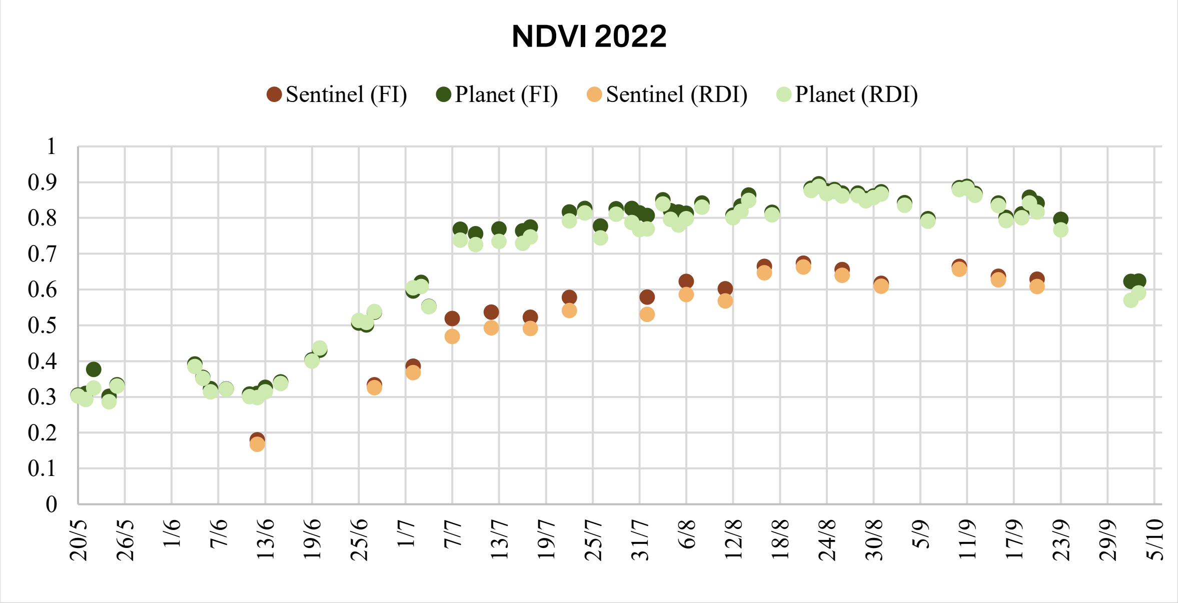

Figure 3.15. NDVI values calculated with Sentinel (red and pink) and Planet (blue and light blue) for 2022.

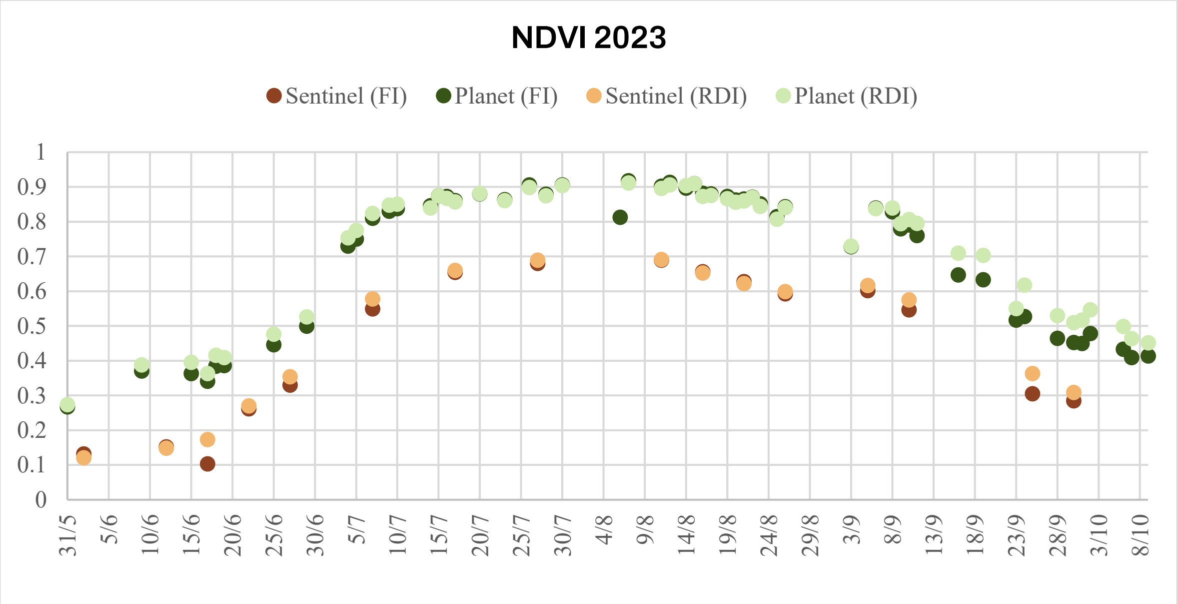

Figure 3.16. NDVI values calculated with Sentinel (red and pink) and Planet (blue and light blue) for 2023.

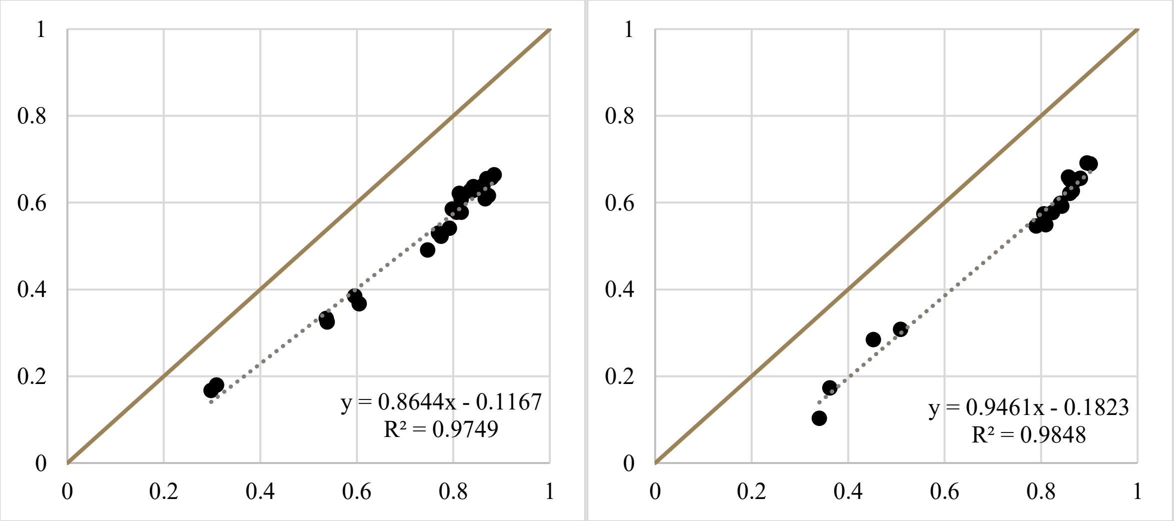

Figure 3.17. Correlation between NDVI values calculated with Planet (x-axis) and Sentinel (y-axis) for 2022 (on the left) and 2023 (on the right). The green line is the bisector and represents the perfect correlation.

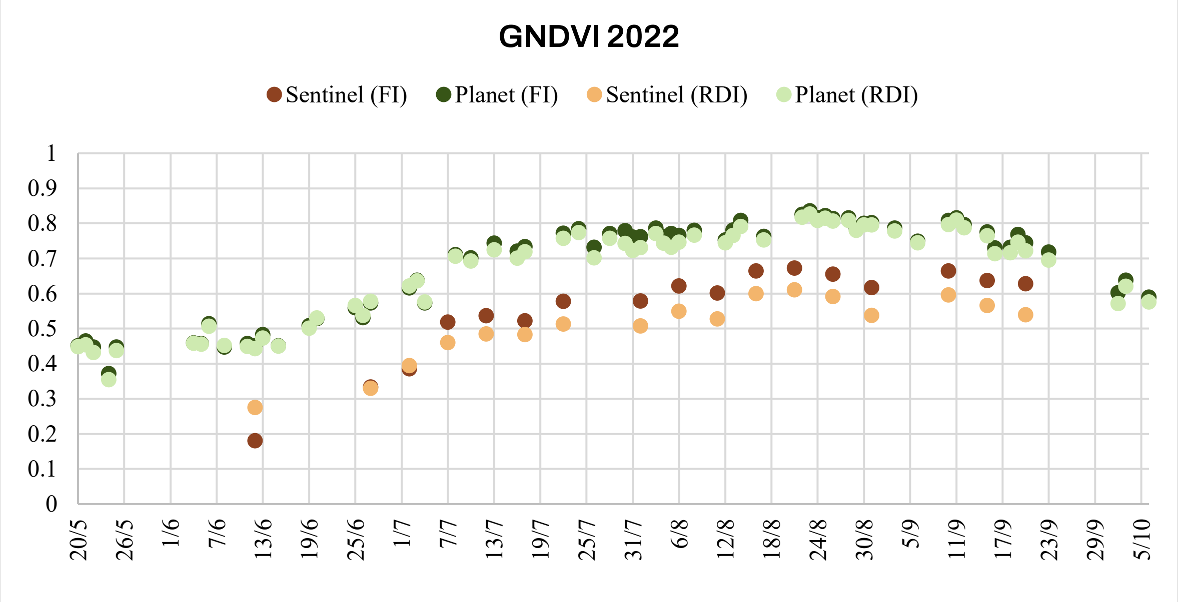

Figure 3.18. GNDVI values calculated with Sentinel (red and pink) and Planet (blue and light blue) for 2022.

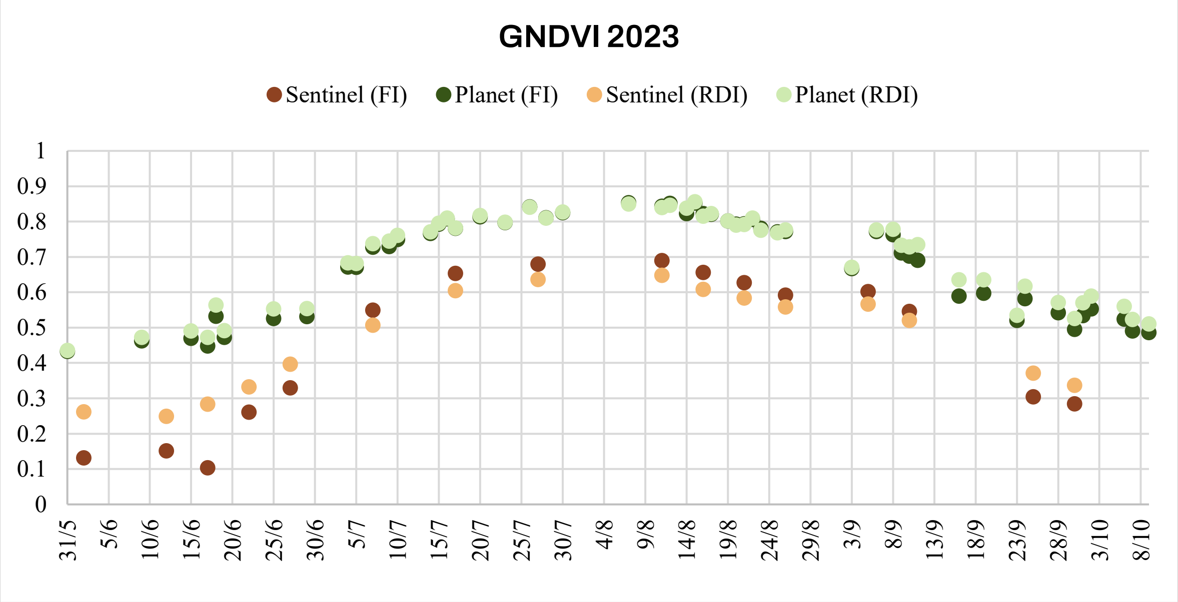

Figure 3.19. GNDVI values calculated with Sentinel (red and pink) and Planet (blue and light blue) for 2023.

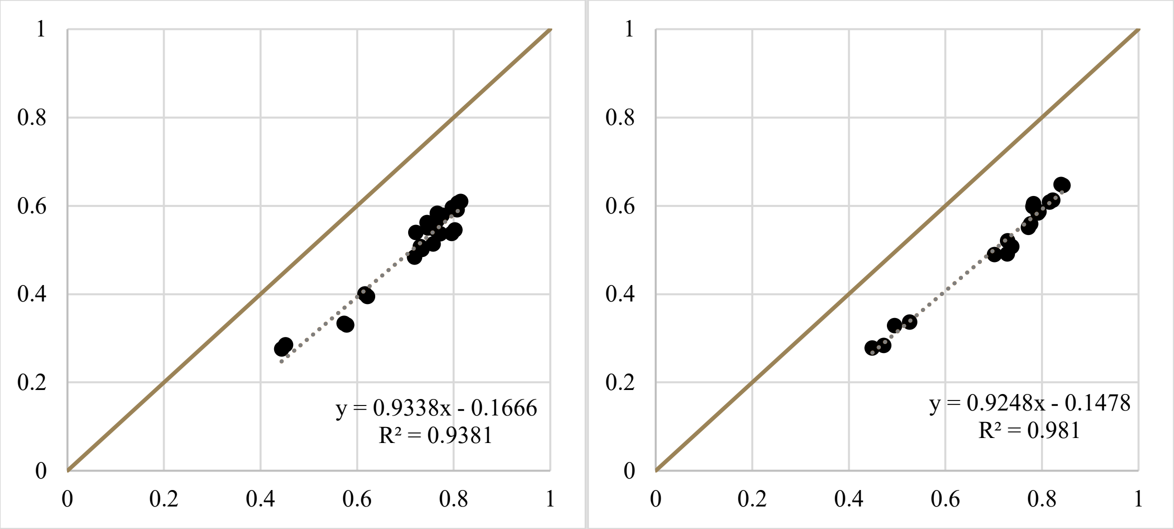

Figure 3.20. Correlation between GNDVI values calculated with Planet (x-axis) and Sentinel (y-axis) for 2022 (on the left) and 2023 (on the right). The green line is the bisector and represents the perfect correlation.

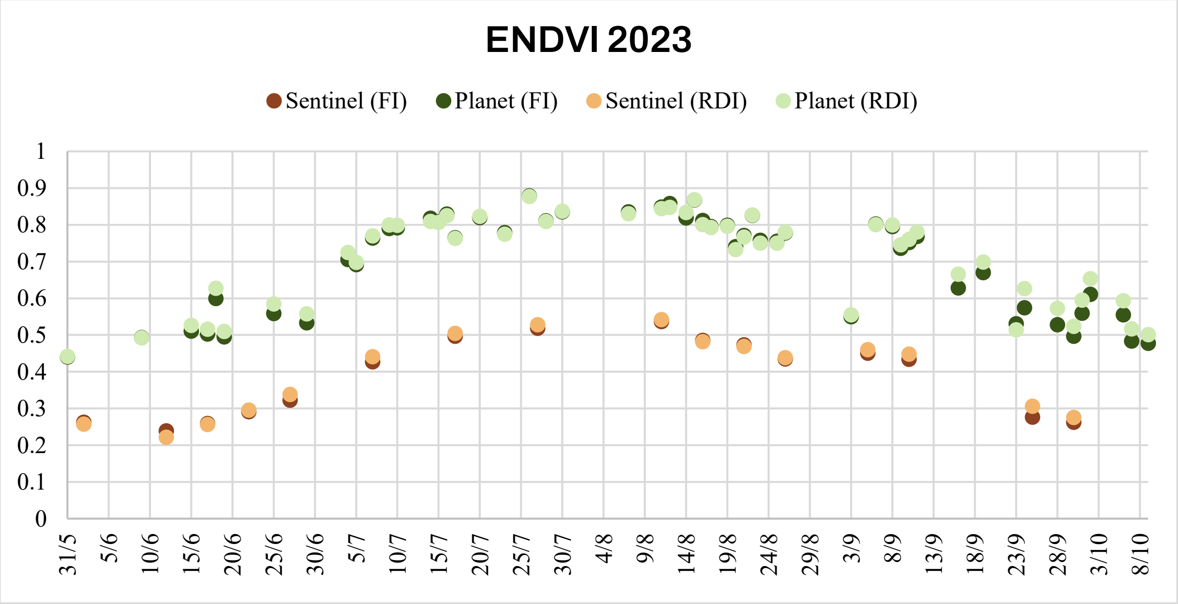

Figure 3.21. ENDVI values calculated with Sentinel (red and pink) and Planet (blue and light blue) for 2022.

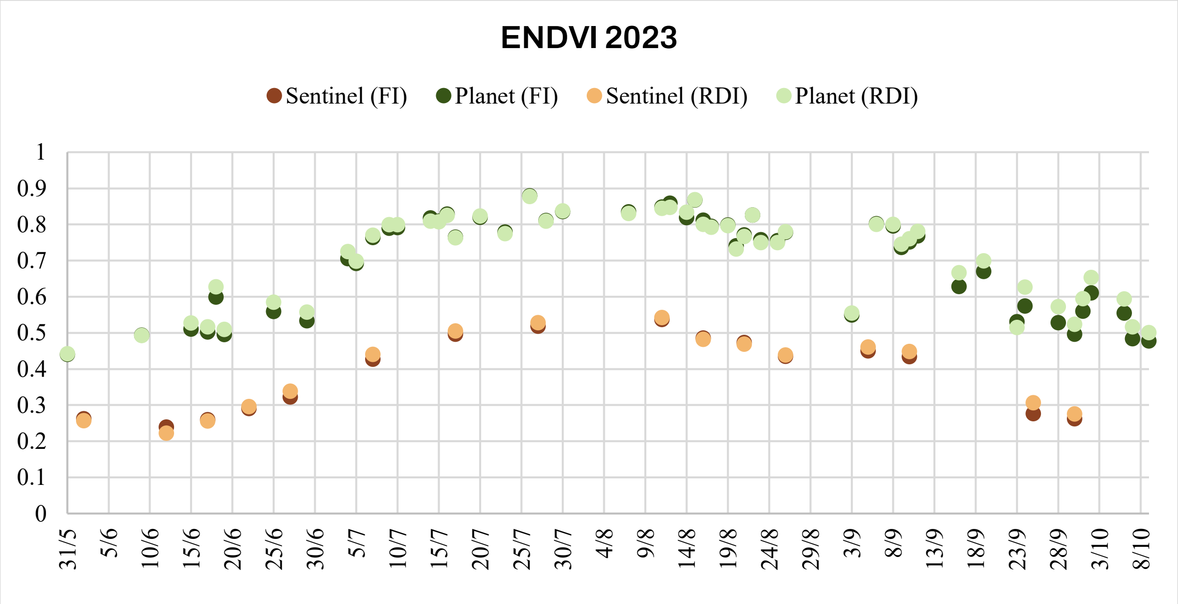

Figure 3.22. ENDVI values calculated with Sentinel (red and pink) and Planet (blue and light blue) for 2023.

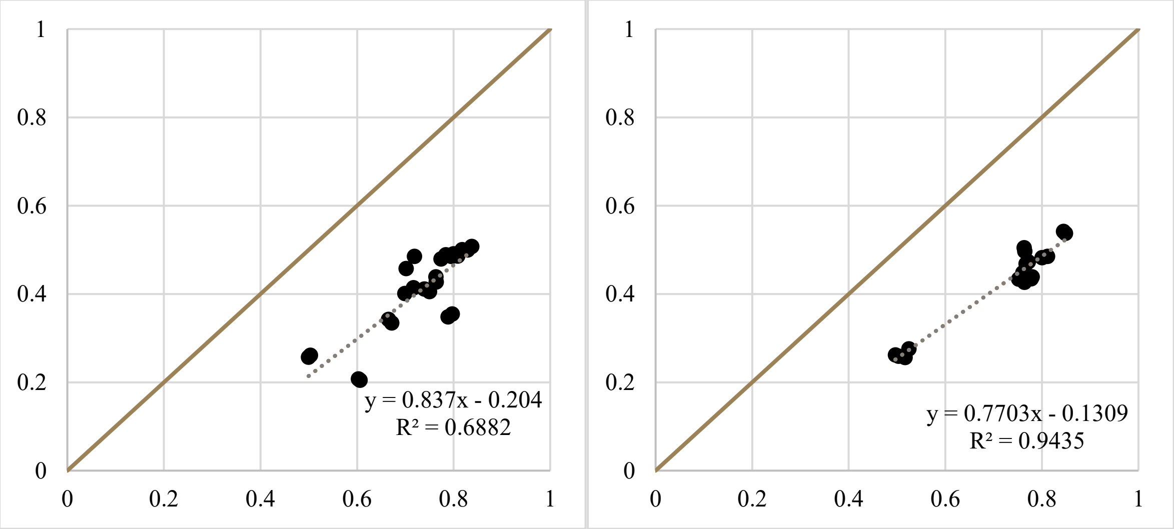

Figure 3.23. Correlation between ENDVI values calculated with Planet (x-axis) and Sentinel (y-axis) for 2022 (on the left) and 2023 (on the right). The green line is the bisector and represents the perfect correlation.

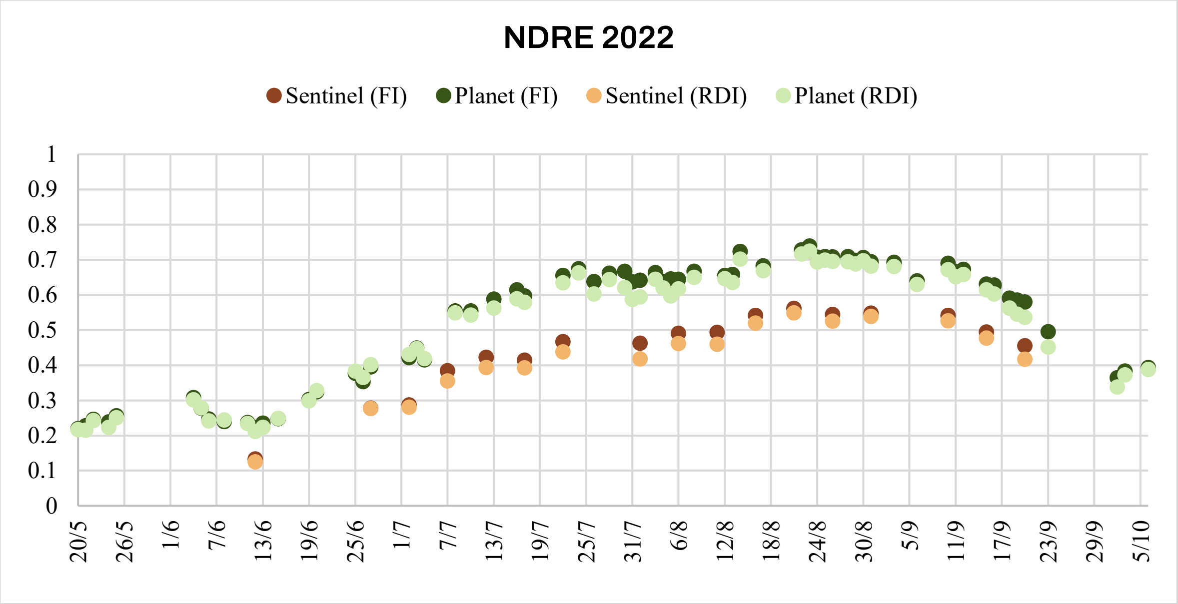

Figure 3.24. NDRE values calculated with Sentinel (red and pink) and Planet (blue and light blue) for 2022.

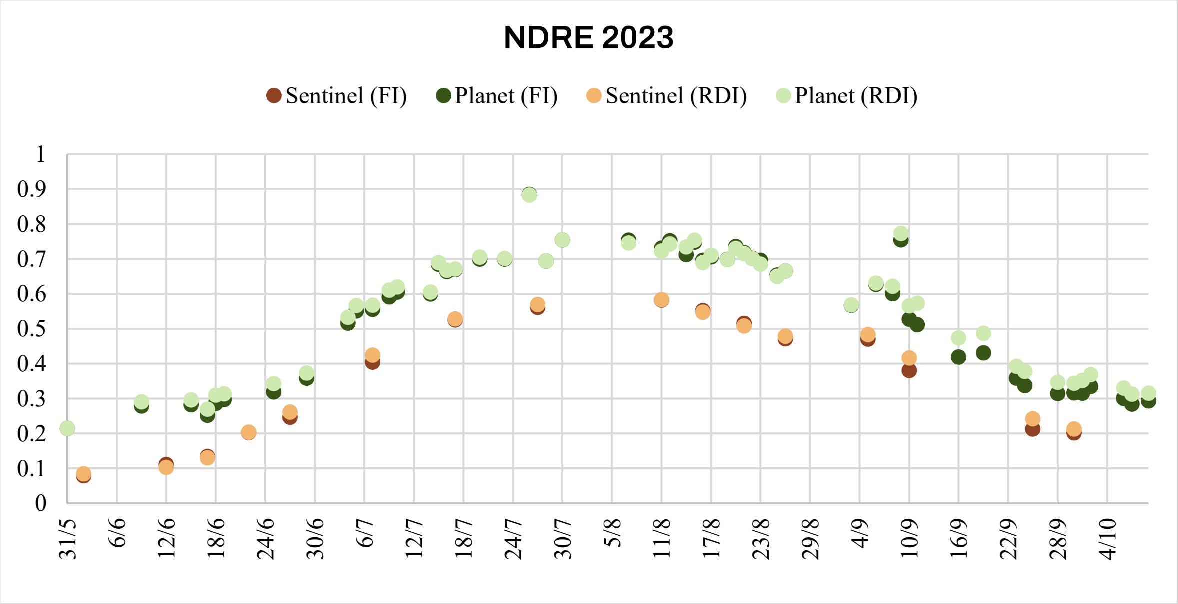

Figure 3.25. NDRE values calculated with Sentinel (red and pink) and Planet (blue and light blue) for 2023.

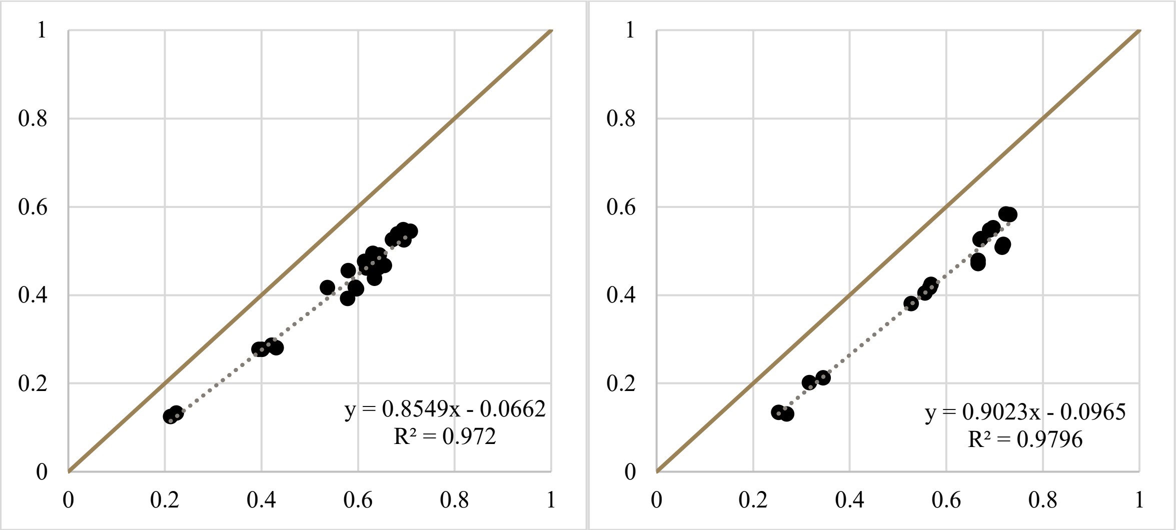

Figure 3.26. Correlation between NDRE values calculated with Planet (x-axis) and Sentinel (y-axis) for 2022 (on the left) and 2023 (on the right). The green line is the bisector and represents the perfect correlation.

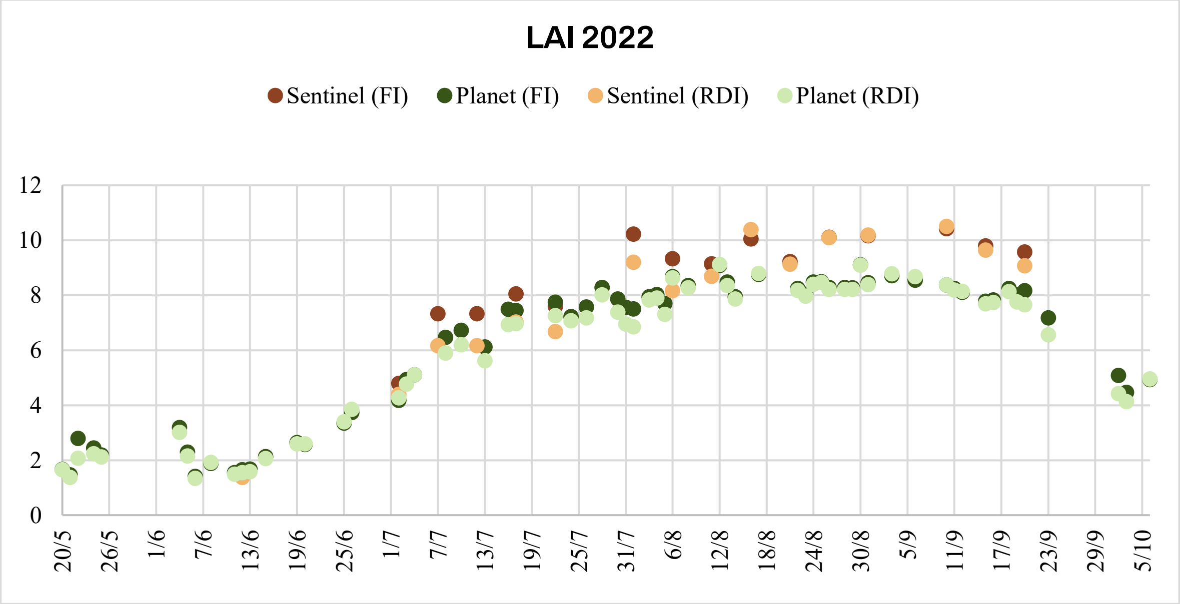

Figure 3.27. LAI values calculated with Sentinel (red and pink) and Planet (blue and light blue) for 2022.

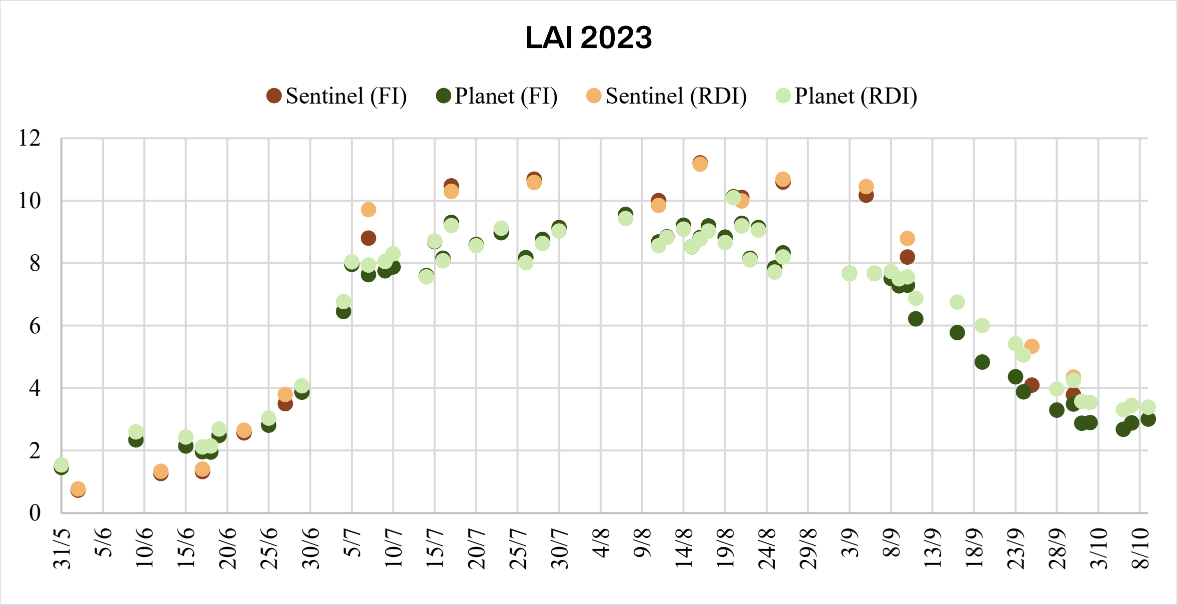

Figure 3.28. LAI values calculated with Sentinel (red and pink) and Planet (blue and light blue) for 2023.

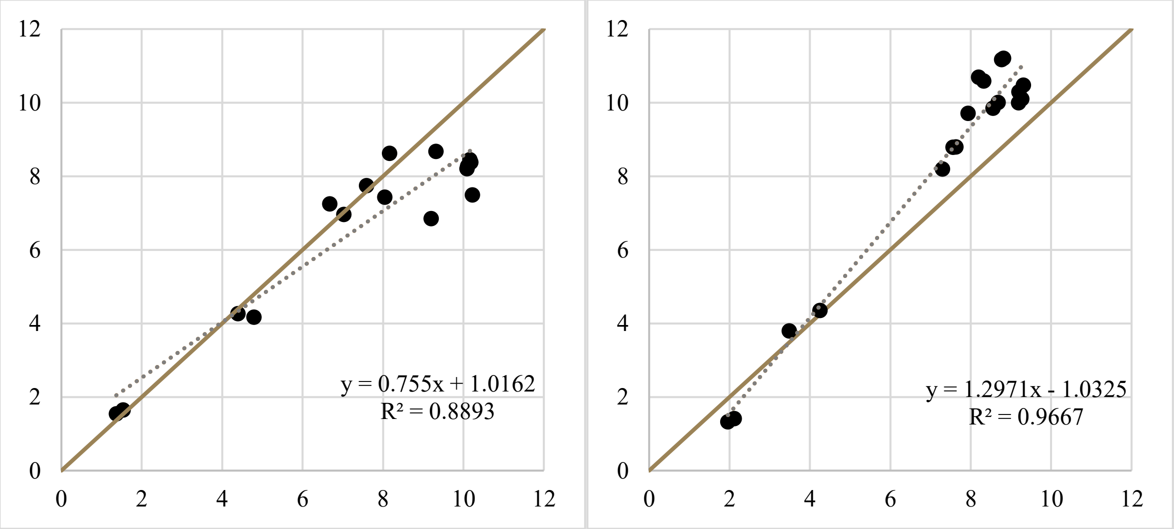

Figure 3.29. Correlation between LAI values calculated with Planet (x-axis) and Sentinel (y-axis) for 2022 (on the left) and 2023 (on the right). The green line is the bisector and represents the perfect correlation.

Table 3.2. Student's t test outcomes. The critical t-value is different in the two years depending on the degrees of freedom, that are a function of the number of days when both acquisitions from Planet and Sentinel were available. "Yes" in the "Significance" column means the difference between the regression coefficients (where m is the slope, q the intercept) and the corresponding coefficient of the bisector is statistically significant; "No" means that the two values can be considered statistically equal.

INDICES		**2022**				**2023**			
		$t_{0.05;22} = 2.0739$				$t_{0.05;16} = 2.1009$			
		Value	**SE**	**|t|**	**Significance**	**Value**	**SE**	**|t|**	**Significance**
NDVI	q	-0.117	0.022	5.208	Yes	-0.182	0.023	7.982	Yes
	m	0.864	0.030	4.590	Yes	0.946	0.029	1.832	No
GNDVI	q	-0.167	0.037	5.208	Yes	-0.148	0.023	6.323	Yes
	m	0.934	0.051	1.294	No	0.925	0.032	2.337	Yes
ENDVI	q	-0.204	0.088	2.319	Yes	-0.131	0.035	3.792	Yes
	m	0.837	0.120	1.357	No	0.770	0.047	4.873	Yes
NDRE	q	-0.066	0.018	3.685	Yes	-0.096	0.019	4.966	Yes
	m	0.855	0.031	4.692	Yes	0.902	0.033	3.002	Yes
LAI	q	-0.516	0.706	0.732	No	-1.032	0.460	2.242	Yes
	m	1.228	0.097	2.362	Yes	1.297	0.060	4.933	Yes

3.3. LI-600 measurements

3.3.1. 2022

In-situ measurements offer valuable insights into plant health. The trend in mean stomatal conductance throughout the soybean growth cycle in 2022 (Figure 3.30) clearly indicates stress conditions of the crop, beginning on June 24th (BBCH 37), as it starts to decline in both the RDI and FI subplots. This downward trend continues until August 12th (corresponding to the midst development of fruit and seeds stage BBCH 73). During these stages, rainfall was exceptionally scarce, with only 54 mm of precipitation spread over 12 days. Additionally, temperatures were unusually high, with peaks of 34.3-34.9°C in June and an heatwave reaching 38.1-38.5°C in July and August. This extremely dry period resulted in very low stomatal conductance, as plants reduce stomatal opening to minimize water loss through transpiration. This diminishes the soybean's ability to produce energy for photosynthesis and, consequently, growth. The very low gsw values of August 12th may be attributed to the timing of the in-situ measurements, which were taken at 8 a.m., when the plants were not yet experiencing the peak daily stress conditions. The downward trend is inverted only when temperatures start decreasing in the second week of August, reaching maximums of 29.2-33°C. Then, gsw rapidly increases up to the maximum mean values of 0.76 and 0.48 on September 3rd for FI and RDI subplots, respectively.

Although both FI and RDI irrigation strategies fail to significantly increase stomatal conductance during the drought period, the FI curve consistently remains higher than that of the RDI throughout the entire growth cycle. This suggests that, despite the overall stress conditions, plants under FI irrigation exhibit a stronger response and better resilience to drought compared to those under RDI, indicating that FI provides relatively more favorable conditions for maintaining plant health.

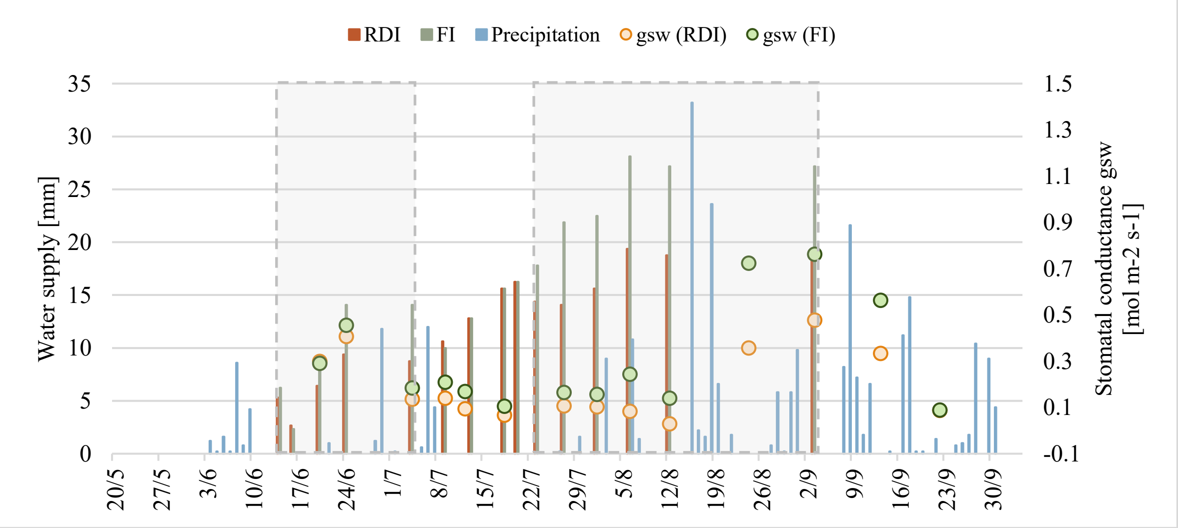

Figure 3.30. Mean stomatal conductance gsw for RDI and FI irrigation strategies measured with LI-600 in 2022. The grey dashed areas represent the periods of application of RDI.

A similar trend is observed in the mean apparent transpiration (T_a) (Figure 3.31), which shows notable peaks of 9.5 mol/m²s for FI and 7.4 mol/m²s for RDI on June 24th. From this day, T_a drops reaching values of 3.0 and 2.2 mol/m²s for FI and RDI, respectively, on July 8th. A slight increasing trend can then be observed in both subplots, indicating that the two irrigation strategies are contributing to improving the health condition of plants, although it does not reach optimal values. A significant decrease follows, leading T_a to 1.5 mol/m²s and 0.3 mol/m²s for FI and RDI, respectively, by August 12th. The extremely low values can be explained by the timing of acquisition of the measurement, but the general decrease could be linked to water scarcity, as the last water supply occurred on August 6th. Like gsw curves, an exponential increase leads transpiration to two peaks in mid-August and in mid-September, when two irrigations of 18.75 and 27.19 for RDI and FI were applied, respectively. Notably, the transpiration under FI nearly doubles that of RDI during these peaks, with FI reaching 10.3 mol/m²s compared to 5.3 mol/m²s under RDI. Then, a significant decline leads transpiration to similar values for the two irrigation strategies on September 23rd, really close to the harvest date. Throughout the soybean growth cycle, both transpiration curves fluctuate in line with changes in water supply, but FI generally follows a more elevated trend than RDI, suggesting that plants under this strategy have greater access to water and, therefore, higher transpiration rate.

Although the difference between the two irrigation strategies is remarkable in the gsw and T_a measurements, this is not captured in the mean leaf temperature values (Figure 3.32). The temperature trend remains stable at 31-33°C during the initial period up to the end of July, with the exception of July 9th, when measurements were taken at 9:30 a.m. After August 12th, when precipitation increases and ambient temperature cools, leaf temperatures of both subplots decrease in magnitude, fluctuating between 25°C during the lower periods and 30°C during the higher periods. Throughout the initial period, FI plants exhibit higher leaf temperatures compared to RDI plants. However, after July 9th, leaf temperatures in FI plants drop below those in RDI plants and remain lower until harvest. This shift aligns with the transpiration patterns shown in Figure 3.31, as increased transpiration cools the foliage, resulting in lower leaf temperatures. Consequently, higher leaf temperatures indicate more severe stress, which can negatively impact the plant's ability to perform photosynthesis efficiently. The leaf temperature patterns observed in June are somewhat unexpected, as RDI plants, being subjected to reduced water supply, would be anticipated to experience greater stress than FI plants. Nevertheless, the temperature difference between the two treatments during the whole period is minimal, ranging between 0.3°C and 1.4°C.

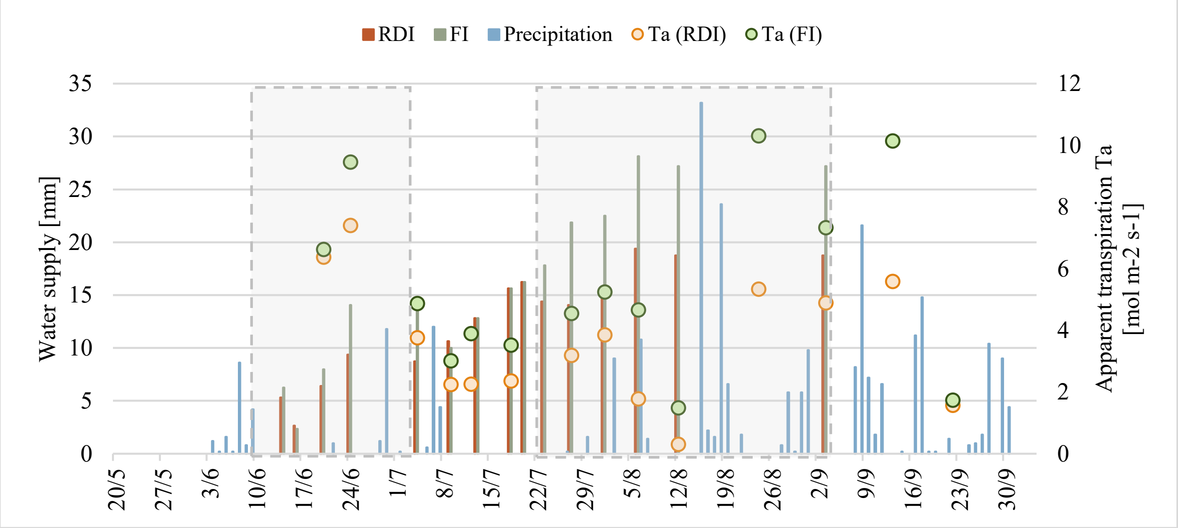

Figure 3.31. Mean apparent transpiration T_a for RDI and FI irrigation strategies measured with LI-600 in 2022. The grey areas represent the periods of application of RDI.

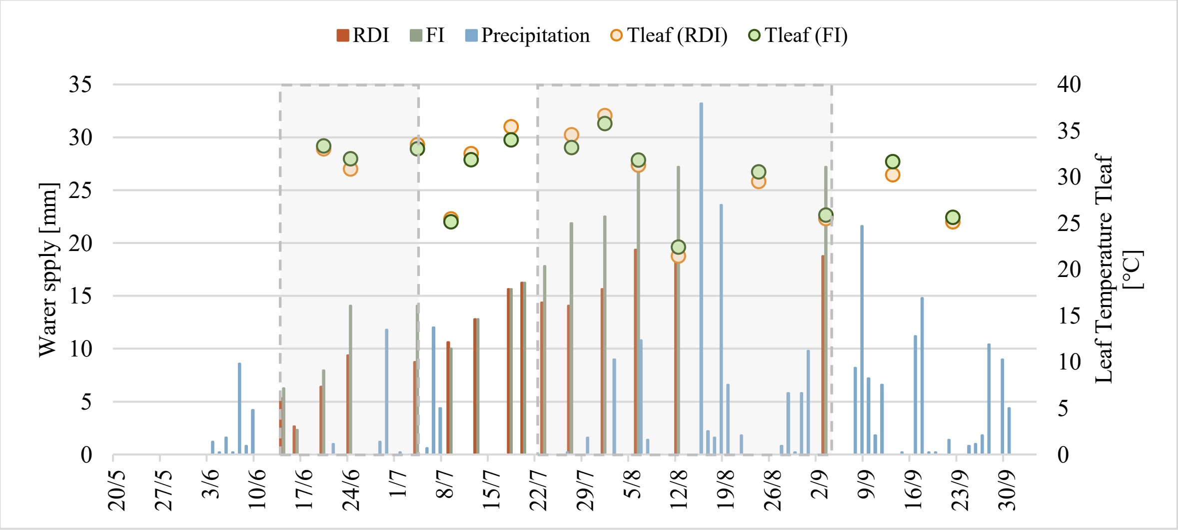

Figure 3.32. Mean leaf temperature Tleaf for RDI and FI irrigation strategies measured with LI-600 in 2022. The grey areas represent the periods of application of RDI.

3.3.2. 2023

Mean stomatal conductance (Figure 3.33) exhibits a steady increase until July 20th, coinciding with a period of abundant precipitation, including a significant event on July 5th and 6th that brought 58.8 mm of rain. Moreover, temperatures were moderate, never exceeding the maximum temperature of 34°C until July 17th, when T_{max} briefly spike to 35.5-35.7 over four days. The data suggests that stomatal conductance is sensitive to rising temperatures, beginning to decline on these hotter days. Once temperature cooled again, gsw increases till August 9th. Following this date, temperatures rose from 27.3°C on that day to a heatwave between August 21st to August 26th, reaching peaks of 36-37°C. In response, gsw fell to 0.63 mol/m²s and 0.57 mol/m²s for FI and RDI conditions, respectively. September also featured temperature anomalies around 31°C, leading to further declines in stomatal conductance, ultimately dropping to 0.07 mol/m²s for FI and 0.10 mol/m²s for RDI. Regarding the comparison between FI and RDI conditions, mean gsw is generally higher in the RDI subplot for most months. However, during most of August, plants under RDI exhibit lower gsw than those under FI. Nonetheless, the difference between the two conditions is minimal, ranging from 0.01 to 0.1 mol/m²s.

Mean transpiration (Figure 3.34) displays a highly oscillating trend, indicating greater variability than stomatal conductance. Specifically, T_a remains relatively constant until early July, after which it begins to fluctuate continuously, likely due to variations in temperature and water supply. Notably, T_a appears to closely follow water supply: following the extreme precipitation event on July 6th, E increases from 9.6 mol/m²s to 11.9 mol/m²s for the FI sublot and from 10.3 mol/m²s to 12.1 mol/m²s for the RDI one. It then declines until the next rainfall event on July 12th, after which it peaks at 14.7 mol/m²s and 13.2 mol/m²s for FI and RDI, respectively, on July 20th. Following this peak, T_a decreases until July 28th: this may be due to frequent precipitation events occurring almost daily from July 19th to July 26th. Excessive water supply can lead to reduced oxygen availability in the root zone due to soil saturation, which in turn may hinder root function and water uptake. This is supported by the subsequent increase in transpiration over the next few days, when precipitation total amount and frequency decreased while temperatures remained moderate. After this period, T_a

consistently decrease, though less abruptly, up to harvesting, except for the measurement taken on August 9th around 11 a.m., which may underrepresent the mean value during peak stress conditions. Unlike stomatal conductance, transpiration in the FI subplot is consistently higher than in plants under RDI.

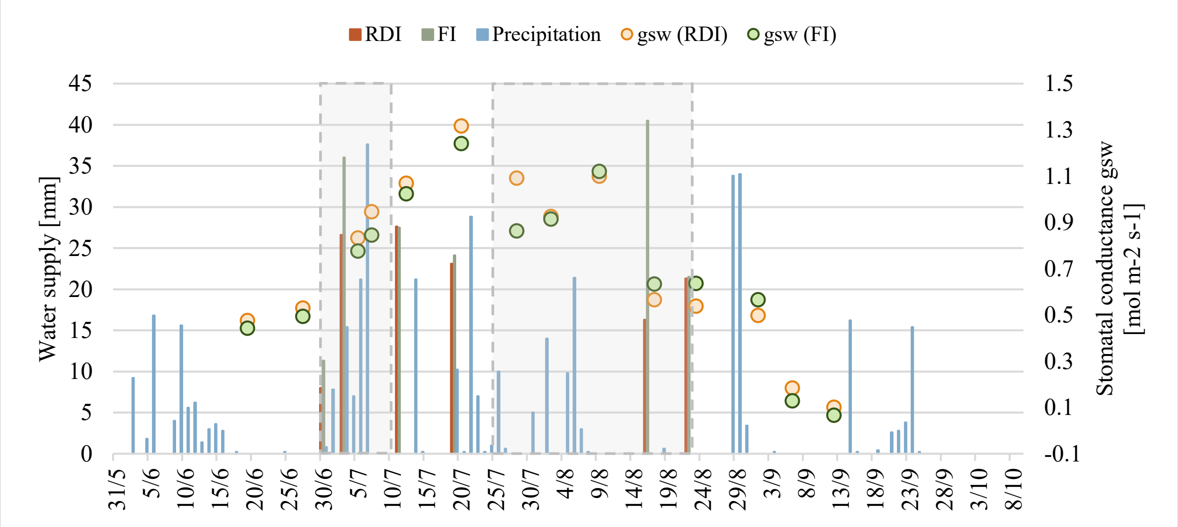

Figure 3.33. Mean stomatal conductance gsw for RDI and FI irrigation strategies measured with LI-600 in 2023. The grey areas represent the periods of application of RDI.

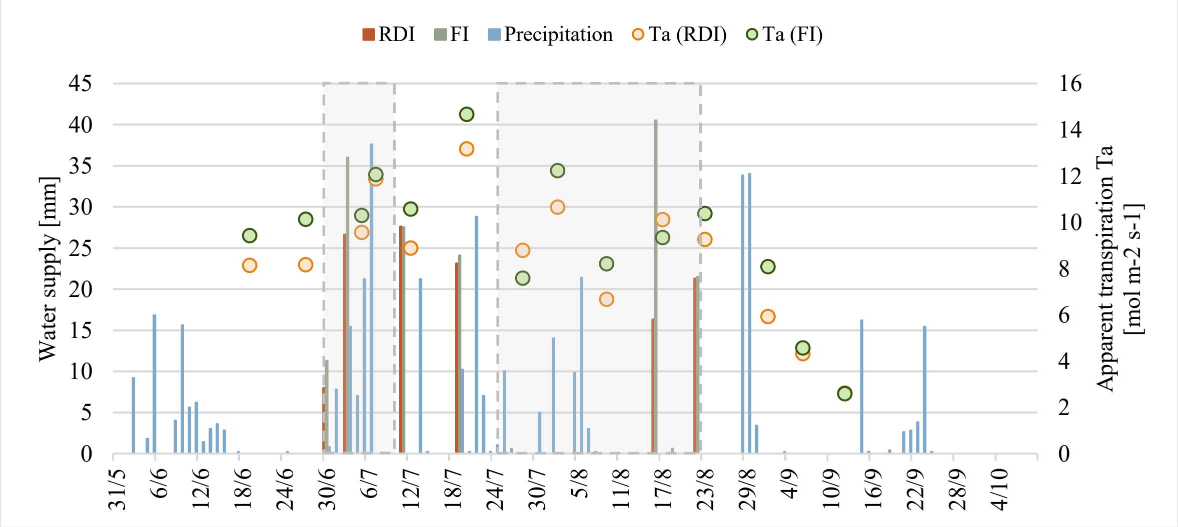

Figure 3.34. Mean apparent transpiration T_a for RDI and FI irrigation strategies measured with LI-600 in 2023. The grey areas represent the periods of application of RDI.

This outcome aligns with expectations for the two irrigation strategies, as transpiration tends to be greater in areas where the plants' water needs are fully met, compared to those experiencing a deficit in water supply. However, this result contrasts with the trends observed in stomatal conductance and satellite indices, where the RDI curve is generally higher than that of the FI subplot.

Finally, mean leaf temperature shows two curves that follow a very similar pattern (Figure 3.35). T_{leaf} oscillations align with the fluctuations experienced by transpiration curves, staying within the range of 30-33°C for both RDI and FI subplots until July 20th. After this date, the oscillations become more pronounced in the FI subplot, with temperature continuously changing between 27°C and 32°C, resulting in a difference of about 5°C between each measurement. In contrast, plants under RDI experience more stable changes, with oscillations around 3°C. By late August, the RDI curve rises from 26°C on August 9th to 35°C by August 17th, while the FI subplot shows a slower increase, from 27°C to 33°C. Eventually, it peaks at 35-36°C for FI and 30-32°C for RDI, leading to higher T_{leaf} in the FI subplot again. This outcome is consistent with the general observation that RDI plants exhibit better overall health compared to FI plants.

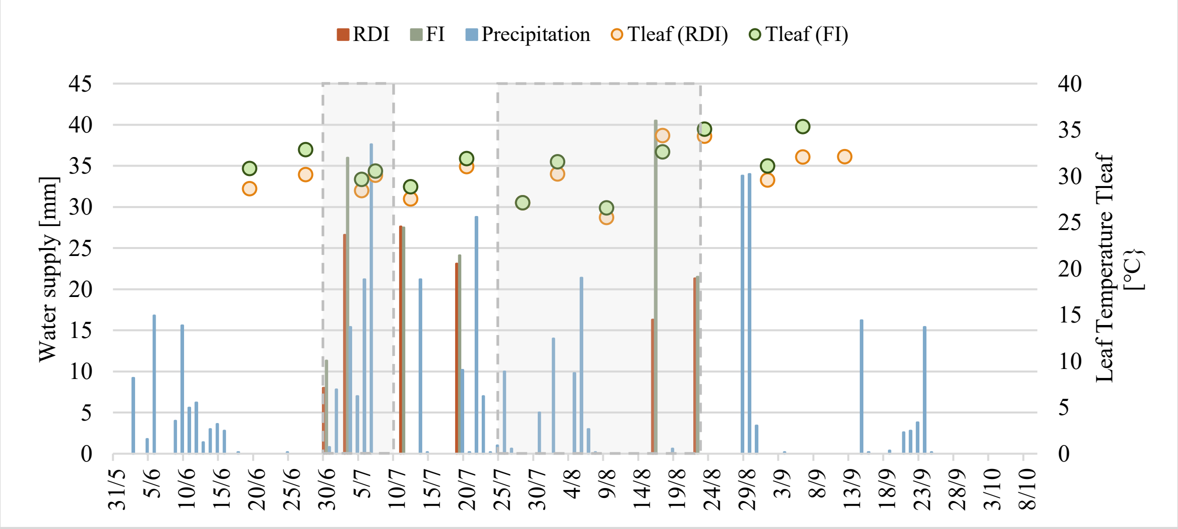

Figure 3.35. Mean leaf temperature Tleaf for RDI and FI irrigation strategies measured with LI-600 in 2023. The grey areas represent the periods of application of RDI.

3.3.3. Comparison between 2022 and 2023

The comparison of in-situ parameters measured in 2022 and 2023 clearly highlights the severe dry conditions of 2022. This is evident from the significantly lower values of stomatal conductance and transpiration, as well as the notably high leaf temperatures throughout most of the summer months. In fact, both mean gsw and T_a (Figure 3.36, Figure 3.37) display much lower values in 2022 compared to 2023 until late August and early September, coinciding with the cooling of the temperatures in 2022. The greatest difference between the two years occurs after mid-July, when 2023 experienced moderate temperatures and frequent precipitation events, in stark contrast to 2022, which saw exceptionally high temperatures and minimal rain, after a prolonged dry period of about 20 days with no rain. By September, the trend reverses, with 2022 gsw and T_a surpassing those of 2023. This shift is attributed to the last irrigation in 2022 occurring on September 3rd, followed by more frequent precipitation, while 2023 experienced a period of zero rainfall with temperatures higher than the average of the thirty-year time series. Moreover, irrigation stopped earlier in 2023, with the last irrigation water supplied on August 22nd.

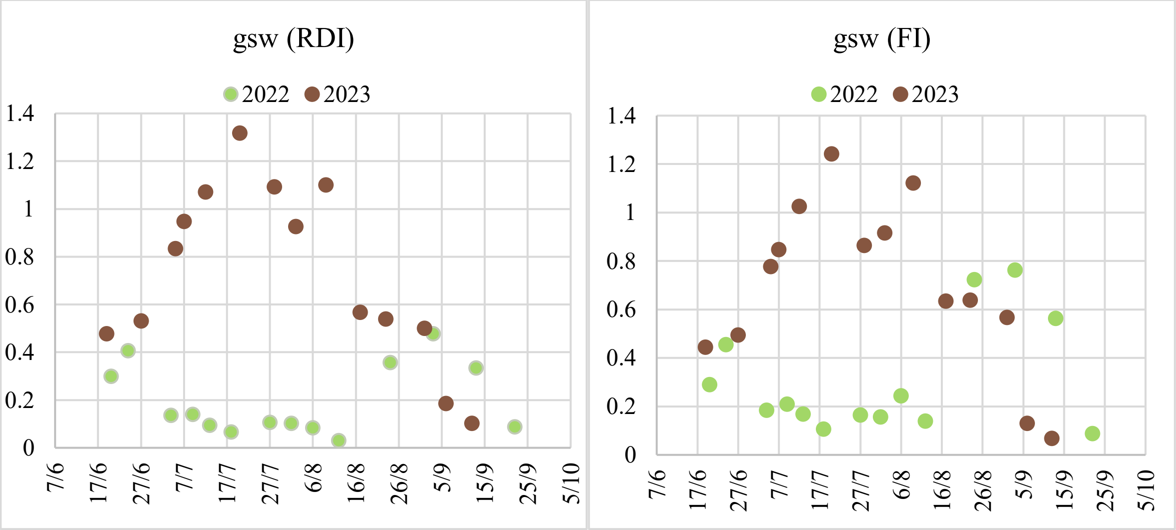

Figure 3.36. Comparison between mean stomatal conductance [mol m-2 s-1] measured in the RDI (on the left) and FI (right) subplots in the two years under consideration.

The same trend can be observed from the mean leaf temperature comparison (Figure 3.38). Leaving aside the measurement taken on July 9, which is underestimated because of the time of acquisition, far from the time of maximum stress for the plant, leaf temperature remains higher in 2022 until early August, indicating more severe stress conditions. The peak difference in this period occurs in late July, consistent with the gsw and E outcomes. Then, as a response to the increasing temperatures of August, T_{leaf} of 2023 becomes higher than those of 2022, that in contrast experienced more frequent precipitation events. The maximum difference occurs in mid-August, with 2023 T_{leaf} resulting higher by 10 and 13°C than 2022 values.

Climatic conditions play a crucial role in determining plant health, as all three curves quickly react to changes in one or more climatic variables. While the influence of weather is clear, the responsiveness of the physiological parameters to the single irrigation events is less evident, with the curves mostly showing responses to temperatures fluctuations. Nonetheless, all three parameters exhibit higher differences between 2022 and 2023 for the RDI subplots than the FI portions of the field. This suggests that, although less apparent, irrigation significantly influences the trends of the plant physiological factors. In fact, RDI's performance is more variable and responsive to any external climate change than FI, which, on the other hand, though responsive, shows variations of smaller magnitude.

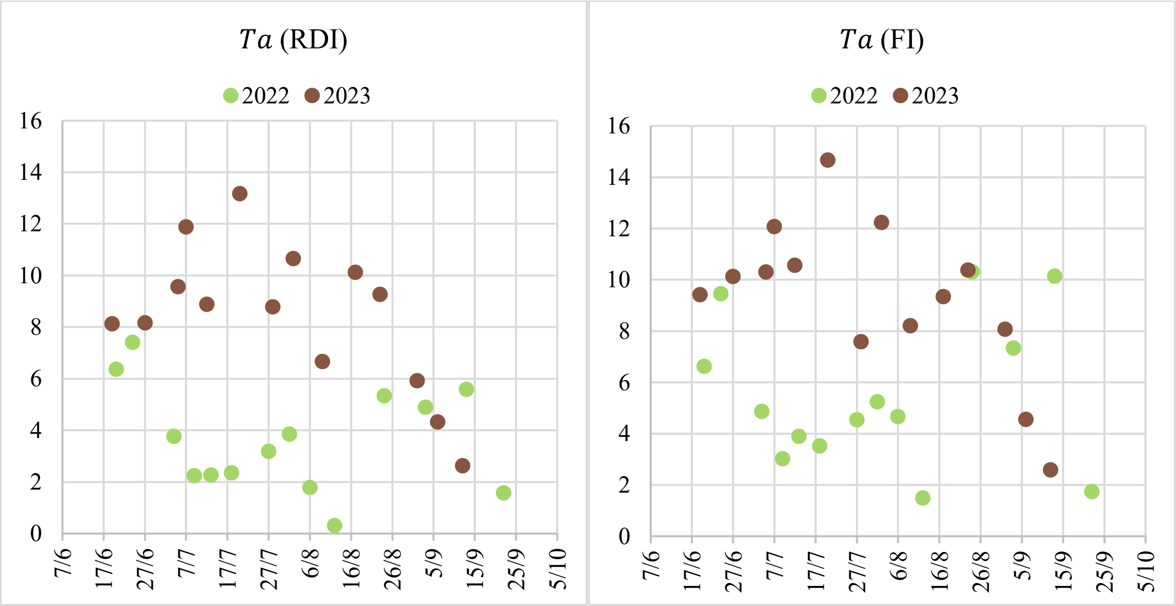

Figure 3.37. Comparison between mean apparent transpiration [mol m-2 s-1] measured in the RDI (on the left) and FI (right) subplots in the two years under consideration.

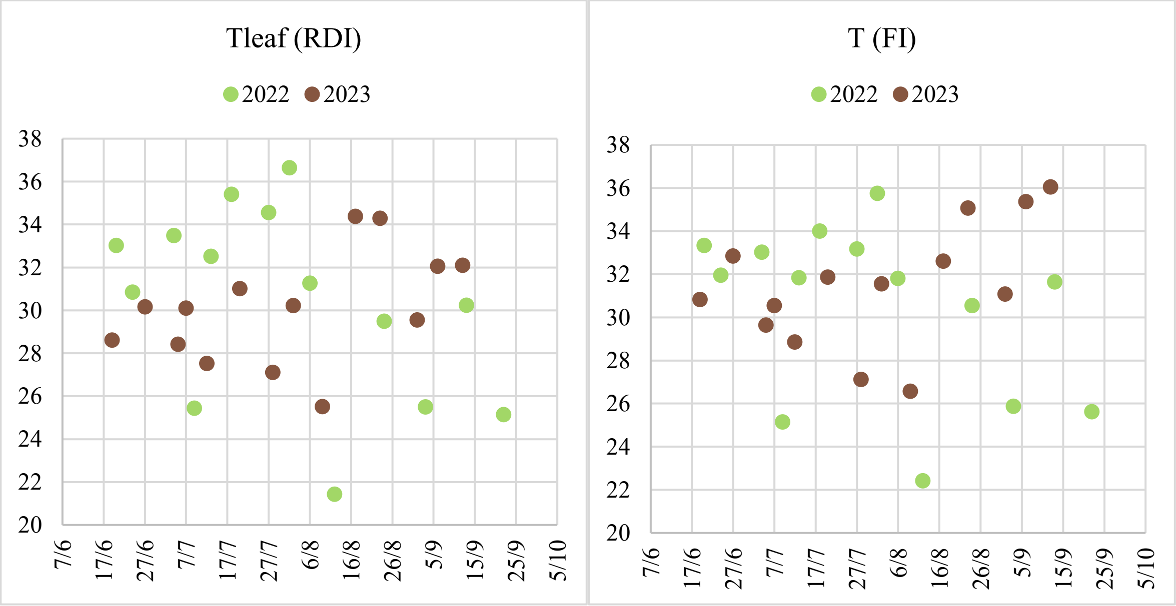

Figure 3.38. Comparison between mean leaf temperature [°C] measured in the RDI (on the left) and FI (right) subplots in the two years under consideration.

3.4. Crop yield

Over the two years, 2022 and 2023, key agronomic parameters such as seed yield, biomass production, water use efficiency (WUE), oil content, and protein content were measured (Table 3.3, Table 3.4), offering a comprehensive view of how soybeans respond to different irrigation regimes.

In 2022, FI produced a higher yield compared to RDI. This suggests that full irrigation promotes better overall yield due to optimal water availability. However, when considering WUE for production, the depth of water required to produce that specific amount of dry matter, RDI outperformed FI with a WUE of 7.4 kg/ha/mm compared to 6.9 kg/ha/mm. This suggests that while full irrigation maximizes yield, the water is used more efficiently under RDI conditions. However, regarding biomass production, FI resulted in a higher biomass yield compared to RDI, though the WUE difference between treatments was small (6.3 kg/mm vs. 6.0 kg/mm for FI and RDI, respectively). This highlights that although biomass production under full irrigation was more substantial, the incremental gain from increased water use was relatively modest in terms of efficiency. In terms of quality, RDI resulted in a higher oil content of 21.3% compared to 20.7% under FI. This suggests that some degree of water stress, as imposed by deficit irrigation, might stimulate greater oil accumulation in the seeds. However, the protein content showed the opposite pattern, being higher under FI (43.1%) compared to RDI (41.8%). This indicates that while water stress may enhance oil content, it might have a limiting effect on protein synthesis, possibly due to reduced protein metabolism under drought conditions.

The results from 2023 present a different scenario, reflecting the different environmental conditions and crop response in that year. The RDI yield was higher than FI, with also higher WUE (5.1 kg/ha/mm compared to 4.5 kg/ha/mm under FI). This further supports the argument that under certain conditions, regulated deficit irrigation can optimize water use without significantly compromising yield. Biomass production was nearly identical under both treatments. However, the WUE for biomass was higher under RDI (8.2 kg/mm) compared to FI (7.7 kg/mm), indicating that the plants used water more efficiently to produce biomass under reduced irrigation levels in 2023. Regarding quality parameters in 2023, the

Table 3.3. Results in terms of yield and biomass in 2022 and 2023, both in terms of dry matter and in terms of Water Use Efficiency (WUE).

YEAR	IRRIGATION	YIELD [kg/ha]	YIELD WUE [kg/ha/mm]	BIOMASS [kg/ha]	BIOMASS WUE [kg/mm]
2022	RDI	3289.4	7.4	2637.8	6.0
	FI	3447.2	6.9	3154.4	6.3
2023	RDI	2691.1	5.1	4334.0	8.2
	FI	2528.8	4.5	4347.5	7.7

Table 3.4. Results in terms of quality parameters (protein and oil content in percentage) for the crop under RDI and FI in 2022 and 2023.

	2022		2023	
	RDI	FI	RDI	FI
Oil content (%)	21.3	20.7	20.4	20.3
Protein content (%)	41.8	43.1	43.9	43.6

oil content was marginally higher under RDI (20.4%) compared to FI (20.3%), though the difference was minimal. However, as in 2022, the protein content remained slightly higher under FI (43.6%) than under RDI (43.9%), reinforcing the earlier observation that full irrigation tends to promote higher protein levels in soybeans.

Although these differences in yield, biomass, water use efficiency, oil content, and protein content were observed between the two irrigation treatments across both years, statistical analysis revealed that they are not statistically significant. This suggests that the variations between full irrigation and regulated deficit irrigation did not reach a level of significance to confirm a definitive advantage of one treatment over the other.

.

4. DISCUSSION

4.1. Satellite imagery for monitoring plant water status

By comparing how different VIs correspond to field-level measurements such as stomatal conductance, transpiration, and leaf temperature, we can assess the reliability and effectiveness of Planet satellite in offering actionable insights for irrigation management. Based on the results from both seasons, it is clear that Planet data provide valuable information on plant growth, biomass accumulation, and stress conditions. The indices were able to capture key growth trends across different irrigation treatments, reflecting differences in canopy cover, photosynthetic activity, and chlorophyll content throughout the different soybean growth stages and between FI and RDI. Additionally, VIs reflected adequately the response of plants to irrigation and precipitation inputs, as well as temperature variations and particularly dry conditions.

In 2022, VIs showed lower values compared to 2023, highlighting the markedly different climatic conditions. The prolonged drought in 2022, with very low precipitation and particularly high temperatures, hindered the VIs growth, particularly in terms of chlorophyll content. photosynthetic activity, and canopy structure. Growth was largely sustained by irrigation, although less defined and sharp compared to the more moderate climate of 2023. When rainfall eventually occurred after the extended dry spell, VIs exhibited a rapid increase, demonstrating the ability of satellite imagery to capture significant shift in the PWS. In contrast, VIs in 2023 started at already higher values and eventually reached greater peaks, reflecting the milder temperatures and more frequent rainfall throughout the season.

The sensitivity of Planet indices to water supply is evident when examining the period from July 26th to August 9th, 2022 (Figure 4.1, Figure 4.2). During this time, the indices clearly respond to irrigation events. While their absolute values differed due to their varying sensitivity to specific plant characteristics, the overall trend was consistent across all indices. Irrigation events significantly boosted their values, whereas precipitation had a smaller impact due to the limited depth in this period. After 2-4 days without substantial water supply, the VIs gradually decline but rebounded quickly following the next irrigation or precipitation event. In contrast, physiological data (Figure 4.3) did not exhibit the same pattern, as LI-600 measurements were not taken immediately before and after the irrigation events. Nonetheless, there is a noticeable increase in the difference between values of gsw and T_a in the FI and RDI subplots on August 6th compared to earlier days. Although the absolute values were not captured at the peak stress time of the day, and therefore cannot be compared to the absolute values of the acquisitions taken the other days, this variation suggests that plants under RDI experienced more stress than those under FI. These daily fluctuations were not well captured by the indices, which were measured by Planet satellite around the same time as the LI-600 data (9-10 a.m.). This suggests that the finer physiological responses to water stress were not always fully captured by the satellite-derived indices alone.

Despite the difficulty in capturing daily variability, the VIs provided continuous and broad-scale insights into plant health, capturing responses to environmental changes, such as water supply and temperature fluctuations, that might otherwise go unnoticed in field-level measurements. For instance, between June 19th (BBCH 30) to June 27th (BBCH 41), 2022, plants were in the middle of their vegetative growth stage, characterized by stem elongation and leaf development. The physiological parameters measured on June 20th and 24th (Figure 4.4), showed an improvement of plant health, with a rapid increase in gsw and T_a and a corresponding drop in leaf temperature, thanks to the enhanced cooling effect due to the higher transpiration, despite the extreme temperatures registered in that period, with maximum temperatures of 34-35°C for most days. However, VIs (Figure 4.5, Figure 4.6) showed a brief but sharp decline on June 26th, likely because of the high temperature, that on that day reached the maximum of 35°C. This decline is particularly well captured by GNDVI, ENDVI, and NDRE, as they measure the photosynthetic activity, chlorophyll content, canopy structure, and general stress status of vegetation. NDVI, which mostly concentrates on biomass development, did not show the same sharp decrease, as well as LAI, indicating that, despite the stress conditions, plants were still physically growing. The lack of in-situ measurement missed these stress signals, underscoring the utility of satellite data as supplement to direct physiological measurements.

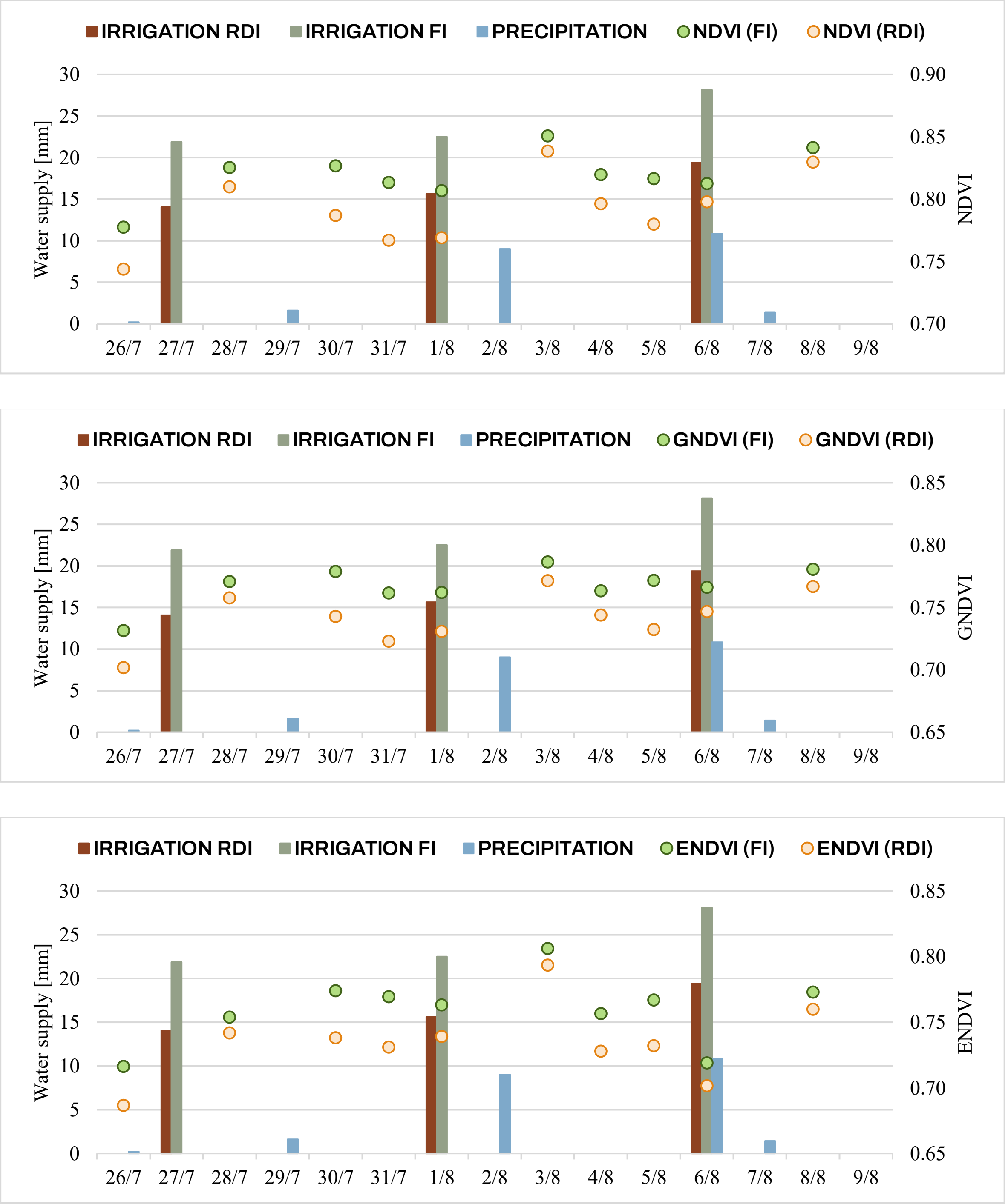

Figure 4.1. Trend of NDVI (up), GNDVI (middle), and ENDVI (down) in the period ranging from July 26th to August 9th, 2022.

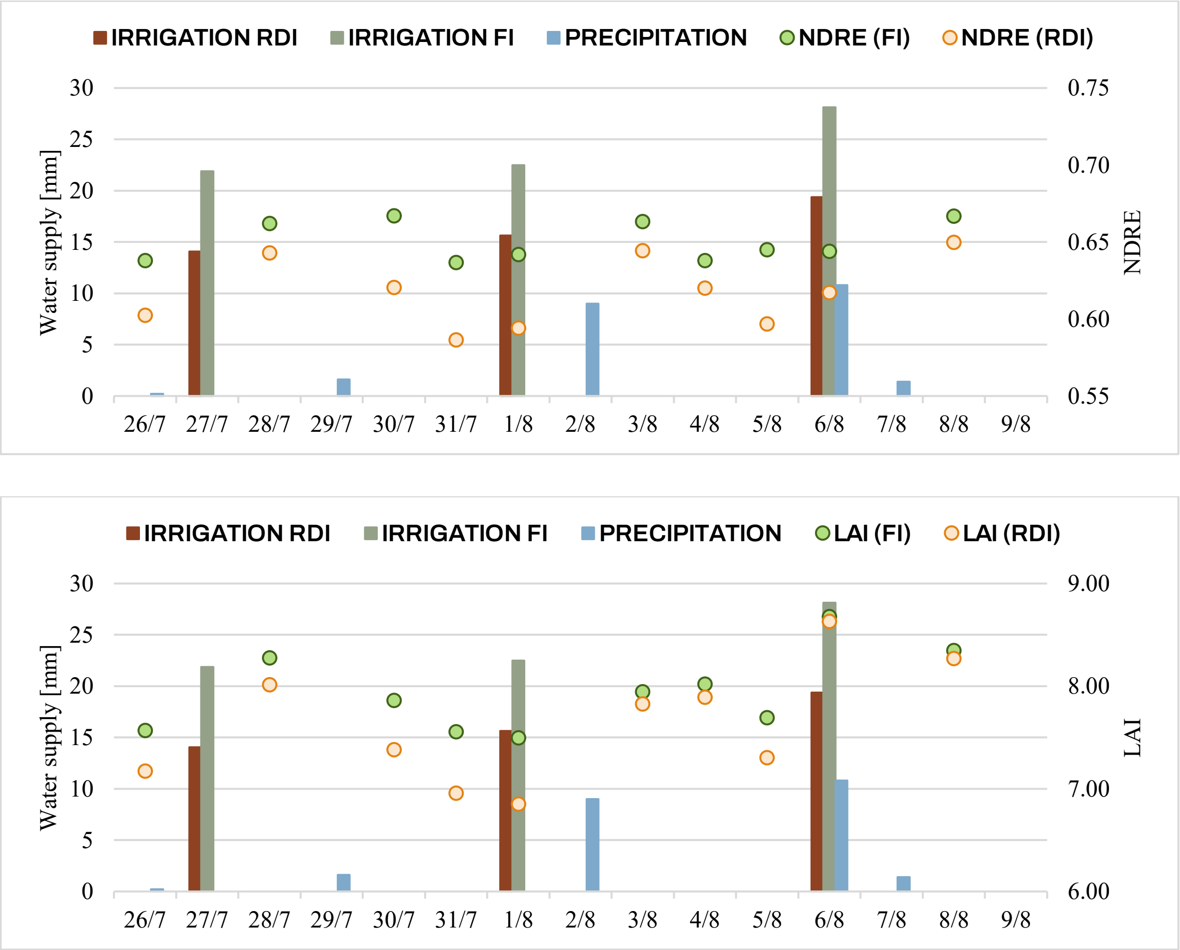

Figure 4.2. Trend of ENDVI (up), NDRE (middle) and LAI (down) in the period ranging from July 26th to August 9th, 2022.

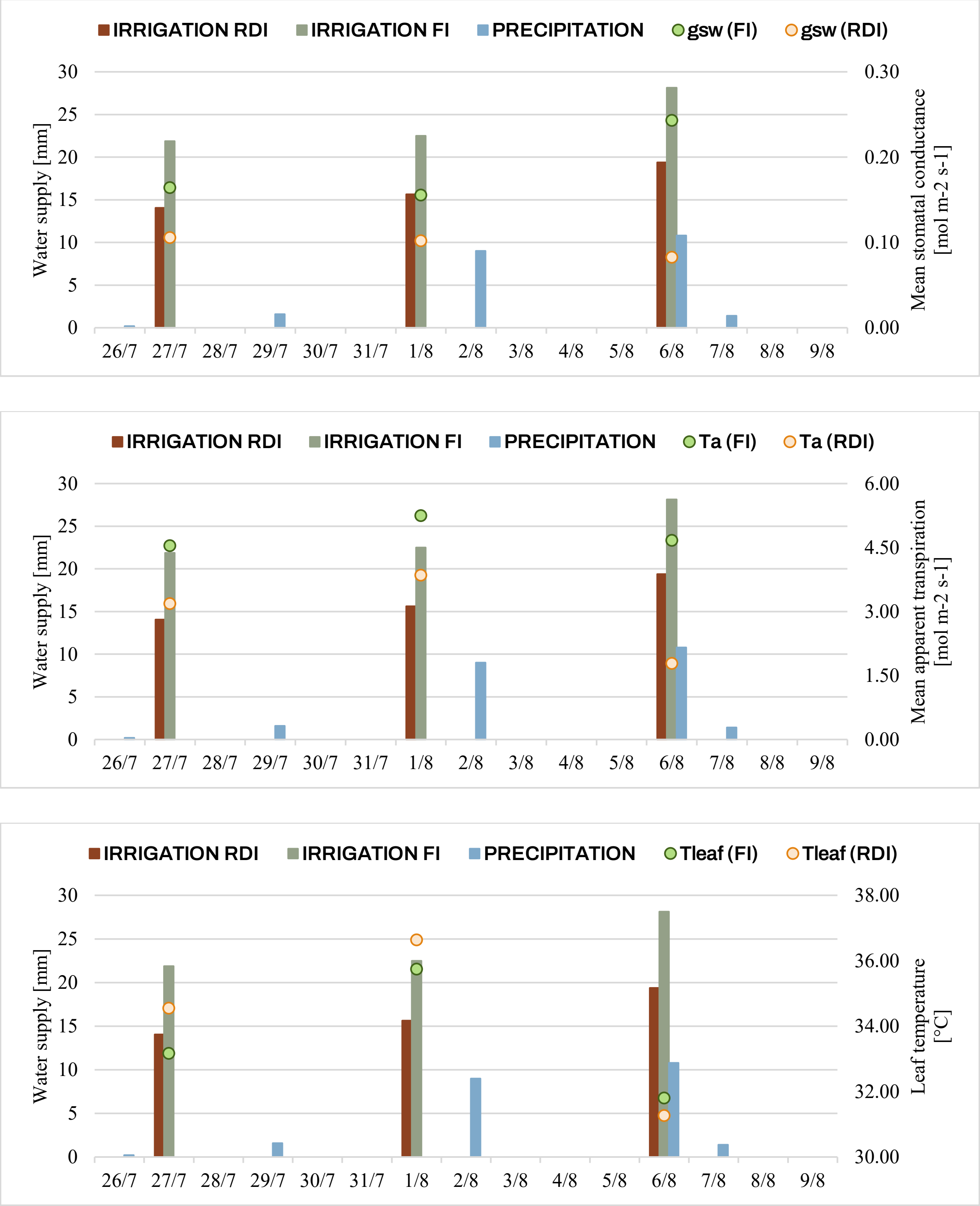

Figure 4.3. Trend of mean stomatal conductance (up), mean apparent transpiration (middle), and mean leaf temperature (down) in the period ranging from July 26th to August 9th, 2022.

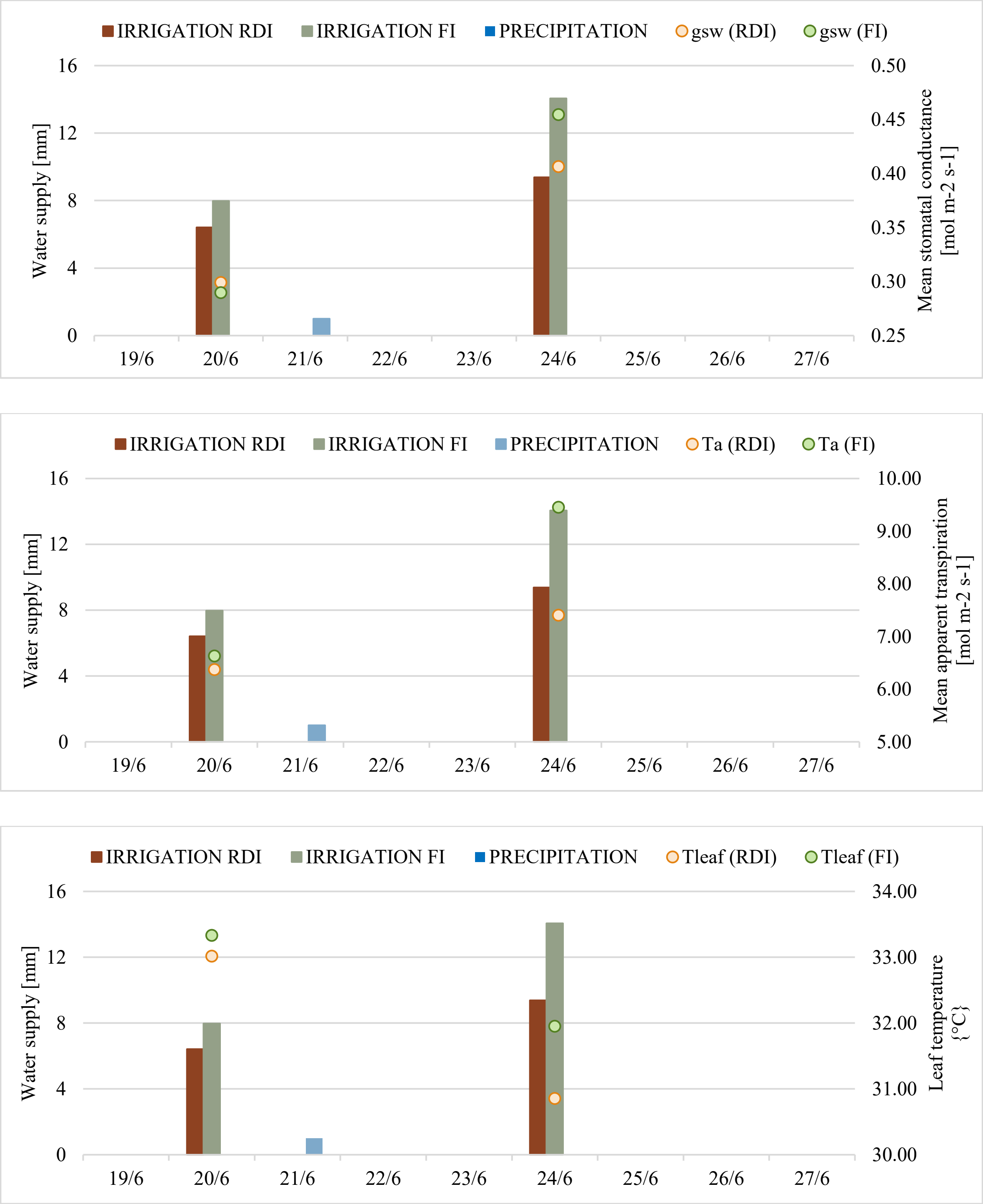

Figure 4.4. Trend of mean stomatal conductance (up), mean apparent transpiration (middle), and mean leaf temperature (down) in the period ranging from June 19th to June 27th, 2022.

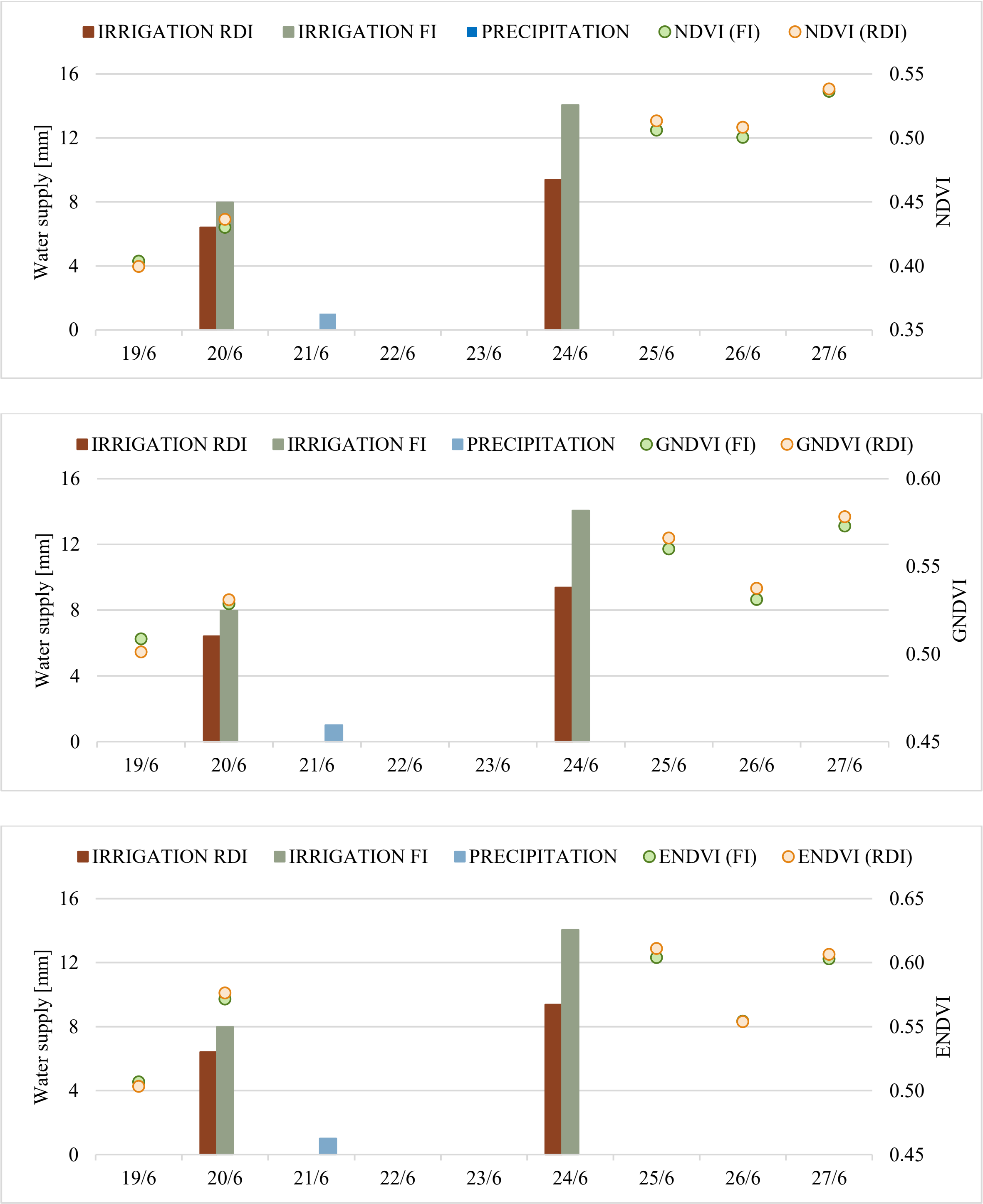

Figure 4.5. Trend of NDVI (up), GNDVI (middle), and ENDVI (down) in the period ranging from June 19th to 27th, 2022.

Figure 4.6. Trend of NDRE (up) and LAI (down) in the period ranging from June 19th to 27th, 2022.

4.2. Comparison of Planet and Sentinel performance

The comparison between Sentinel and Planet satellite data reveals notable differences in their performance across various vegetation indices, primarily driven by their distinct spatial and temporal resolutions, as well as differences in data processing methodologies. Sentinel, with its coarser spatial resolution (10 m) and lower temporal resolution (5-10 days), consistently underestimates values compared to Planet, which offers finer spatial resolution (3 m) and more frequent revisits (daily).

Specifically, NDVI values from Sentinel are underestimated by 0.213 to 0.227 compared to Planet, though the high correlation coefficients (0.984 in 2023 and 0.977 in 2022) indicate that Sentinel accurately tracks the temporal trends observed in Planet data. GNDVI shows similar patterns, with a slightly poorer correlation than NDVI, underscoring Sentinel's ability to capture general vegetative trends despite systematic underestimation. ENDVI, however, exhibits the poorest alignment between the two platforms, particularly in 2022 ($R^2 = 0.6882$), highlighting a challenge for Sentinel in capturing finer spectral details that are more sensitive to minor vegetative changes such as canopy structure, possibly due to its lower spectral resolution. Conversely, NDRE shows the closest agreement between the two datasets, with small underestimations of 0.147 – 0.154, making it one of the most reliable indices in this comparison. Interestingly, Sentinel overestimate LAI values compared to Planet by an average of 1.211 (FI) and 0.953 (RDI) in 2022, and 1.080 (FI) and 1.165 (RDI) in 2023. This is likely due to the nature of the LAI equation, that is experimentally derived from EVI and therefore represents an approximation. Despite this, Sentinel's LAI trends still closely follow Planet's.

The regression analysis further suggests that while Sentinel and Planet track similar patterns, their differences in slope and intercept, particularly for NDVI, NDRE, and ENDVI, reveal biases that could be attributed to Sentinel's coarser spatial and temporal resolution, which may fail to capture the detailed variability in crop canopy detected by Planet's higher resolution sensors. These discrepancies, along with significant deviations from the ideal bisector line as indicated by the Student t-test, reflect the limitations of Sentinel for precision agriculture, where finer temporal and spatial resolutions, such as those provided by Planet, offer a more granular understanding of crop health.

However, Sentinel's freely available data makes it a valuable resource for large-scale monitoring, while Planet's higher cost structure may limit its use to more targeted applications requiring frequent and high-resolution observations. Although the Sentinel data consistently underestimated Planet outcomes, the high correlation coefficients between the two platforms indicate that both provide valuable insights into vegetation dynamics over time. This finding suggests that while differences in absolute values exist, the overall trends remain consistent across both platforms, making them suitable tools for monitoring agricultural health and aiding irrigation management. Therefore, Sentinel resulted still adequate to monitor the general PWS stress, although its absolute values need some calibration in order to be considered as a basis for irrigation decision making. Nonetheless, the reduced frequency of the acquisitions dictated by its temporal resolution could be an obstacle in more delicate crops that need a constant and precise evaluation of the PWS.

4.3. FI and RDI performances

The evaluation of Full Irrigation (FI) and Regulated Deficit Irrigation (RDI) strategies presents nuanced insights into the trade-offs between water savings and crop performance.

The results show that FI generally promotes higher values in key VIs such as NDVI, GNDVI, ENDVI, NDRE, and LAI during 2022, with minimal but notable differences between the two strategies. This trend shifts in 2023, where RDI surpasses FI in most indices despite receiving less water, indicating the potential for higher irrigation efficiency under RDI. This performance can be explained by the crop aptitude to adapt to reduced water availability in RDI plots, mainly related to the higher percentage of fine particles compared to coarse soil. Soil composition plays a crucial role in water retention, and the RDI subplots, with a higher fraction of fine-textured particles such as silt and clay, were able to retain significantly more water than the coarser-textured soils in FI subplots. Fine particles have smaller pore spaces, which slow down water movement through the soil profile, allowing the soil to hold onto water for longer periods. This characteristic creates a natural reservoir effect, where more water remains available to the plants even when the irrigation input is reduced. As a result, the RDI subplots were able to hold up to 43% more water than the FI areas: specifically, PAWC equals 37.44 and 34.26 mm in subplot 10 and 11, respectively, both under FI, while it counts 54.03 and 48.56 mm in subplot 5 and 6, RDI-irrigated. The total irrigation water depths applied are equal to 160.90 mm and 122.90 mm for FI and RDI, respectively, meaning 23% less water was used in RDI compared to FI. However, the higher PAWC in the RDI subplots largely offset the reduction in irrigation water. This increased water retention capacity in RDI-treated soils likely contributed to the enhanced performance seen in 2023, as plants were able to access moisture stored in the soil for extended periods, even under reduced irrigation regimes. This water-holding advantage mitigates the risk of water stress, enabling RDI plants to maintain higher physiological activity during critical growth stages. Therefore, soil composition, particularly the fine particle content in the RDI subplots, played a pivotal role in improving irrigation efficiency without severely compromising crop performance.

In terms of physiological responses, during 2022's drought conditions, FI maintained higher gsw and transpiration levels, indicating greater resilience to water stress due to better water access, whereas RDI subplots faced more severe reductions. However, in 2023, despite RDI generally showing higher gsw for much of the season, it could not match FI's overall water use efficiency, as FI plants consistently exhibited higher transpiration. Nonetheless, the RDI plants managed to maintain cooler leaf temperatures for the majority of the season, indicating better adaptation to reduced water availability and overall stress.

The findings of this study in terms of yield, biomass, WUE, and quality parameters, showed that although differences between the two irrigation strategies were observed across both years of the study, these differences were not statistically significant. This suggests that neither irrigation treatment offered a definitive advantage over the other in terms of overall crop performance. Hence, RDI emerged as a promising water-saving strategy, especially in soils with high water retention capacity, where it maintained competitive yields and improved WUE without significantly compromising crop productivity. Conversely, FI consistently supported higher protein content and slightly higher yields under more similar soil characteristics as in 2022.

5. CONCLUSION

This study highlights the intricate relationship between irrigation management, soil composition, and plant physiological responses, while demonstrating the significant value of integrating satellite-based vegetation indices with field-level measurements for monitoring crop water status. The findings underscore the effectiveness of satellite-based vegetation indices in monitoring crop health and plant water status across different irrigation treatments. VIs such as NDVI, GNDVI, ENDVI, NDRE, and LAI proved invaluable for capturing key growth dynamics, canopy development, photosynthetic activity, and stress conditions. These indices were highly responsive to both irrigation events and climatic variations, providing actionable insights into plant water requirements. Moreover, the integration of satellite data and in-situ measurements proved essential, both for validating the VIs trends across the soybean growth cycle and for compensating the lack of more frequent field data. Their ability to fill gaps where in-situ measurements are absent, combined with their sensitivity to key plant physiological processes, makes satellite indices a powerful tool for improving agricultural decision-making and enhancing crop management practices.

The comparison between Sentinel and Planet satellite data highlights important trade-offs between spatial and temporal resolution, accuracy, and cost-effectiveness in agricultural monitoring. While Planet’s finer spatial resolution (3 m) and daily revisits provide more detailed and frequent insights, Sentinel’s coarser resolution (10 m) and less frequent acquisitions result in systematic underestimations of key vegetation indices. However, despite these discrepancies, the high correlation coefficients between the two platforms indicate that Sentinel accurately captures overall vegetative trends, making it a valuable tool mainly for large-scale monitoring. While Planet’s higher cost may limit its use to more targeted, precision-driven applications, Sentinel’s freely available data remains an accessible option for monitoring general crop health and water stress. However, its reduced spatial and temporal resolutions may be a limitation for crops requiring more frequent and precise assessments. Overall, this study underscores the importance of selecting satellite platforms based on specific management needs, balancing cost with the level of spatial and temporal detail required for effective irrigation and crop monitoring.

The comparison between FI and RDI treatments revealed that while RDI is a promising strategy for reducing water consumption, the specific soil conditions and environmental context play a pivotal role in determining the success of this approach. RDI performed well in 2022, though resulting slightly less robust than FI against water and heat stress. In 2023, under more favorable climatic conditions and higher water retention capacity in RDI plots, the performance of RDI surpassed FI in several indices, suggesting that plants can adapt to reduced water inputs when supported by appropriate soil characteristics. This highlights the need for a flexible irrigation strategy that takes into account not only the irrigation regime, but also soil composition. In terms of yield, biomass, WUE, and quality parameters, the differences between FI and RDI across both years were not statistically significant, suggesting that RDI can be a viable alternative to FI without severely compromising crop performance. This has significant implications for sustainable agriculture, particularly in regions facing increasing water scarcity due to climate change. The ability of RDI to maintain yields with less water input, especially in soils with favorable water retention properties, supports its potential as a strategy to enhance irrigation efficiency and reduce water use in agriculture.

Expanding the comparison across more diverse crops, climates, and soil types will further clarify the conditions under which different irrigation strategies are most effective. Moreover, investigating how satellite-derived indices can be calibrated for real-time irrigation decision-making is essential, especially in regions where water resources are limited. As climate change intensifies water scarcity worldwide, these themes are becoming increasingly important for ensuring food security, promoting sustainable farming practices, and enhancing global water use efficiency. Future work should also explore cost-effective solutions for small-scale farmers, enabling them to access advanced technologies for precision agriculture to mitigate water stress and adapt to evolving environmental challenges.

A. APPENDIX 1 – GUMBEL DISTRIBUTION

According to Gumbel, the cumulative distribution function $F(h)$ of the analyzed data is given by (A.1):

$$F(h) = \exp\left[-\exp\big(-\alpha(h-u)\big)\right] \tag{A.1}$$

Where, in this case, h is the annual maximum precipitation depth [mm] and α and u the scale and location parameters, respectively [68]. The parameters were through the Least Square Method, which minimizes the sum of the squares of the errors reached in each single measurement. The procedure is to sort the data in ascending and descending order with the associated position i in the rank, and calculate the Weibull [69] cumulative frequency F_i:

$$F_i = \frac{i}{n+1} \tag{A.2}$$

By taking the logarithm of both sides of the Gumbel distribution function twice and equating $F(h)$ to F_i, the following equation (A.3) can be written:

$$y_k = -\ln[-\ln(F_i)] = \alpha(h_i - u) \tag{A.3}$$

Where y_k represents the value of the reduced variable, that allows one to determine the canonical form of the exponential law. The equation highlights a linear envelope between the precipitation depths and y_k, around which the data cluster themselves if the fitting distribution is properly designed. The parameters of the Gumbel distribution α and u were computed by assessing the mean and standard deviation for both sorted data and the reduced Gumbel variable, using (A.4):

$$\alpha = \frac{S_y}{S_h};\ u = m_h - \frac{m_y}{\alpha} \tag{A.4}$$

Table A.1. Description of the necessary variables to assess the parameters of the Gumbel distribution: standard deviations and means of both Gumbel variable and observation data.

VARIABLE	DEFINITION	EQUATION
$\boldsymbol{S_y}$	Standard deviation of the reduced Gumbel variable	$S_y = \sqrt{\left(\frac{1}{n-1}\sum_{i=1}^{n}\left(y_i - m_y\right)^2\right)}$
$\boldsymbol{S_h}$	Standard deviation of the observation data	$S_h = \sqrt{\left(\frac{1}{n-1}\sum_{i=1}^{n}\left(h_i - m_y\right)^2\right)}$
$\boldsymbol{m_y}$	Mean of the reduced Gumbel variable	$m_y = \frac{1}{n}\sum_{i=1}^{n} y_i$
$\boldsymbol{m_h}$	Mean of the observation data	$m_h = \frac{1}{n}\sum_{i=1}^{n} h_i$

Finally, the extreme events associated with return periods of 10, 100, and 1000 years were estimated. The return period T_r (or recurrence interval) is defined as the average time between two subsequent exceedances of a defined event or threshold [70]. and is expressed by the following formula (A.2):

$$T_r(h) = \sum_{t=1}^{\infty} p(t) \cdot t \tag{A.2}$$

Where h is the value of the random variable (here, precipitation depth), $p(t)$ is the probability of not exceeding the design rainfall h in an arbitrary year, and t is the interarrival time between two subsequent exceedances of h.

As previously introduced, $F(h)$ is the probability of not observing exceedance in a given year. To define the same probability for (n-1) years in a row, the equation to solve is (A.3):

$$p(t) = F(h) \cdot F(h) \cdot \ldots \cdot F(h) \tag{A.3}$$

For a total of (n-1) terms.

Therefore, if the goal is to define the probability of not observing exceedances for (n-1) years in a row and then observing the overcome of the threshold in the n-th year, the formula to be applied is (A.4):

$$p(t) = F(h) \cdot F(h) \cdot \ldots \cdot F(h) \cdot [1 - F(h)] \tag{A.4}$$

Where $[1 - F(h)]$ represents the probability of observing the exceedance in that given year.

By substituting (A.4) in (A.2), it can be observed that a relationship exists between $F(h)$ and T_r (A.5):

$$F(h) = \frac{T_r - 1}{T_r} \tag{A.5}$$

Eq. (A.5) means that if the functional form of $F(h)$ is known, each value of h that corresponds to any prescribed value of the return period can be defined. By setting the (A.5) equal to (A.1) and by isolating the depth, it is possible to express the equation that relates precipitation depth with the return period (A.6):

$$h(T_r) = u - \frac{1}{\alpha} \ln\left(-\ln\left(1 - \frac{1}{T_r}\right)\right) \tag{A.6}$$

By inverting Eq. (A.6), the return period is expressed as the inverse of the probability of occurrence (A.7) [71]:

$$P = \frac{1}{T_r} \tag{A.7}$$

Using Eq. (A.7) it can be easily stated that the higher the return period, the lower the probability of having the event associated with that specific T_r.

The Gumbel distribution was applied to both annual maxima precipitation depths and annual maximum temperatures. With regards to rainfall data, the annual maxima distribution in the years 1993-2021 shows a pretty high correlation with the reduced Gumbel variable, with a correlation coefficient $R^2 = 0.9871$ (Figure A.1). The same analysis was performed for the months interested in the soy cultivation, resulting in high R^2 for all months (Figure A.2, Figure A.3).

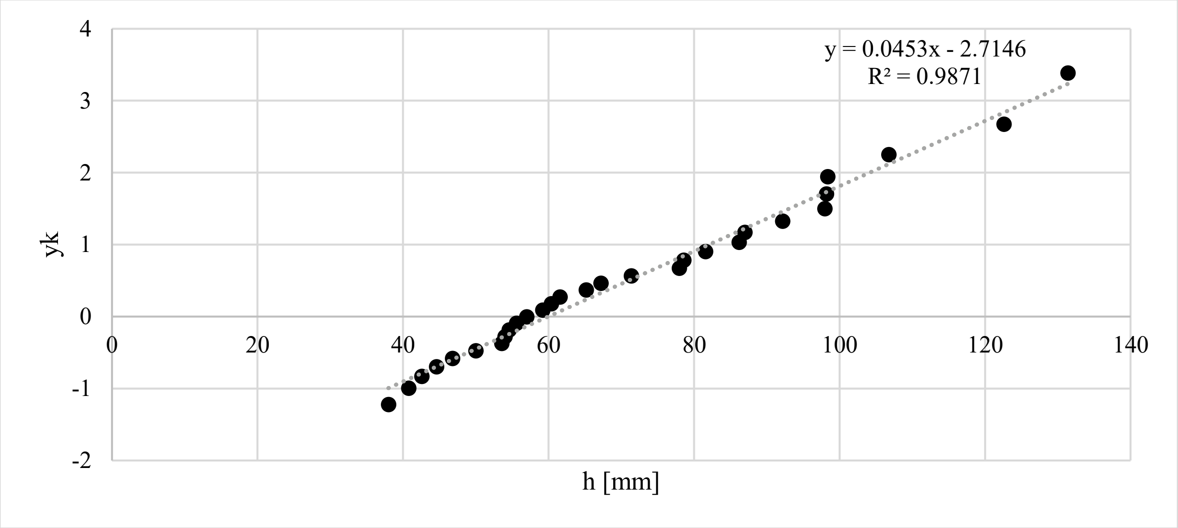

Figure A.1. Gumbel distribution application on the annual maxima precipitation depths [mm] of the considered period (1993-2021).

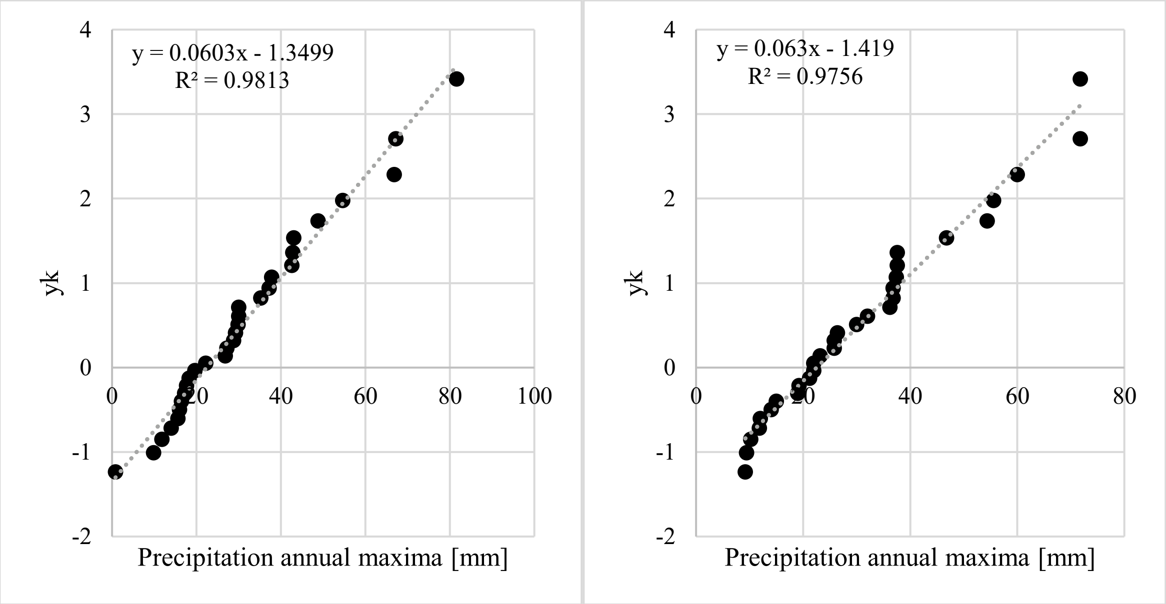

Figure A.2. Gumbel distribution on the monthly maxima precipitation depths [mm] (June on the left, July on the right) for the considered period (1992-2021).

The same procedure was applied to the temperature datasets of the study area. The annual maxima temperature [°C] shows a high correlation with the values of the reduced variable y_k, with a correlation coefficient $R^2 = 0.9784$ (Figure A.4). The monthly analysis was performed for May too, considering the years 1993-2021, as the year 1992 is incomplete. All five distributions show high correlation coefficients, with the data that cluster pretty well around the regression line.

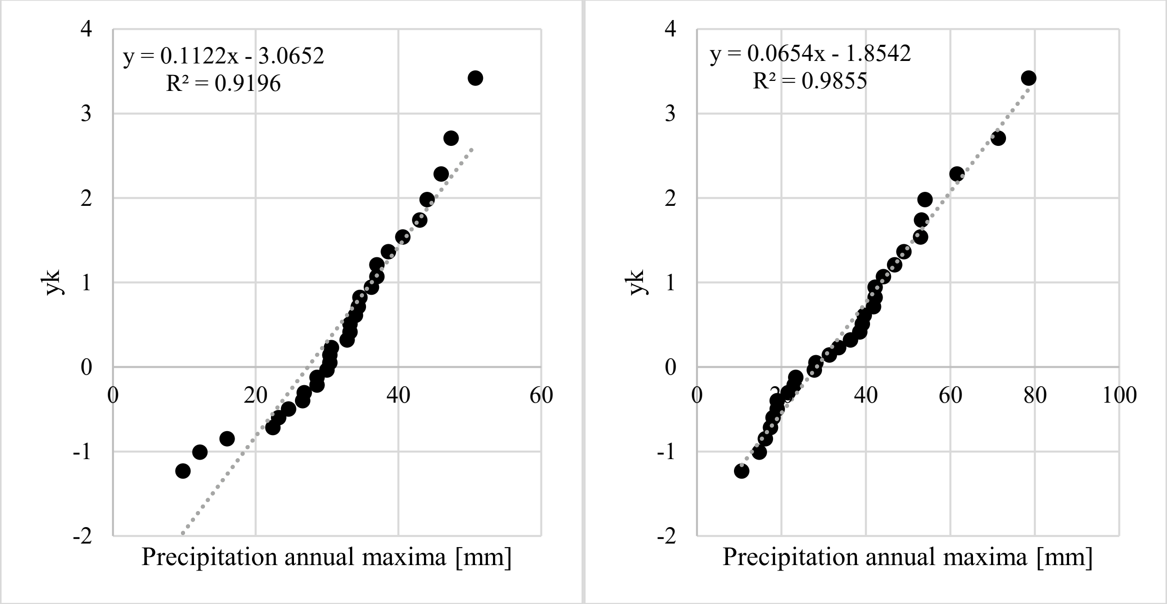

Figure A.3. Gumbel distribution on the monthly maxima precipitation depths [mm] (August on the left, September on the right) for the considered period (1992-2021).

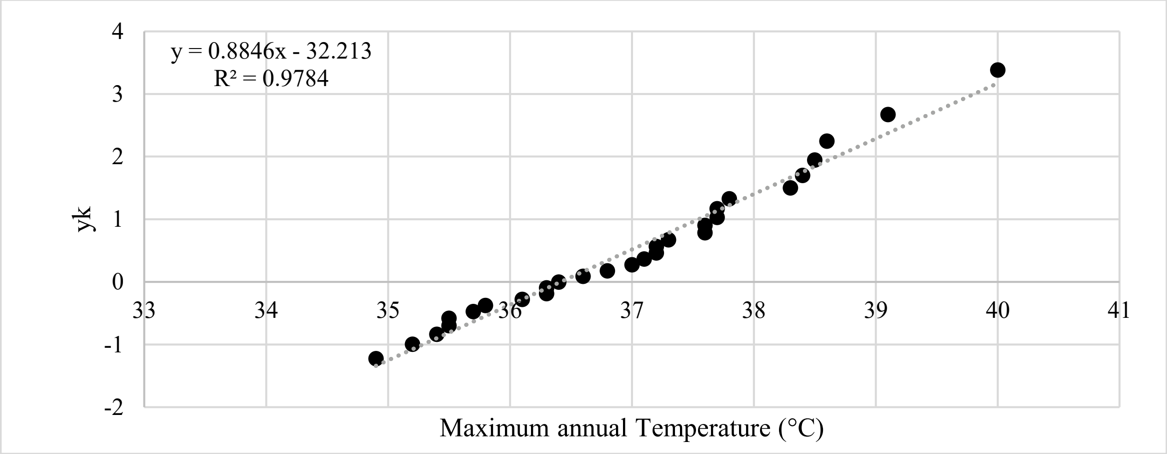

Figure A.4. Gumbel distribution application on the annual maxima temperature [°C] of the considered period (1993-2021).

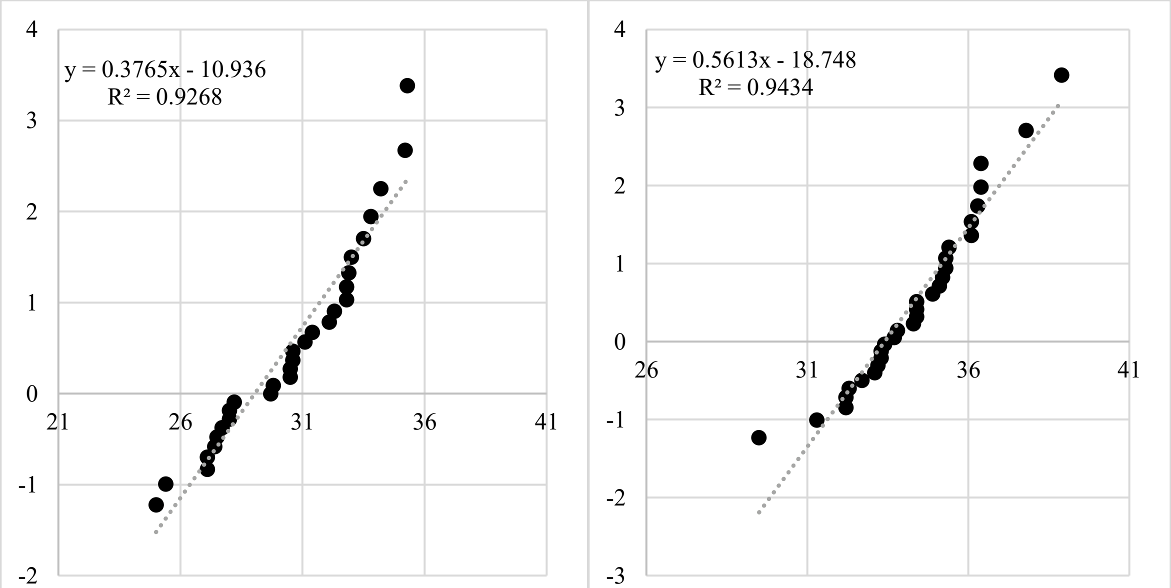

Figure A.5. Gumbel distribution on the monthly maximum temperature [°C] (May on the left, June on the right) for the considered period (1993-2021 for May, 1992-2021 for June).

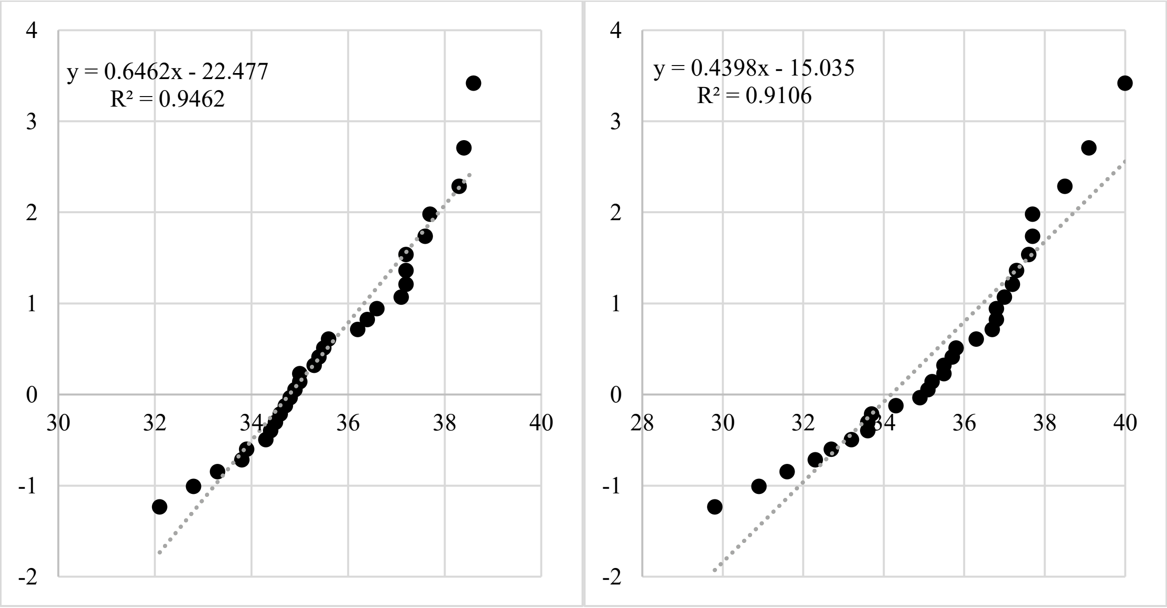

Figure A.6. Gumbel distribution on the monthly maximum temperature [°C] (July on the left, August on the right) for the considered period (1992-2021).

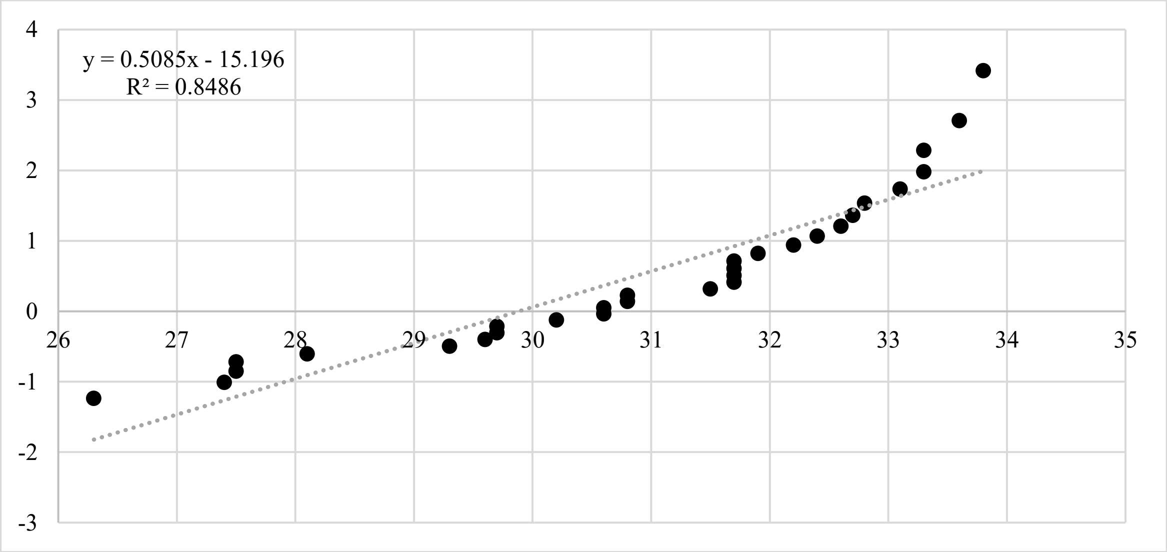

Figure A.7. Gumbel distribution on the monthly maximum temperature [°C] for September over the considered period (1992-2021).

B. APPENDIX 2 – IDW INTERPOLATION ON SOIL TEXTURE CHARACTERISTICS

The IDW interpolation technique is based on Tobler's First Law of Geography, according to which "everything is related to everything else, but near things are more related to distant things" [49]. IDW assumes that any pair of points are related to each other in such a way that their similarity decreases with their distance following a power law [50]. In particular. The estimation of a certain value z at a specific location X is given by the weighted mean of the nearby known observations (Equation (B.1):

$$\hat{z}(X) = \frac{\sum_i^n w_i z_i}{\sum_i^n w_i} \tag{B.1}$$

where w_i are the weights of the observations according to the distance to X, formulated in (B.2):

$$w_i = |X - X_i|^{-\beta} \tag{B.2}$$

The exponent $-\beta$ refers to the Euclidean distance, being the length of the line segment between connecting two points. It determines the degree of influence of the nearest versus farthest points, chosen at the user's discretion in $\mathbb{R}^+$ [84].

In this study, the exponent was taken equal to 2, representing an inverse squared relationship. The georeferenced soil samples collected in the field for both 2022 and 2023 were used as observation points, associated with the corresponding values of coarse-grained and fine-grained soil fractions (in %). The resulting IDW interpolation maps are shown in Figure B.1 and Figure B.2 for 2023, from which it can be noticed that the field is cut in half. On the subplot irrigated with Full Irrigation, the fraction of coarse-grained soil is more prevalent than finer particles, with a maximum percentage of 60.25% against the 21.66% of the field on which the Regulated Deficit Irrigation has been applied. Consequently, the fine-grained fractions are higher in the RDI subplot than in the fully irrigated one. This comparison shows how the portion of the field subjected to reduced water supply is actually better responsive to drought conditions, as it can retain more water than the other subplot. This is further confirmed by PAWC (Figure B.3), clearly showing the much higher water retention capacity of the RDI-based subplot, that can retain up to 43% more water than the FI portion of the field. This condition could hinder one of the objectives of the present study, as it influences the performance of soybean production by lower amounts of water irrigation. In fact, the good yield outcomes obtained this year could be the result of the optimal water retention capacity of the soil, rather than an effective and prompt response of the soybean crop to possible water scarcity conditions. Despite the promising performance of the study in this context, the results of 2023 RDI cannot be taken as a guarantee of the success of this irrigation strategy on soybean cultivation, and therefore not even as a basis for wider application on different environments.

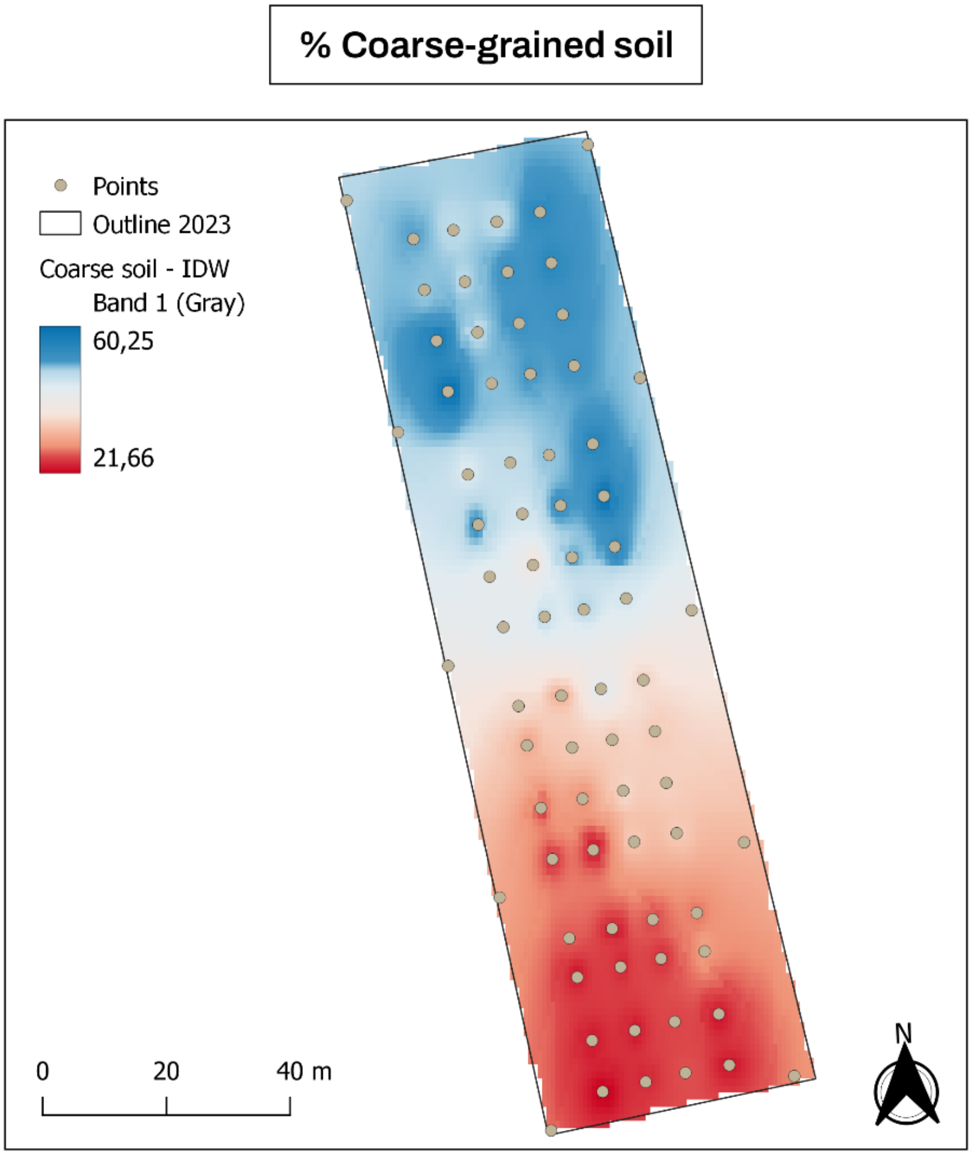

Figure B.1 IDW interpolation results on the fraction (%) of coarse-grained soil of the soybean field.

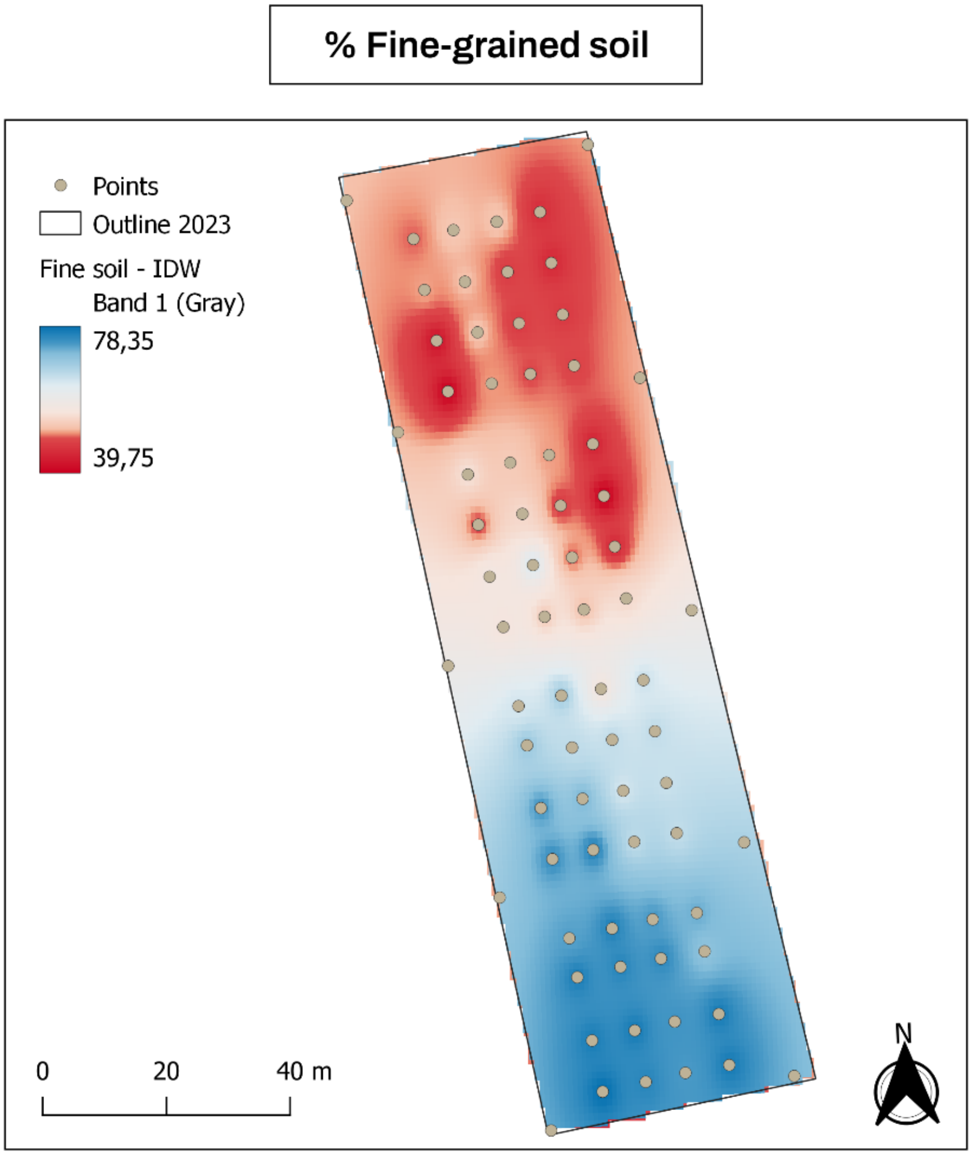

Figure B.2. IDW interpolation results on the fraction (%) of fine-grained soil of the soybean field.

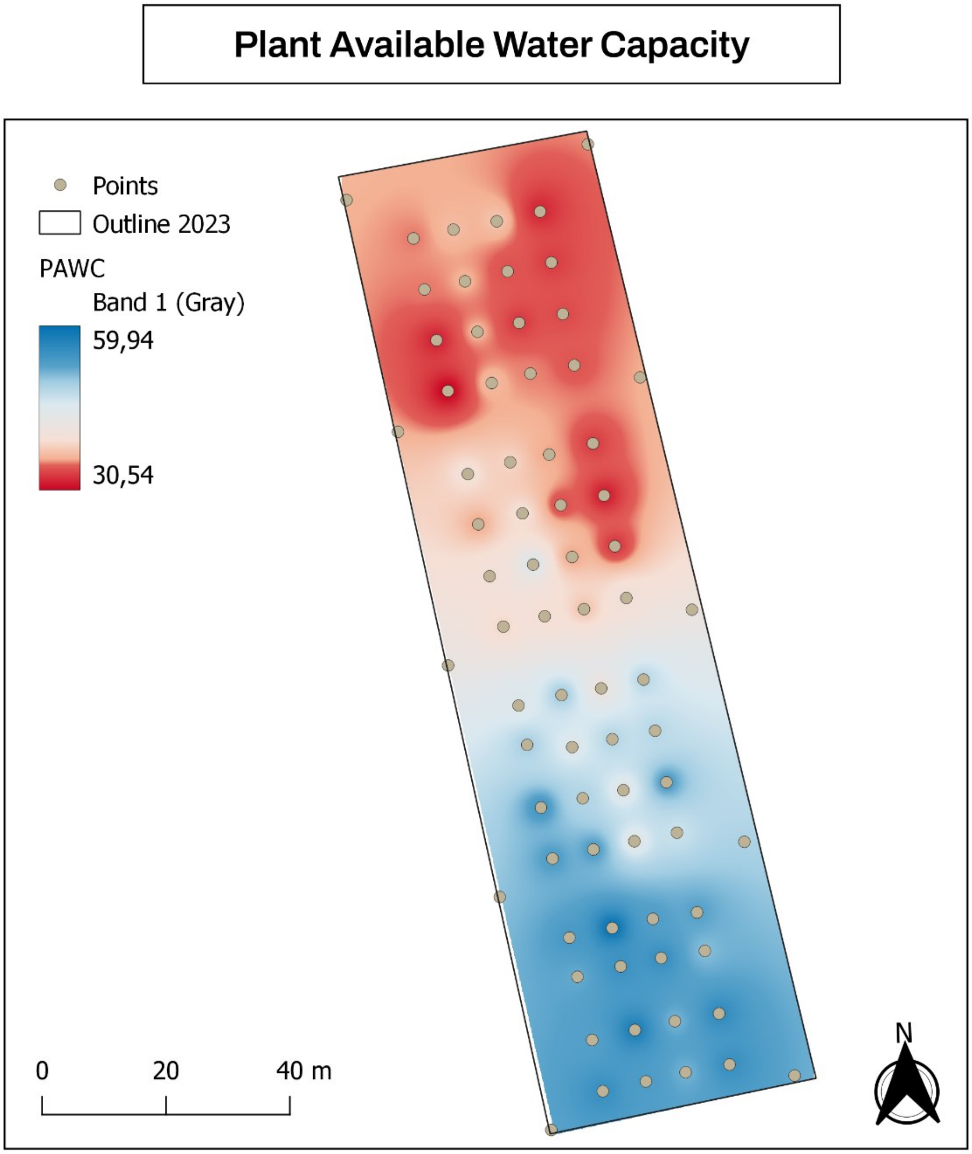

Figure B.3. IDW interpolation results on Plant Available Water Capacity (PAWC) of the soybean field.

C. APPENDIX 3 – INDICES TREND IN RESPONSE TO CLIMATE AND IRRIGATION

Planet indices are overall reliable in identifying shifts in climate, water supply, and general PWS, as proved by the trend that VIs follow throughout the soybean growth cycle in both years under examination. The following paragraph presents several examples illustrating how VIs respond to variations in water supply and temperature, comparing their trend to the physiological parameters measured at the site.

From July 1st (BBCH 37) to 12th (BBCH 54), 2023, frequent and abundant precipitation occurred, with a total of 89 mm of rain over six days, up until July 6th. This precipitation helped keep temperatures moderate (with maxima of 27-29°C). After this period, the temperature rose, peaking at 34°C on July 11th. These favorable climatic conditions are reflected in the VIs (Figure C.1, Figure C.2), which increased sustained by the ample water supply from both rainfall and irrigation. The physiological parameters followed a similar trend (Table C.1). In particular, gsw rose steadily throughout the period, indicating that stomata were more open, and transpiration was potentially favored. In fact, transpiration also reached very high values (12.07 for FI, 11.88 for RDI). Leaf temperature, on the other hand, increased up to 30°C, largely driven by the temperature spike on July 7th, when temperatures jumped from 27°C of the previous day to 31°C.

Moderate climatic conditions persisted throughout soybean growth stages in 2023, except for a brief period in September. From September 6th (BBCH 79) to 12th (BBCH 81), neither irrigation nor precipitation occurred, and temperatures rose above the average, peaking at 32°C almost daily. These conditions accelerated the decline in all VIs, as can be observed from Figure C.3 and Figure C.4. NDVI, GNDVI, and NDRE decreased by 0.08-0.12 in FI and by 0.04-0.06 in RDI subplots. ENDVI showed a smaller reduction, dropping only by 0.03 and 0.02 in FI and RDI subplots, respectively, making it the least sensitive to these climatic changes. Additionally, LAI dropped by 1.46 in FI and 0.80 in RDI, indicating a rapid decline in canopy density over just five days. This trend is corroborated by the

Table C.1. Physiological parameters (mean stomatal conductance, mean transpiration, and mean leaf temperatures) measured on July 5th and 7th, 2023.

PARAMETERS		**05/07/23**		**07/07/23**	
		RDI	**FI**	**RDI**	**FI**
gsw	[mol m-2 s-1]	0.833	0.777	0.947	0.846
T_a	[mol m-2 s-1]	9.565	10.300	11.877	12.071
T_{leaf}	[°C]	28.418	29.644	30.100	30.549

physiological data in Table C.2., which shows a decline in gsw and T_a, almost halving between subsequent measurements. The increase in T_{leaf} further confirms the stress experienced by plants.

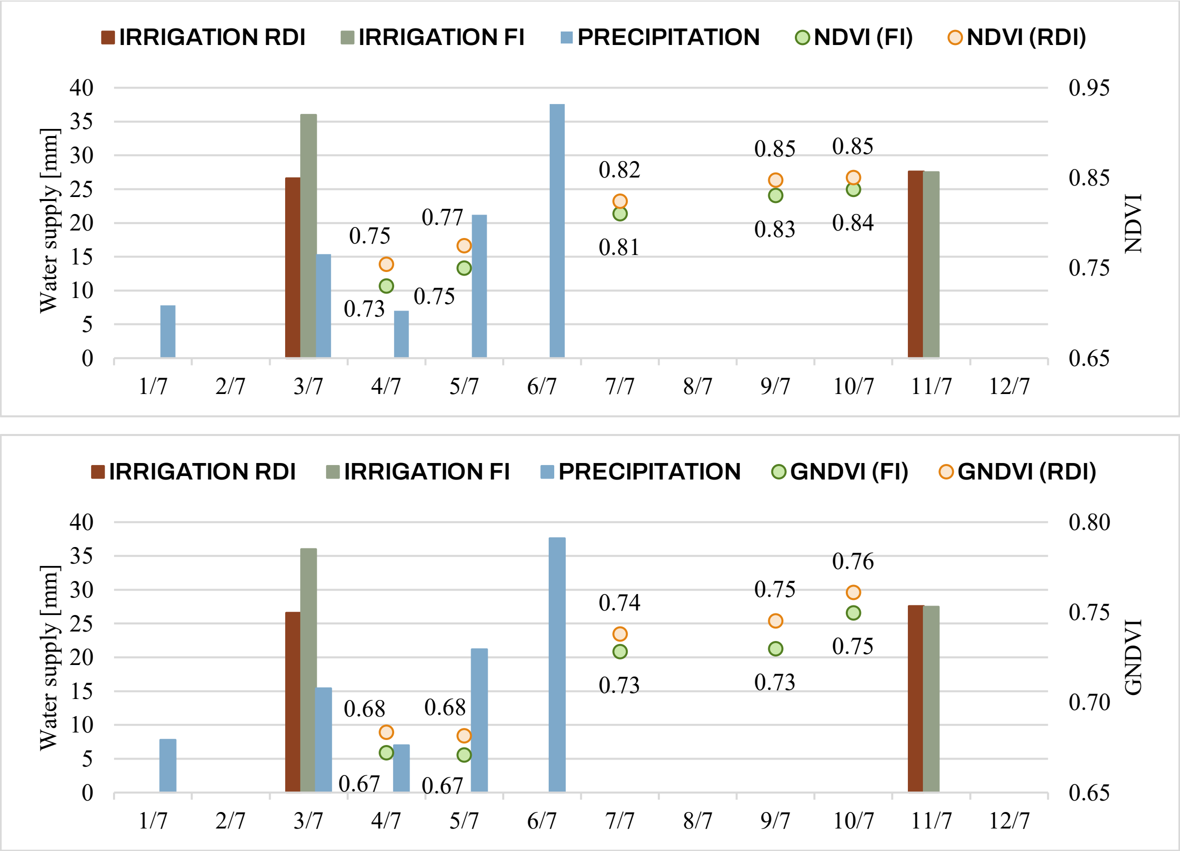

Figure C.1. Trend of NDVI (up) and GNDVI (down) during the period ranging from July 1st to 12th, 2023.

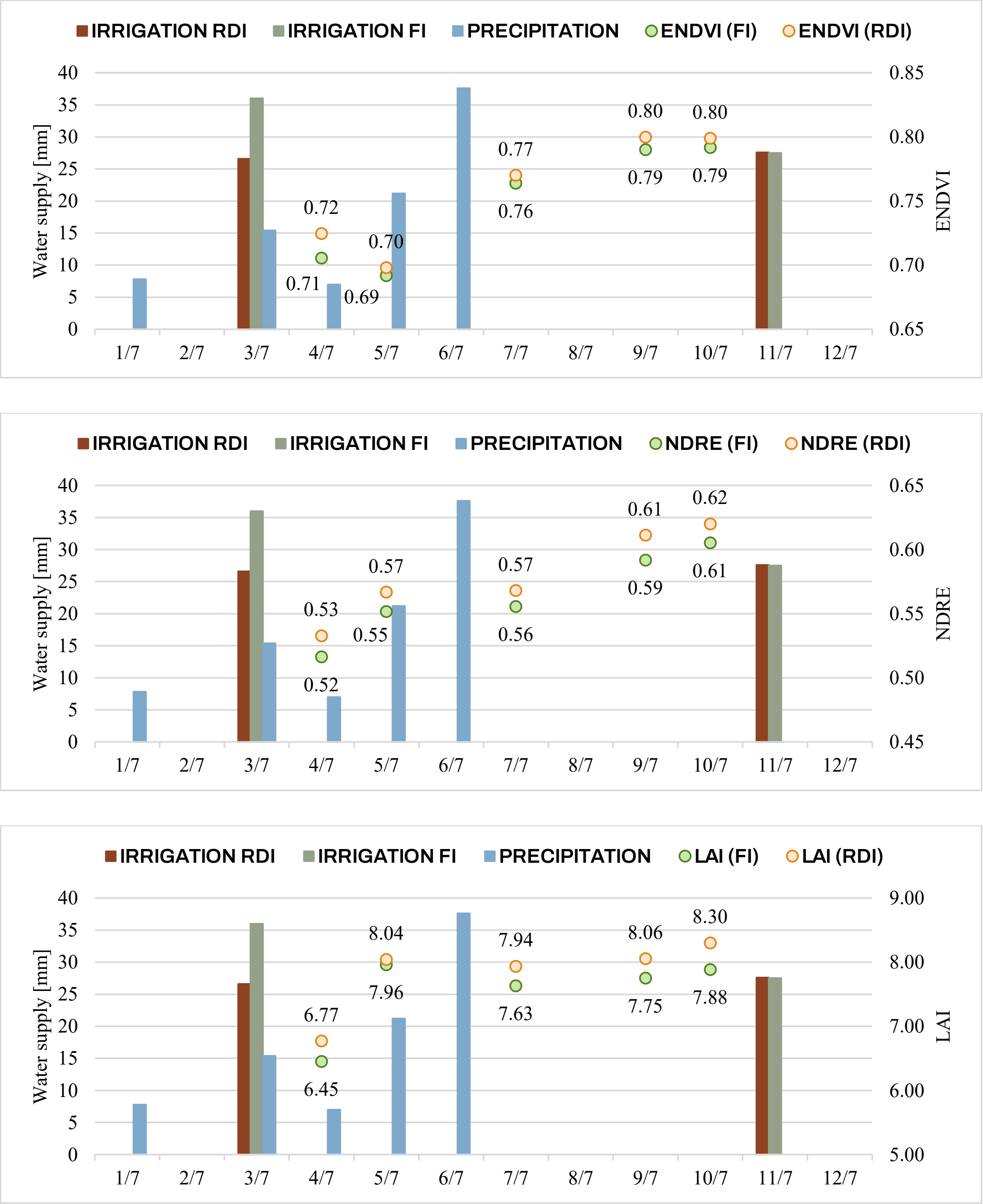

Figure C.2. Trend of ENDVI (up), NDRE (middle), and LAI (down) in the period ranging from July 1st to 12th, 2023.

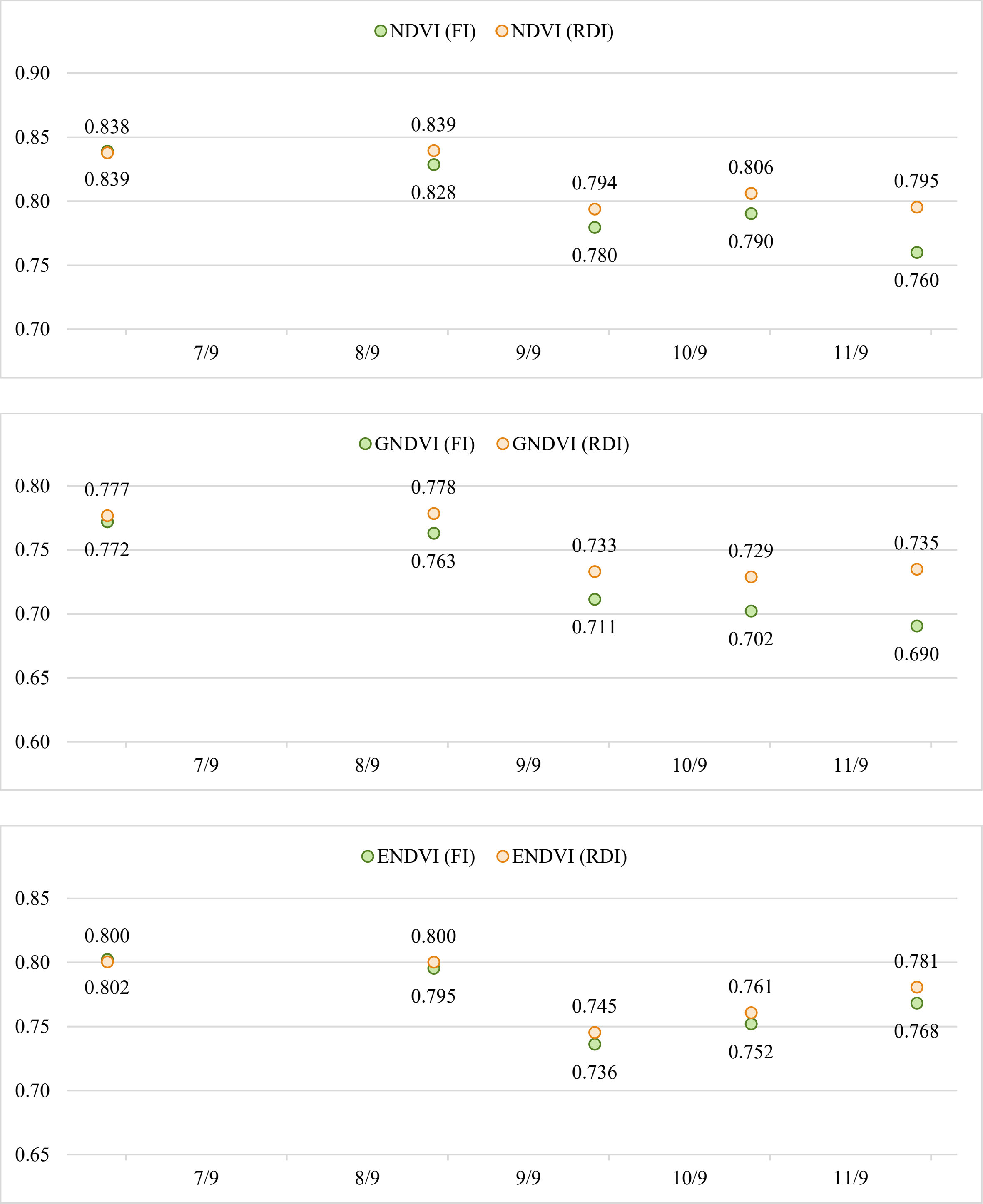

Figure C.3. Trend of NDVI (up), GNDVI (middle), and ENDVI (down) in the period ranging from September 6th to September 12th, 2023.

Table C.2. Physiological parameters (mean stomatal conductance, mean transpiration, and mean leaf temperatures) measured on September 6th and September 12th, 2023.

PARAMETER		DAYS			
		06/09/23		12/09/23	
		RDI	FI	RDI	FI
gsw	[mol m-2 s-1]	0.185	0.129	0.102	0.067
T_a	[mol m-2 s-1]	4.320	4.563	2.622	2.590
T_{leaf}	[°C]	32.059	35.357	32.103	36.050

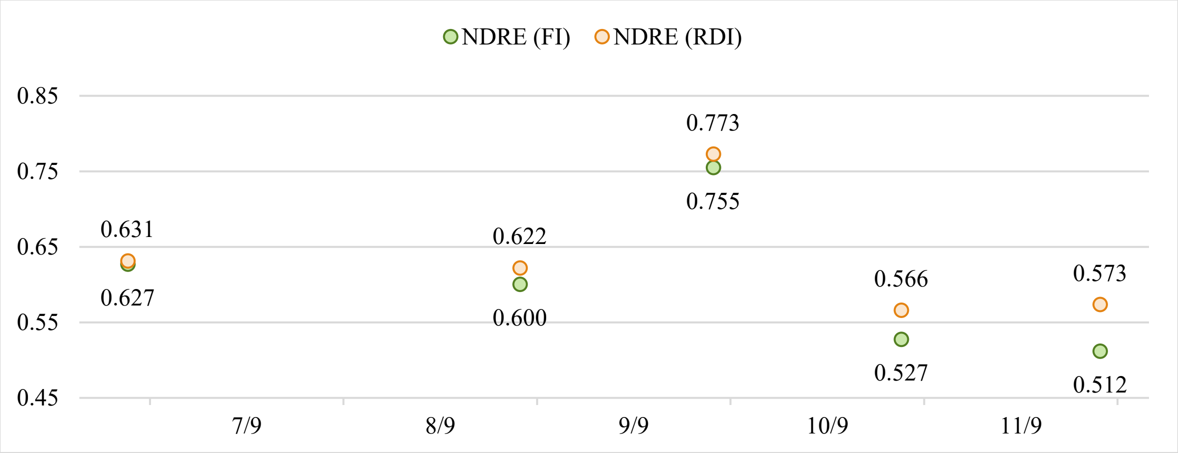

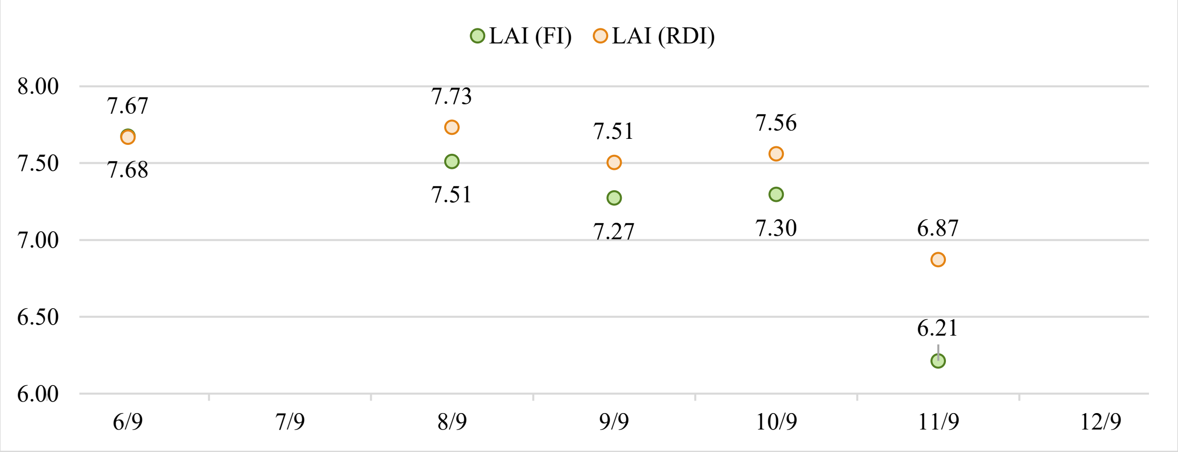

Figure C.4. Trend of NDRE (up) and LAI (down) in the period ranging from September 6th to September 12th, 2023.

BIBLIOGRAPHY

1] T. Zhu and C. Ringler, "Climate Change Impacts on Water Availability and Use in the Limpopo River Basin," *Water,* vol. 4, no. 1, pp. 63 - 84, 2012.

2] F. Xiao, X. Wang and C. Fu, "Impacts of land use/land cover and climate change on hydrological cycle in the Xiaoxingkai Lake Basin," *Journal of Hydrology: Regional Studies,* vol. 47, 2023.

3] P. Singh, P. K. Srivastava and R. K. Mall, "Estimation of potential evapotranspiration using INSAT-3D sarellite data over an agriculture area," in *Agricultural Water Management*, Academic Press, Elsevier, 2021, pp. 143 - 155.

4] A. Carella, P. T. B. Fischer, R. Massenti and R. Lo Bianco, "Continuous Plant - Based and Remote Sensing for Determination of Fruit Tree Water Status," *Horticulturae,* vol. 10, p. 516, 2024.

5] S. Rost, D. Gerten, A. Bondeau, W. Lucht, J. Rohwer and S. Schaphoff, "Agricultural green and blue water consumption and its influence on the global water system," *Water Resources Research,* vol. 44, no. 9, 2008.

6] K. Zhang, X. Li, D. Zheng, L. Zhang and G. Zhu, "Estimation of Global Irrigation Water Use by the Integration of Multiple Satellite Observations," *Water Resources Research,* vol. 58, no. 3, 2022.

7] P. Thenkebail, M. K. Gumma and V. Dheeravath, "Global Croplands and Their Water Use from Remote Srnsing and Non-remote Sensing Perspective," *Remote Sensing,* vol. 2, pp. 211-261, 2010.

8] D. Wisser, S. Frolking, E. M. Douglas, B. M. Fekete, C. J. Vörösmarty and A. H. Schumann, "Global irrigation water demand: Variability and uncertainties arising from agricultural and climate data sets," *Geophysical Research Letters,* vol. 35, no. 24, 2008.

9] S. Khan, R. Tariq, Y. Cui and J. Blackwell, "Can irrigation be sustainable?," *Agricultural Water Management,* vol. 80, no. 1, pp. 87-99, 2006.

10] H. Turral, J. Burke and J.-M. Faurès, "Climate change, water and food security," Food and Agriculture Organization of the United Nations (FAO), Rome, 2011.

11] S. Wanniarachchi and R. Sarukkalige, "A Review on Evapotranspiration Estimation in Agricultural Water Management: Past, Present, and Future," *Hydrology,* vol. 9, no. 7, p. 123, 2022.

12] E. Fereres and M. A. Soriano, "Deficit Irrigation for reducing agricultural water use," *Journal of Experimental Botany,* vol. 58, no. 2, pp. 147-159, 2007.

13] Y. Chen, J.-H. Zhang, M.-X. Chen, F.-Y. Zhu and T. Song, "Optimizing water consumption and utilization with a regulated deficit irrigation strategy in woody crops: A review," *Agricultural Water Management,* vol. 289, no. 108523, 2023.

14] Q. Chai, Y. Gan, C. Zhao, H.-L. Xu, R. M. Waskom, Y. Niu and K. H. M. Siddique, "Regulated Deficit Irrigation for crop production under drought stress. A review," *Agronomy for Sustainable Development,* vol. 36, no. 3, 2016.

15] H. Yang, H. Liu, J. Zheng and Q. Huang, "Effects of regulated deficit irrigation on yield and water productivity of chili pepper (Capsicum annuum L.) in the arid environment of Northwest China," *Irrigation Science,* vol. 36, pp. 61-74, 2018.

16] D. Gautam and V. Pagay, "A Review of Current and Potential Applications of Remote Sensing to Study the Water Status of Horticultural Crops," *Agronomy,* vol. 10, no. 1, p. 140, 2020.

17] S. Ambast, A. K. Keshari and A. Gosain, "Satellite remote sensing to support management of irrigation systems: concepts and approaches," *Irrigation and Drainage,* vol. 51, pp. 25-39, 2002.

18] J. Xue and B. Su, "Significant Remote Sensing Vegetation Indices: A Review of Developments and Applications," *Journal of Sensors,* vol. 2017, no. 1, 2017.

19] J. B. Campbell and R. H. Wynne, Introduction to Remote Sensing, Fifth Edition ed., New York, United States of America: The Guilford Press, 2011.

20] A. A. Gitelson, M. N. Merzlyak and H. K. Lichtenthaler, "Detection of Red Edge Position and Chlorophyll Content by Reflectance Measurements Near 700 nm," *Journal of Plant Physiology,* vol. 148, no. 3-4, pp. 501-508, 1996.

21] "NDVI e la tua attività: capire il significato del termine NDVI per la salute delle piante," Sky53, [Online]. Available: https://sky53.com/ndvi/#:~:text=Descrizione%20NDRE%20(Normalized%20Difference%20Red%20Edge)&text=Valori%20elevati%20di%20NDRE%20rappresentano,hanno%20i%20valori%20pi%C3%B9%20alti.. [Accessed 04 08 2024].

22] J. Traba, J. Gómez-Catasùs, A. Barrero, D. Bustillo-de la Rosa, J. Zurdo, I. Hervás, C. Pérez-Granados, E. L. García de la Morena, A. Santamaria and M. Reverter, "Comparative assessment of satellite- and drone-based vegetation indices to predict arthropod biomass in shrub-steppes," *Ecological Applications,* vol. 32, no. 8, p. 2707, 2022.

23] C. J. Strong, N. G. Burnside and D. Llewellyn, "The potential of small-Unmanned Aircraft Systems for the rapid detection of threatened unimproved grassland communities using an Enhanced Normalized Difference Vegetation Index," *PLoS ONE,* vol. 12, no. 10, p. e0186193, 2017.

24] T. M. Susantoro, K. Wikantika, A. Saepulob and H. Harsolumakso, "Utilization of Vegetation Indices to Interpret the Possibility of Oil and Gas Microseepages at Ground Surface," in *IOP Conf. Series: Earth and Environmental Science*, Bandung, Indonesia, 2017.

25] B. Boiarskii and H. Hasegawa, "Comparison of NDVI and NDRE Indices to Detect Differences," in *International Conference on Applied Science, Technology and Engineering*, 2019.

26] F. C. G. Alvino, C. C. Aleman, R. Filgueiras, D. Althoff and F. F. Da Cunha, "Vegetation Indices for Irrigated Corn Monitoring," *Engenharia Agrìcola,* vol. 40, no. 3, pp. 322-333, 2020.

27] T. Foster, T. Mieno and N. Brozović, "Satellite - Based Monitoring of Irrigation Water Use: Assessing Measurement Errors and Their Implications for Agricultural Water Management Policy," *Water Resources Research,* vol. 56, no. 11, 2020.

28] S. Barbagallo, S. Consoli and A. Russo, "A One-Layer Satellite Surface Energy Balance for Estimating Evapotranspiration Rates and Crop Water Stress Indexes," *Sensors,* vol. 9, pp. 1-21, 2009.

29] M. C. Anderson, R. G. Allen, A. Morse and W. P. Kustas, "Use of Landsat thermal imagery in monitoring evapotranspiration and managing water resources," *Remote Sensing of Environment,* vol. 122, pp. 50-65, 2012.

30] G. S. Campbell and M. D. Campbell, "Irrigation Scheduling Using Soil Moisture Measurements: Theory and Practice," in *Advances in irrigation*, New York, Academic Press, 1982, pp. 25-26.

31] E. G. Njoku and D. Entekhabi, "Passive microwave remote sensing of soil moisture," *Journal of Hydrology,* vol. 184, pp. 101-129, 1996.

32] L. Wang and J. J. Qu, "Satellite remote sensing applications for surface soil moitsture monitoring: A review," *Frontiers of Earth Science in China,* vol. 3, no. 2, pp. 237-247, 2009.

33] X. Zhang, J. Qiu, G. Leng, Y. Yang, Q. Gao, Y. Fan and J. Luo, "The Potential Utility of Satellite Soil Moisture Retrievals for Detecting Irrigation Patterns in China," *Water,* vol. 10, no. 11, p. 1505, 2018.

34] L. Brocca, A. Tarpanelli, P. Filippucci, W. Dorigo, F. Zaussinger, A. Gruber and D. Fernández-Prieto, "How much water is used for irrigation? A new approach exploiting coarse resolution satellite soil moisture products," *International Journal of Applied Earth Observation and Geoinformation,* vol. 73, pp. 752-766, 2018.

35] K. Sheffield and E. Morse-McNabb, "Using satellite imagery to assess trends in soil and crop productivity across landscapes," *IOP Conference Series: Earth and Environmental Science,* vol. 25, 2015.

36] D. Dimov and P. Noack, "Exploring the Potential of Multi - Temporal Crop Canopy Models and Vegetation Indices from Pleiades Imagery for Yield Estimation," *Remote Sensing,* vol. 15, no. 16, p. 3990, 2023.

37] B. Aragon, R. Houborg, K. Tu, J. B. Fisher and M. McCabe, "CubeSats Enable High Spatiotemporal Retrievals of Crop-Water Use for Precision Agriculture," *Remote Sensing,* vol. 10, no. 12, p. 1867, 2018.

38] M. A. Haq, "Intellligent sustainable agricultural water practice using multi sensor spatiotemporal evolution," *Environmental Technology,* vol. 45, no. 12, pp. 2285-2298, 2024.

39] F. Maselli, P. Battista, M. Chiesi, B. Rapi, L. Angeli, L. Fibbi, R. Magno and B. Gozzini, "Use of Sentinel-2 MSI data to monitor crop irrigation in Mediterranean areas," *International Journal of Applied Earth Observation and Geoinformation,* vol. 93, 2020.

40] I. P. de Lima, R. G. Jorge and J. L. M. P. de Lima, "Remote Sensing Monitoring of Rice Fields: Towards Assessing Water Saving Irrigation Management Practices," *Frontiers in Remote Sensing,* vol. 2, no. 762093, 2021.

41] R. Casa, D. Upreti and F. Pelosi, "Measurement and estimation of leaf area index (LAI) using commercial instruments and smartphone-based systems," in *1st Workshop on Metrology for Agriculture and Forestry (METROAGRIFOR)*, 2019.

42] G. Zheng and M. Moskal, "Retrieving Leaf Area Index (LAI) Using Remote Sensing: Theories, Methods and Sensors," *Sensors,* vol. 9, pp. 2719-2745, 2009.

43] N. J. J. Bréda, "Ground-based measurements of leaf area index: a review of methods, instruments and current controversies," *Journal of Experimental Botany,* vol. 54, no. 392, pp. 2403-2417, 2003.

44] E. Boegh, H. Soegaard, N. Broge, C. B. Hasager, N. O. Jensen, K. Schelde and A. Thomsen, "Airborne multispectral data for quantifying leaf area index, nitrogen concentration, and photosynthetic efficiency in agriculture," *Remote Sensing of Environment,* vol. 81, pp. 179 - 193, 2002.

45] S. Skakun, N. I. Kalecinski, M. G. L. Brown, D. M. Johnson, E. F. Vermote and J.-C. F. B. Roger, "Assessing within-Field Corn and Soybean Yield Variability from WorldView-3, Planet, Sentinel-2, and Landsat 8 Satellite Imagery," *Remote Sensing,* vol. 13, no. 5, p. 872, 2021.

46] J. Segarra, "Satellite Imagery in Precision Agriculture," in *Digital Agriculture: A Solution for Sustainable Food and Nutritional Security*, Springer, Cham, 2024, pp. 325 - 340.

47] M. Sozzi, F. Marinello, A. Pezzuolo and L. Sartori, "Benchmark of Satellites Image Services for Precision Agricultural Use," in *European Society of Agricultural Engineers 2018*, Wageningen, Netherlands, 2018.

48] H. Li, J. Van den Bulcke, O. Mendoza, H. Deroo, G. Haesaert, K. Dewitte, S. De Neve and S. Sleutel, "Soil texture controls added organic matter mineralization by regulating soil moisture—evidence from a field experiment in a maritime climate," *Geoderma,* vol. 410, no. 115690, 2022.

49] R. K. Rai, V. P. Singh and A. Upadhyay, "Irrigation Scheduling," in *Planning and Evaluation of Irrigation Projects: Methods and Implementation*, Academic Press, 2017, pp. 385-412.

50] R. G. Allen, L. S. Pereira, D. Raes and M. Smith, "Chapter 8 - ETc under soil water stress conditions," in *Crop evapotranspiration - Guidelines for computing crop water requirements - FAO Irrigation and Drainage Paper 56*, Rome, FAO - Food and Agriculture Organization of the United Nations, 1998.

51] I. Cousin, S. Buis, P. Lagacherie, C. Doussan, C. Le Bas and M. Guérif, "Available water capacity from a multidisciplinary and multiscale viewpoint. A review," *Agronomy for Sustainable Development,* vol. 42, no. 46, 2022.

52] Federal Research Centre for cultivated Plants, "Growth stages of mono- and dicotyledonous plants," 1997. [Online]. Available: https://www.julius-kuehn.de/media/Veroeffentlichungen/bbch%20epaper%20en/page.pdf. [Accessed 2024 10 02].

53] V. Cherlinka, "Soybean Growth Stages: Season-Long Guide For Crop Care," EOS Data Analytics, 27 02 2024. [Online]. Available: https://eos.com/crop-management-guide/soybean-growth-stages/. [Accessed 02 10 2024].

54] P. Munger, H. Bleiholder, H. Hack, M. Hess, R. Stauss, T. van den Boom and E. Weber, "Phenological Growth Stages of the Soybean Plant (Glycine max L.

MERR.): Codification and Description According to the BBCH Scale*," *Journal of Agronomy and Crop Science,* vol. 179, no. 4, pp. 209-217, 2001.

55] L. L. Korte, J. H. Williams, E. Specht and R. C. Sorensen, "Irrigation of Soybean Genotypes During Reproductive Ontogeny. I. Agronomic Responses," *Crop Science,* vol. 23, no. 3, pp. 521-527, 1983.

56] F. Morbidini, B. Jr., Wilfredo, G. Zanin, L. Verdi, C. Camarotto, G. Ghinassi, C. Maucieri, A. Dalla Marta and M. Borin, "The state of the art on deficit irrigation in soybean," *Irrigation and Drainage,* pp. 1-13, 2023.

57] A. D'Amico, G. Ciulla, D. Panno and S. Ferrari, "Building energy demand assessment through heating degree days: The importance of a climatic dataset," *Applied Energy,* vol. 242, pp. 1285-1306, 2019.

58] I. M. Hernandez-Ochoa and S. Asseng, "Cropping Systems and Climate Change in Humid Subtropical Environments," *Agronomy,* vol. 8, no. 2, p. 19, 2018.

59] ARPAV, "Clima e cambiamenti climatici in Veneto," 2022.

60] "Rete di Telemisura," ARPAV, 16 09 2022. [Online]. Available: https://www.arpa.veneto.it/temi-ambientali/meteo/monitoraggio/rete-di-telemisura-1. [Accessed 05 08 2024].

61] K. Cooray, "Generalized Gumbel distribution," *Journal of Applied Statistics,* vol. 37, no. 1, pp. 171-179, 2010.

62] Energypedia, "Solar Irradiation," [Online]. Available: https://energypedia.info/wiki/SPIS_Toolbox_-_Solar_Irradiation#:~:text=Solar%20radiation%20can%20be%20categorized,m2%20is%20very%20high%20radiation.. [Accessed 09 08 2024].

63] Sistema Nazionale per la Protezione dell'Ambiente, "Il clima in Italia nel 2022," Report Ambientali SNPA 36, 2023.

64] ARPAV, "Il meteo nel 2022 in Veneto: un anno da record per caldo e deficit di precipitazioni," Teolo, 2023.

65] Sistema Nazionale per la Protezione dell'Ambiente, "Il clima in Italia nel 2023," Report Ambientali SNPA 42, 2024.

66] ARPAV, "Agrometeo Mese - Anno 2023," Teolo, 2024.

67] LI-COR Biosciences, "LI-COR Corporate," [Online]. Available: https://www.licor.com/corp/history. [Accessed 2024 August 29].

68] C. Gimenéz, M. Gallardo and R. Thompson, "Plant-Water Relations," in *Encyclopedia of Soils in the Environment*, New York, Academic Press, 2005, pp. 231-238.

69] LI-COR, "Using the LI-600 Porometer/Fluorometer - Instruction Manual," 12 December 2023. [Online]. Available: https://licor.app.boxenterprise.net/s/wym7qeyy51myp425lyu9jthsadmsj74c. [Accessed 2024 08 29].

70] M. Gräf, M. Immitzer, P. Hietz and R. Stangl, "Water-Stressed Plants Do Not Cool: Leaf Surface Temperature of Living Wall Plants under Drought Stress," *Sustainability,* vol. 13, no. 7, p. 3910, 2021.

71] LI-COR, "Support: LI-600 Porometer/Fluometer," LI-COR, [Online]. Available: https://www.licor.com/env/support/LI-600/topics/taking-measurements.html. [Accessed 13 09 2024].

72] "Planet Developers," Planet, 17 July 2024. [Online]. Available: https://developers.planet.com/docs/data/planetscope/. [Accessed 21 July 2024].

73] "PlanetScope Mission," European Space Agency ESA, [Online]. Available: https://earth.esa.int/eogateway/missions/planetscope. [Accessed 21 07 2024].

74] J. Tan, J. Ding, L. Han, X. Ge, X. Wang, J. Wang, R. Wang, S. Qin, Z. Zhang and Y. Li, "Exploring PlanetScope Satellite Capabilities for Soil Salinity Estimation and Mapping in Arid Regions Oases," *Remote Sensing,* vol. 15, no. 4, p. 1066, 2023.

75] "Sentinel-2: Colour vision for Copernicus," European Space Agency, [Online]. Available: https://www.esa.int/Applications/Observing_the_Earth/Copernicus/Sentinel-2. [Accessed 21 07 2024].

76] "Sentinel-2," DataSpace Copernicus, European Space Agency (ESA), [Online]. Available: https://dataspace.copernicus.eu/explore-data/data-collections/sentinel-data/sentinel-2. [Accessed 21 07 2024].

77] A. Pisanti, S. Magrì, I. Ferrando and B. Federici, "Sea water turbidity analysis from Sentinel-2 images: atmospheric correction and bands correlation," *The International Archives of the Photogrammetry Remote Sensing and Spatial Information Sciences,* Vols. XLVIII-4, no. W1-2022, pp. 371-378, 2022.

78] J. Segarra, M. L. Buchaillot and J. L. K. S. C. Araus, "Remote Sensing for Precision Agriculture: Sentinel-2 Improved Features and Applications," *Agronomy,* vol. 10, no. 5, p. 641, 2020.

79] "Understanding PlanetScope Instruments," Planet Developers, 30 07 2024. [Online]. Available: https://developers.planet.com/docs/apis/data/sensors/. [Accessed 01 08 2024].

80] S. Huang, L. Tang, J. P. Hupy, Y. Wang and G. Shao, "A commentary review on the use of normalized difference vegetation index (NDVI) in the era of popular remote sensing," *Journal of Forestry Research,* vol. 32, pp. 1-6, 2021.

81] "Normalized Difference Vegetation Index," International Production Assessment Division, U.S. Department of Agriculture, [Online]. Available: https://ipad.fas.usda.gov/cropexplorer/Definitions/spotveg.htm#:~:text=In%20general%2C%20NDVI%20values%20range,vegetation%20(0.6%20and%20above).. [Accessed 02 08 2024].

82] S. Antognelli, "Indici di vegetazione NDVI e NDMI: istruzioni per l'uso," Agricolus, 29 05 2018. [Online]. Available: https://www.agricolus.com/indici-vegetazione-ndvi-ndmi-istruzioni-luso/. [Accessed 04 08 2024].

83] S. M. A. Letsoing, R. C. Purwestri, M. C. Perdana, P. Hnizdil and D. Herak, "Monitoring of Paddy and Maize Fields Using Sentinel-1 SAR Sata and NGB Images: A Case Study in Papua, Indonesia," *Processes,* vol. 11, p. 647, 2023.

84] H. Xheng, T. Cheng, D. Li, X. Zhou, X. Yao, Y. Tian, W. Cao and Y. Zhu, "Evaluation of RGB, Color-Infrared and Multispectral Images Acquired from Unmanned Aerial Systems for the Estimation of Nitrogen Accumulation in Rice," *Remote Sensing,* vol. 10, no. 6, p. 824, 2018.

85] "NDRE: Normalized Difference Red Edge Index," EOS Data Analytics, [Online]. Available: https://eos.com/make-an-analysis/ndre/. [Accessed 02 08 2024].

86] T. D. Setiyono, A. Weiss, J. E. Specht, K. G. Cassman and A. Dobermann, "Leaf area index simulation in soybean grown under near-optimal conditions," *Field Crops Research,* vol. 108, pp. 82-92, 2008.

87] GISGeography, "What is Bilinear Interpolation?," [Online]. Available: https://gisgeography.com/bilinear-interpolation-resampling/. [Accessed 16 09 2024].

88] P. Mishra, U. Singh, C. M. Pandey, P. Mishra and G. Pandey, "Application of Student's t-test, Analysis of Variance, and Covariance," *Cardiac Anaesthesia,* vol. 22, no. 4, pp. 407-411, 2019.

89] H. P. Hong, S. H. Li and T. Mara, "Performance of the generalized least - square method for the Gumbel distribution and its application to annual maximum wind speeds," *Journal of Wind Engineering and Industrial Aerodynamics,* vol. 119, pp. 121-132, 2013.

90] W. Weibull, "A Statistical Distribution Function of Wide Applicability," *Journal of Applied Mechanics,* Vols. hal-03112318f, pp. 1-5, 1951.

91] E. Koliokosta, "Return Periods in Assessing Climate Change Risks: Uses and Misuses," in *16th International Conferance on Meteorology, Climatology, and Atmospheric Physics - COMECAP*, Athens, 2023.

92] ASCE, Hydrology Handbook, American Society of Civil Engineers, 1996.

93] N. Waters, "Tobler's First Law of Geography," *Wiley - Online Library,* 2018.

94] A. a. i.-d. w. s. i. technique, "Lu, George Y.; Wong, David W.," *Computers & Geosciences,* vol. 34, no. 9, pp. 1044-1055, 2008.

95] K. Hartmann, J. Krois and A. Rudolph, "Statistics and Geodata Analysis using R (SOGA-R)," Berlin, 2023.

96] A. Neupane, N. Raj, R. Deo and M. Ali, "Chapter 6 - Development of data-driven models for wind speed forecasting in Australia," in *Predictive Modelling for Energy Management and Power Systems Engineering*, Elsevier, 2021, pp. 143-190.